

## **Design of an Apparatus for Wind Tunnel Tests of Electric UAV Propulsion Systems**

**Miguel Marques Borges**

Thesis to obtain the Master of Science Degree in

### **Mechanical Engineering**

Supervisors: Prof. André Calado Marta  
Prof. Virgínia Isabel Monteiro Nabais Infante

### **Examination Committee**

Chairperson: Prof. Luis Manuel Varejão Oliveira Faria  
Supervisor: Prof. André Calado Marta  
MemberCommittee: Prof. Luís Alberto Gonçalves de Sousa

**June 2015**



*To my parents for their unconditional support.*



## **Acknowledgments**

First and foremost, to my Supervisors, Prof. André Marta and Prof. Virgínia Infante for their patience, support and help that gave me throughout the time it took me to complete this thesis. A special word of thanks to Prof. André Marta for his effort on trying to make this thesis a unique work but also to improve my soft and technical skills.

To my parents: my father who was always an example to me as a hard worker and my mother for the unconditionally love and support which always allowed me to embrace my projects and passions. Also thanks to my girlfriend Małgorzata Ogórek for her patience, love and support at all time.

To all my friends, for their love and support that accompanied me at all times. A special thanks to Luis Prior, Marco Roda, Carlos Branco and João Batista that were always available at any time to help me. Also to all my other friends that did not mention but were no less important in any way.



## Resumo

A procura de fontes energéticas alternativas tem crescido nos últimos anos. A mudança para a energia eléctrica já pode ser vista na indústria automóvel, e a indústria aeronáutica está lentamente a seguir o mesmo caminho. Esta tese foca-se no projeto, construção e validação de um sistema capaz de testar sistemas propulsivos eléctricos capazes de serem utilizados em aeronaves não tripuladas. O sistema desenvolvido foi um banco de ensaios capaz de testar motores eléctricos acoplados a hélices com um diâmetro máximo de 27 polegadas. O sistema de medição instalado no banco de ensaios é flexível o suficiente para ser capaz de efectuar medições de diferentes gamas geradas por diferentes sistemas propulsivos. O aparato experimental foi instalado dentro do tunel de vento aero-acustico do IST, para permitir efectuar ensaios em condições dinâmicas e estáticas. Todo o projecto mecânico efectuado teve em conta os limites de medição estudados previamente de acordo com os dados fornecidos pelos fabricantes de hélices. Por meio deste banco de ensaios é possível gerar os dados relativos ao sistema propulsivo de uma maneira simples e flexível. Para isto foi desenhado o sistema de interface para que o utilizador possa ter acesso a todos os dados gerados pelo sistema propulsivo em tempo real, mas ao mesmo tempo possa também guardar os mesmos para posterior processamento

**Palavras-chave:** UAV, Propulsão Eléctrica, Banco de Ensaios, Túnel de Vento, Aquisição de Dados,





## **Abstract**

The demand for alternative energy sources has grown in recent years. The shift to electricity can already be seen in the automotive industry, and the aviation industry is slowly following the same path. This thesis focuses on the design, construction and validation of a system to test electrical propulsive systems capable of being used in unmanned aerial aircraft. The system developed was a test rig capable of testing electric motors with propellers with a maximum diameter of 27 inches. The measuring system installed on the test rig is flexible enough to be able to perform measurements of different ranges generated by different propulsive systems. The experimental apparatus was installed in the aero-acoustic wind tunnel IST that allows out tests in a dynamic and static environment. All the mechanical design takes into account the measurement limits previously studied according to data provided by the propeller manufacturers. Through this test bench it is possible to generate the data for the propulsion system in a simple and flexible way. For this, it was created an interface so that the user can have access to all the generated data by the propulsion system in real time, but at the same time can also store that data for further post processing.

**Keywords:** UAV, Electric Propulsion, Test Rig, Wind Tunnel. Propeller Performance, Data Acquisition



# Contents

- Acknowledgments . . . . . v
- Resumo . . . . . vii
- Abstract . . . . . ix
- List of Tables . . . . . xvi
- List of Figures . . . . . xix
- Nomenclature . . . . . xxii
- Glossary . . . . . xxiii
  
- 1 Introduction . . . . . 1**
- 1.1 Motivation . . . . . 1
- 1.2 The LEEUAV Project . . . . . 2
- 1.3 Objectives . . . . . 2
- 1.4 Contents . . . . . 3
  
- 2 Hystorical Perspective of UAVs . . . . . 5**
- 2.1 History of Flight . . . . . 5
- 2.2 First Powered Flight . . . . . 6
- 2.3 The Uprising of UAVs . . . . . 6
- 2.4 UAVs in Portugal . . . . . 9
- 2.5 Future Work in UAVs . . . . . 11
  
- 3 Propulsion Systems . . . . . 13**
- 3.1 Types of Propulsion Systems . . . . . 13
- 3.1.1 Piston Engines . . . . . 14
- 3.1.2 Jet Engines . . . . . 14
- 3.1.3 Rocket Engines . . . . . 15
- 3.1.4 Electric Motors . . . . . 15
- 3.2 LEEUAV Propulsion System . . . . . 15
- 3.3 Propulsion Components . . . . . 16
- 3.3.1 Propellers . . . . . 16
- 3.3.2 Electric Motors . . . . . 23
- 3.3.3 Electronic Speed Controller (ESC) . . . . . 25

3.3.4	Power Supply/Battery . . . . .	26
<b>4</b>	<b>Test Rig Requirements</b>	<b>29</b>
4.1	Propeller . . . . .	30
4.2	Brushless Motor . . . . .	34
4.3	Power Supply . . . . .	35
4.4	Electronic Speed Controller . . . . .	37
4.5	Wind Tunnel . . . . .	37
<b>5</b>	<b>Test Rig Design</b>	<b>41</b>
5.1	Measuring Method . . . . .	41
5.2	Studied Solutions . . . . .	43
5.3	Proposed Structure Design . . . . .	45
5.3.1	Overall Dimensions and Components . . . . .	46
5.3.2	Main Properties of the components . . . . .	47
5.3.3	Load Analysis . . . . .	48
5.4	Assembly Motor+Propeller . . . . .	59
5.5	Support Foundation Design . . . . .	61
5.5.1	CAD Model . . . . .	61
5.5.2	Overall Dimensions and Components . . . . .	62
5.6	Aerodynamic Shielding . . . . .	62
5.7	Final Design and Build . . . . .	65
<b>6</b>	<b>Sensing, Data Acquisition and Control</b>	<b>68</b>
6.1	Summary of Measuring Quantities . . . . .	68
6.2	Sensor Selection . . . . .	68
6.2.1	Load Cell . . . . .	68
6.2.2	Voltage and Current Sensor . . . . .	69
6.2.3	RPM Sensor . . . . .	69
6.2.4	Temperature Sensor . . . . .	70
6.2.5	Air Speed Sensor . . . . .	71
6.3	Motor Speed Control . . . . .	71
6.4	Data Acquisition System . . . . .	72
6.5	Wiring Layout . . . . .	73
6.6	User Interface . . . . .	73
6.7	Recorded Data . . . . .	74
<b>7</b>	<b>Test Rig Testing</b>	<b>76</b>
7.1	Sensor Calibration . . . . .	76
7.1.1	Load Cell Sensor . . . . .	76
7.1.2	Voltage and Current Sensor . . . . .	77

7.1.3 Air Stream Velocity Sensor . . . . .	78
7.2 Static Test . . . . .	79
7.3 Dynamic Test . . . . .	80
<b>8 Conclusions</b>	<b>85</b>
8.1 Achievements . . . . .	85
8.2 Future Work . . . . .	85
<b>Bibliography</b>	<b>88</b>
<b>A LiPo cells duration</b>	<b>89</b>
<b>B Technical Datasheets</b>	<b>90</b>



# List of Tables

4.1	Maximum possible values of RPM for each propeller . . . . .	30
4.2	Maximum and minimum values of thrust presented in the structure . . . . .	31
4.3	Propulsive power for three ranges of propellers . . . . .	33
4.4	Propeller efficiency for each propeller for a certain advance ratio . . . . .	34
4.5	Minimum electrical power for the testing motors . . . . .	34
4.6	Required maximum current of the ESC . . . . .	37
5.1	Description of the components present in the structure . . . . .	45
5.2	Relations $\frac{D_1}{D_2}$ available in the main beam . . . . .	47
5.3	Mechanical properties of the materials used in study . . . . .	48
5.4	Critical load present in the structure . . . . .	48
5.5	Geometric parameters of the main beam for thickness of 1.5 millimetres . . . . .	51
5.6	Stress present in the main beam for different geometries . . . . .	51
5.7	Safety coefficient for an aluminium main beam present in the different geometries . . . . .	52
5.8	Safety coefficient for a steel main beam in the different geometries. . . . .	52
5.9	Geometric parameters of the rear beam . . . . .	53
5.10	Stress present in the rear beam for different cross-section sizes . . . . .	54
5.11	Safety coefficient for an aluminium rear beam for different cross-section sizes. . . . .	54
5.12	Safety coefficient for a steel rear beam for different cross-section sizes. . . . .	54
5.13	Geometric parameters for different diameters of the pin. . . . .	56
5.14	Stress present in the pin for different diameters . . . . .	56
5.15	Safety coefficient for a steel pin for different diameters . . . . .	56
5.16	Geometric parameters of the support beam . . . . .	58
5.17	Stress present in the support beam for different cross-section sizes . . . . .	58
5.18	Safety coefficient for an aluminium support beam for different cross-section sizes . . . . .	59
5.19	Safety coefficient for a steel support beam present for different cross-section sizes . . . . .	59
5.20	Description of the components present in the structure motor+propeller . . . . .	60
5.21	Description of the structural components present in the support foundation . . . . .	62
6.1	Summary of measured quantities and respective ranges . . . . .	68
A.1	Values used to plot the LiPo cells usage . . . . .	89





# List of Figures

1.1	Long Endurance Electric UAV . . . . .	2
2.1	One of Leonardo's sketches . . . . .	5
2.2	Wright Brother's Flyer III . . . . .	6
2.3	The USAF Liberty Eagle Aerial Torpedo . . . . .	7
2.4	General Atomics MQ-1 Predator at Paris Air Show 2007 . . . . .	8
2.5	Israeli Aircraft Industries Scout drone . . . . .	8
2.6	UAV AR1 Blue Ray acquired by PSP . . . . .	9
2.7	Pitvant family . . . . .	9
2.8	Alpha UAS . . . . .	10
2.9	UAS 30 . . . . .	10
2.10	Spyro UAV designed and built by UAVision . . . . .	11
2.11	Spin.Works Integrated UAV system for forest management . . . . .	11
2.12	QuadCopter of DHL . . . . .	12
3.1	Aircraft propulsion systems in relation to flight envelopes . . . . .	13
3.2	Typical cross-section of a four-cylinder piston engine . . . . .	14
3.3	Thrust and mass flow of a TurboJet engine . . . . .	15
3.4	Example of a liquid fuel rocket engine . . . . .	15
3.5	Architecture of the LEEUAV propulsion system . . . . .	16
3.6	Three-blade propeller, showing blade cross section. . . . .	17
3.7	Propeller blades showing pitch angle near the tip and root. . . . .	17
3.8	Relative airspeed and its direction at a blade section. . . . .	18
3.9	Angles of attack of a blade section. . . . .	19
3.10	Blade of a propeller and forces acting on its section . . . . .	20
3.11	Calculated and measured $F_R$ along the blade length . . . . .	20
3.12	Thrust coefficient versus advance ratio for different pitch angles . . . . .	22
3.13	The two brushless motor configurations . . . . .	23
3.14	Simplified brushless motor diagram . . . . .	24
3.15	PWM representations. . . . .	26
3.16	Comparison of energy densities for various chemistries . . . . .	27

3.17	Characteristic curves for a LiPo battery . . . . .	27
4.1	Output data taken from the System . . . . .	29
4.2	Thrust coefficient versus advance ratio for different p/D . . . . .	31
4.3	Thrust versus diameter of propeller . . . . .	32
4.4	Power coefficient versus advance ratio, p/D a parameter . . . . .	32
4.5	Propeller efficiency coefficient . . . . .	33
4.6	Estimated required electrical power for different propellers . . . . .	36
4.7	Estimated battery duration for different propellers . . . . .	36
4.8	Aero-acoustic wind tunnel at IST . . . . .	37
4.9	Outside view of the test chamber of the aero-acoustic wind tunnel at IST . . . . .	38
4.10	Internal measures of the wind tunnel . . . . .	39
5.1	Design flowchart for the structure . . . . .	41
5.2	Free body diagram for several different ways to measure thrust in a beam . . . . .	42
5.3	Turnigy thrust stand . . . . .	42
5.4	Example of a simple thrust measurement . . . . .	43
5.5	Sketch of how the option with the table works . . . . .	43
5.6	First version of the test rig . . . . .	44
5.7	Second version of the test rig. . . . .	44
5.8	Proposed solution for the measuring system of the test rig. . . . .	45
5.9	General dimensions for the structure . . . . .	46
5.10	Different profiles used in the structure . . . . .	47
5.11	Free body diagram of the forces presented in the main beam. . . . .	49
5.12	Shear and bending moment for the main beam . . . . .	50
5.13	Cross section for the main beam . . . . .	51
5.14	FE study for the main beam using different materials. . . . .	52
5.15	Free body diagram for the rear beam . . . . .	52
5.16	Rear beam load diagram. . . . .	53
5.17	FE study for the rear beam using different materials. . . . .	54
5.18	Free body diagram of the pin in the main beam of the structure. . . . .	55
5.19	Rotation pin load diagram. . . . .	55
5.20	Free body diagram of the forces present in the support beam . . . . .	57
5.21	Load diagram for the support beam . . . . .	58
5.22	FE study for the support beam using different materials. . . . .	59
5.23	Complete support structure for the motor in the main beam . . . . .	60
5.24	FE simulation of the designed motor support cross . . . . .	61
5.25	Sketch of the foundation of the structure . . . . .	61
5.26	Main characteristics of the support foundation . . . . .	62
5.27	Top View shielding square beam . . . . .	63

5.28 Aerodynamic study of the airfoil EPPLER 863 STRUT AIRFOIL using the software XFOIL	64
5.29 Hot wire cutting machine present in the laboratory	64
5.30 Different phases of the cutting process of the airfoil	65
5.31 Final design for the aerodynamic shielding	66
5.32 Process of assembling the structure of the test rig	67
6.1 Load Cell	69
6.2 Voltage and current sensor	69
6.3 Reflective optical sensor Vishay CNY70	70
6.4 Temperature sensor Analog Devices TMP36GZ	70
6.5 Differential sensor Freescale Semiconductor MPXV7002DP	71
6.6 Servo tester used in the first test runs	71
6.7 Block used on LabView to generate the PWM signal to control the motor speed	72
6.8 Nationals Instruments NI PCIe-6321	72
6.9 Electrical layout of the test rig	73
6.10 Graphical Interface for Operating the test rig	74
6.11 Labview block arrangement	75
6.12 Example of data recorded	75
7.1 Load cell calibration and linear regression result	76
7.2 Structure used for the calibration of the load cell	77
7.3 Screenshots of the developed LabView program for voltage/current sensor calibration	77
7.4 Voltage and current calibration test of the sensors.	78
7.5 Relation of wind tunnel motor frequency with the true wind airspeed	79
7.6 Linear regression applied to the airspeed sensor	79
7.7 Thrust versus rev/min for the APC 14x7E propeller	80
7.8 Thrust coefficient versus rev/min for the APC 14x7E propeller	80
7.9 Motor at N=3000 rev/min for the APC 14x7E propeller	82
7.10 Motor at N=5000 rev/min for the APC 14x7E propeller	83
7.11 Motor at N=7000 rev/min for the APC 14x7E propeller	84



# Nomenclature

## Greek symbols

$\alpha$	Angle of attack
$\beta$	Pitch angle
$\omega$	Angular velocity
$\rho$	Density
$\sigma$	Tensile stress
$\sigma_U$	Tensile ultimate stress
$\tau$	Shear stress

## Roman symbols

$C_D$	Coefficient of drag
$C_L$	Coefficient of lift
$C_P$	Coefficient of power
$C_Q$	Coefficient of torque
$C_T$	Coefficient of thrust
$D$	Drag
$d$	Diameter
$F_R$	Sectional Thrust
$i$	Current
$i_0$	No load current
$K_v$	Electric motor speed constant
$M_{tip}$	Mach number on the tip of the propeller
$N$	Revolutions per minute

$Q$	Torque
$Q_R$	Sectional Torque
$R$	Electric resistance
$r$	Radial distance
$R_e$	Reynolds number
$T$	Thrust
$V$	Forward velocity
$v$	Motor terminal voltage
$V_R$	Resultant airspeed
$p$	Pressure

# Glossary

<b>BEC</b>	Battery eliminator circuit
<b>CAD</b>	Computer-aided design (CAD) is the use of computer systems to assist in the creation and modification analysis of a design.
<b>DC</b>	Direct Current
<b>ESC</b>	Electronic Speed Controller.
<b>FEM</b>	Finite Element Method
<b>GPS</b>	Global Position System
<b>LEEUAV</b>	Long Endurance Electric Unmanned Aerial Vehicle.
<b>LiPo</b>	Lithium Polymer
<b>PWM</b>	Pulse Width Modulation.
<b>RPM</b>	Revolutions per minute
<b>UAS</b>	An Unmanned Aerial System (UAS) refers to the systems involved in a UAV control such as the UAV itself, the control station or the ground staff.
<b>UAV</b>	An Unmanned Aerial Vehicle (UAV) is an aircraft without a human pilot on board.





# Chapter 1

## Introduction

### 1.1 Motivation

Nowadays, with the increasing price of fossil fuels, the demand for the usage of electricity has been rising in the past years. In the aviation industry, the development of unmanned airplanes has grown a lot not only because of their efficiency but also because of their agility and capability of adapting to almost every environment. The simplicity and improvement of their components made the Unmanned Aerial Vehicle (UAV) one of the most important tools for the mass emergence of unmanned vehicles. One of the first organization to use it in their operations was the American Army. With a wide range of functions, nowadays the UAVs are used in a wide range of functions such as military and civil applications, delivering mail, recognition operations and also detection of forest fires.

The technology related to UAVs evolved exponentially in the last decade due to the investment made by the military branch that needed technological developments in surveillance and reconnaissance. Today electric UAVs have ability to withstand longer flights (thanks to Lithium polymer batteries) and can be equipped with GPS systems, high-sensors quality and / or similar devices, or even weapons. One of the most important components of a UAV is the propulsion system, which is responsible for 90 % of the energy consumption of the vehicle. It is necessary to use an efficient propulsion system and suitable for its gross weight to ensure higher flight times and greater safety in the event of unforeseen conditions during flight.

This thesis aims to make good use of the current computer capabilities to study and comprehend the main features of the propulsion system of an UAV. With a well designed propulsive system, fitted to each different case, it will be possible to have a more efficient flight. To achieve this, it will be necessary to design a test rig. This design will be based on the physical testing limits that are proposed for this test bench. The complete structure will be assembled inside the aero-acoustic wind tunnel at IST. To measure all the output data produced by the motor, the test rig will be equipped with several sensors that will allow the user monitor and record all the data during a test.

## 1.2 The LEEUAV Project

This thesis takes part in a project proposal by several major institutions units belonging to the research line of Aeronautics and Space of LAETA (Associated Laboratory for Energy, Transports and Aeronautics), namely CCTAE(Center for Aerospace Science and Technology), AEROG (Aeronautics and Astronautics Research Center) and IDMEC(Institute of Mechanical Engineering. Lisbon). The project is entitled *Long Endurance Electric UAV* (LEEUAV)[1] and its goals are to develop a low cost, small footprint, easy to build and maintain multirole electric UAV, capable of being deployed from short airfields and highly flexible in such ways that it is able to adapt to different civilian surveillance missions, thus not being restricted to specific mission profiles. The mission of this project can be summarized in:

- Takeoff in a very short distance (in 8 meters), or hand launched (in 3 meters);
- Climb 1000 meters to cruise altitude in 10 minutes;
- Fly for 8 hours in the equinox at low speed defined by system efficiency but greater than 7m/s;
- Descent during 29 minutes without power;
- Landing in the field.

The current LEEUAV platform can be seen in Fig. 1.1.



Figure 1.1: Long Endurance Electric UAV[1]

The main goal of this Thesis is to build a structure capable of testing several different configurations of a propulsive system in order to meet the mission of the LEEUAV. With the structure designed, it will be possible to test a good range of configurations in both dynamic and static environment.

## 1.3 Objectives

This thesis covers a wide range of contents regarding Mechanical Engineering. The first main goal is to achieve basic knowledge on the area of measuring data. Before the designing of the Test Rig starts, it is necessary to study and comprehend the main features of the propulsion system of the UAV. It is crucial to know what parameters the Test Rig need to measure from the propulsive system such that the

tests can achieve a good level of accuracy. Also, with the resulting output, it would be possible to assess optimal operating points.

About the design of the Test Rig, first the author need to have in consideration about the area where the Test Rig is going to be mounted but also the testing limits for the test rig. Since the range of tests to be done include static and dynamic environments, the Test Rig will be mounted in a wind tunnel. First it would be conducted several theoretical computations to estimate the maximum values of output that the propulsive system will generate. It was decided that the maximum possible diameter for the propeller would be 27 inches and for the motor 63 millimetres in diameter. After this, it will be performed the drawing of the complete structure aided with a CAD software. The student will have to perform a mechanical verification to the structure, using a numerical software, to ensure that the Test Rig agrees all the specifications that was built for, applying a correct safety factor. Also, it will be necessary to design an aerodynamic shielding for protecting the structure of the aerodynamic forces generated during a dynamic test.

After the design of the Test Rig, the student will perform static and dynamic tests of a demonstrative propulsive system for verification purposes of the experimental apparatus developed.

## **1.4 Contents**

In chapter 2, a brief introduction will be made concerning the history of flight and UAV.

Then, in chapter 3 it is briefly described the different types of propulsive systems, focusing the electric motors. It is given a short introduction about the LEEUAV propulsive system and then all the major propulsive components are described.

In chapter 4, after presenting the theoretical background about electric motors, it is then studied and presented the testing limits of the test rig. Based on information provided by the propulsive components manufacturers, it is presented the maximum values that will be measured on the test rig.

Then, in chapter 5 is designed the test rig. It is performed several load analysis for each structural component of the test rig, based on the measuring limits of the test rig. It is presented the CAD version of the structure and described the assembly and construction of the structure.

In chapter 6, all the sensors and the control made in the test rig are presented.

The chapter 7 is dedicated to the test rig testing. The calibration of the sensors, the tests performed on the test rig are described in this chapter.

Finally, in chapter 8 it is discussed the progress done and the results obtained.



## Chapter 2

# Hystorical Perspective of UAVs

### 2.1 History of Flight

Human beings have always wanted to fly. A great example of such desires and ambitions is the Greek mythology tale of Daedalus and Icarus.

When the age of flight finally did arrive, it came from an unexpected direction that had nothing to do with wings. The invention of the balloon created a wave of excitement that swept across Europe and America. Although the balloon would be put to good use by science and the military, it could only travel where the wind blew it. The age-old dream of wings remained very much alive [2].

Not being naturally apt to fly, human beings started experimenting and thinking of ways of experiencing flight[3]. Eventually some investigators began to discover and define some of the basics of rational aircraft design. Most notable of these was Leonardo da Vinci, although his work remained unknown until 1797, and so had no influence on developments over the next three hundred years. While his designs were at least rational, they were not based on particularly good science[4]. From the last years of the 15th century on he wrote about and sketched many designs for flying machines and mechanisms, including ornithopters, fixed-wing gliders, rotorcraft and parachutes. His early designs were man-powered types including ornithopters and rotorcraft, however he came to realise the impracticality of this and later turned to controlled gliding flight, also sketching some designs powered by a spring. There is no definite proof that this machine was actually built but its working mechanisms, as seen in Figure 2.1, were to mimic the flapping wing movement of birds[5].



Figure 2.1: One of Leonardo's sketches[6]

In 1709 Bartolomeu de Gusmão presented a petition to King John V of Portugal, begging for support for his invention of an airship, in which he expressed the greatest confidence. The public test of the machine, which was set for June 24, 1709, did not take place. According to contemporary reports, however, Gusmão appears to have made several less ambitious experiments with this machine, descending from eminences. It is certain that Gusmão was working on this principle at the public exhibition he gave before the Court on August 8, 1709, in the hall of the Casa da India in Lisbon, when he propelled a ball to the roof by combustion[7].

Later in the second half of that century, the Montgolfier brothers designed and built hot air balloons that ascended and flew several kilometers across Paris[8]. Human beings were one step closer to conquer the skies. However, despite the success of actually flying through the skies, those balloons were not meant to achieve high velocities and maneuverability. This feat was achieved by George Cayley in 1799 and his airplane designs included a fixed wing to generate lift, a propulsion system to produce thrust and a cruciform tail for stabilization purposes[9].

## 2.2 First Powered Flight

Later in the twenty century, in camp at Kill Devil Hills, the Wright Brothers endured weeks of delays caused by broken propeller shafts during engine tests. After the shafts were replaced (requiring two trips back to Dayton), Wilbur won a coin toss and made a three-second flight attempt on December 14, 1903, stalling after takeoff and causing minor damage to the Flyer. Following repairs, the Wrights finally took to the air on December 17, 1903 (Fig. 2.2), making two flights each from level ground into a freezing headwind gusting to 27 miles per hour (43 km/h). The first flight, by Orville at 10:35 am, of 120 feet (37 m) in 12 seconds, at a speed of only 6.8 miles per hour (10.9 km/h) over the ground, was recorded in a famous photograph. The next two flights covered approximately 175 and 200 feet (53 and 61 m), by Wilbur and Orville respectively. Their altitude was about 10 feet (3.0 m) above the ground[10].

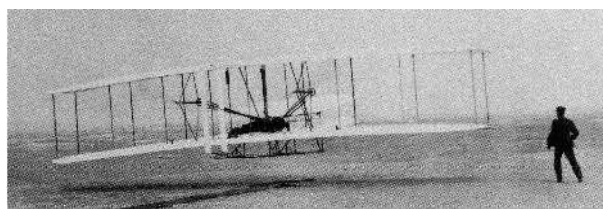


Figure 2.2: Wright Brother's Flyer III[11]

## 2.3 The Uprising of UAVs

In 1916, less than 15 years after the Wright brothers historical flight, the first modern unmanned aircraft was demonstrated. It was the Hewitt-Sperry Automatic Airplane, named after the two inventors that designed it. This aircraft could not have become a reality without the previous work of Sperry on gyroscopic devices that were needed to provide flight stabilization. Sperry managed to attract the interest of the US

Navy resulting in the development of the Curtiss-Sperry Aerial Torpedo, while at the same time the US Army Air Force sponsored the Liberty Eagle Aerial Torpedo of Charles Kettering shown in Fig. 2.3. Due to technical problems and lack of accuracy, interest in “automatic” planes was lost but the potential for use of remotely operated drones for target practice was soon realized[12].



Figure 2.3: The USAF Liberty Eagle Aerial Torpedo (Photo Credit: National Museum of the USAF)[13].

Remote operation required the perfection of radio control, a concept proposed and demonstrated in 1895 and 1898, respectively, by Tesla[14]. Yet again private industry spurred developments, when actor Reginald Denny opened his “Reginald Denny Hobby Shops” in 1934 and started selling radio controlled airplanes. A few years later he demonstrated his work for the US Army that led to the development of a very successful target drone used extensively during WWII[12].

In the late 1960s, the CIA was involved in its own hypersonic, long-range reconnaissance UAV, designed to be launched from another “mother” aircraft. The D-21 Tagboard program was mired with technical problems, accidents and failed missions that led to its ultimate cancellation in the early 1970s[12]. In parallel with US efforts, the Soviet Air Force developed its own reconnaissance drones. The first system was the TBR-1 based on a popular target drone and it was soon followed by the DBR-1 that allowed for higher range and capabilities[13]. The DBR-1 was not designed to be fully recovered, instead when it reached the recovery area it dumped fuel, ejected the nose containing the sensor package and the rest of the airframe crashed. As a result, the DBR-1 involved high operation costs which led to its replacement in the mids 1970s by the Tu-141/143, a mid and short range, respectively, reconnaissance drone that were fitted with parachutes for recovery.

In Europe, the unmanned system of choice of the time was funded by Canada and the UK and was developed by Canadair [13]. This resulted in the CL-89 Midge that was also acquired by the French and German armies. It was designed to follow a pre-programmed course, take photographs (day or night) and return to be recovered by parachute [13].

In the 21st century, the military role of unmanned aircraft systems is growing at unprecedented rates. In 2005, tactical- and theater-level unmanned aircraft alone had flown over 100,000 flight hours in support of Operation Enduring Freedom and Operation Iraqi Freedom, in which they are organized under Task Force Liberty in Afghanistan and Task Force ODIN in Iraq. One of these examples is the General Atomics MQ-1 Predator (see Figure 2.4). It is an unmanned aerial vehicle (UAV) built by General Atomics and used primarily by the United States Air Force (USAF) and Central Intelligence Agency (CIA). Initially conceived in the early 1990s for reconnaissance and forward observation roles, the Predator carries

cameras and other sensors but has been modified and upgraded to carry and fire two AGM-114 Hellfire missiles or other munitions. The aircraft, in use since 1995, has seen combat over Afghanistan, Pakistan, Bosnia, Serbia, Iraq, Yemen, Libya, Syria, and Somalia.



Figure 2.4: General Atomics MQ-1 Predator at Paris Air Show 2007 (Photo Credit: David Monniaux)

Rapid advances in technology are enabling more and more capability to be placed on smaller airframes, which is spurring a large increase in the number of Small Unmanned Aircraft Systems (SUAS) being deployed in the battlefield. The use of SUAS in combat is so new that no formal DoD wide reporting procedures have been established to track SUAS flight hours. As the capabilities grow for all types of UAS, nations continue to subsidize their research and development, leading to further advances and enabling them to perform a multitude of missions. UAS no longer only perform intelligence, surveillance, and reconnaissance missions, although this still remains their predominant type. Their roles have expanded to areas including electronic attack, strike missions, suppression or destruction of enemy air defense, network node or communications relay, combat search and rescue, and derivations of these themes. These UAS range in cost from a few thousand dollars to tens of millions of dollars, with aircraft ranging from less than one pound to over 40,000 pounds.

Another major player in the area of unmanned aircraft was the Israeli Air Force, that acquired and operated a squadron of American drones for reconnaissance purposes during the Yom Kippur War[13]. Later the Israeli Aircraft Industries and Tadiran developed their own aircraft, the Scout (see Figure 2.5 ) and Mastiff, respectively[12].The Mastiff was the basis of the very popular Pioneer system and the Israeli designs have also influenced the construction of the Predator and Shadow UAS[14].



Figure 2.5: The Israeli Aircraft Industries Scout drone (Photo Credit: Wikimedia Commons User Bukvoed).



## 2.4 UAVs in Portugal

The purchase of two UAVs by Polícia de Segurança Pública (PSP), was authorized on 19 July 2014 by former national director of the corporation and was the subject of a contract classified as secret. The contrast between the secret of the contract and the display of your subject before the whole world is just one of the surprises of the current betting the PSP in terms of their equipping special units. The purchase of unmanned aerial vehicles was done by direct negotiation with the Portuguese company Tekever[15], for about two hundred thousand euros. The drones purchased come equipped with two video cameras and tools for remote viewing, featuring autonomous flight of two hours, a range of 20 kms and high tech communications. The drones, shown in fig 2.6, weigh five kilograms, have a wingspan of 1.8 meters and are hand thrown, landing with the aid of a parachute. The decision to buy these devices relates to the fact that PSP deems necessary to support its activities in the field of crime prevention. Was made a following protocol signed between the corporation and the Tekever, in May 2012, with a view to exploring ways unmanned aerial.



Figure 2.6: UAV AR1 Blue Ray acquired by PSP[15].

One of the projects that is being developed by the Portuguese Air Force along with other two main Institutes is the PITVANT project. This concerns the development of vehicles, tools, technologies, know how and operational concepts for the Portuguese Air Force (PoAF). The project builds on the experience accumulated since 2006 by Portuguese Air Force Academy (PoAFA) and the Underwater Systems and Technologies Laboratory (LSTS) from University of Porto on the design, implementation, testing and demonstration of different types of UAS in a wide spectrum of military/civil missions[16]. Since 2002 the Portuguese Air Force Academy Research Centre (CIAFA) is actively participating in multinational European Commission sponsored projects of the fifth, sixth and seventh Framework Programmes [16].



Figure 2.7: All the UAVs built under the PITVANT Project (Photo Credit: Portuguese Air Force Academy).

Currently in this project are operating and developing different UAVs: ANTEX X03, ANTEX X02, a Silver Fox (from Advanced Ceramics Research), trainers and hand launched flying wing, as shown in Fig. 2.7. ANTEX X02 (see Fig. 2.8) is a half-sized version of the ANTEX-X03. ANTEX X02 and the trainers share the same computational and sensor configurations. Both airframes use the a OS 91-FX engine (15cc and 2.9HP). The maximum payload weight is in the order of 5kg and the maximum flight time is close to 80 minutes. The flying wing is equipped with an electric motor and a video camera. The design aims to allow up to 1kg of payload, a nominal velocity of less than 50 knots and one hour maximum flight time. The wingspan is about 2 meters. ANTEX-X02 and ANTEX-X03 are being optimized in order to increase their endurance.



Figure 2.8: Alpha UAS (Photo Credit: Portuguese Air Force Academy)

Another project that the FAP is currently developing is the construction of the UAV UAS30 (see Figure 2.9). This 25 kilogram UAV will takeoff with the help of a catapult and lands with the support of a net. The project took off about two years ago, with a challenge by EDP, intended to test the use of small drones for inspection of electric power lines. The UAS30 was developed in partnership with the CEIIA (Center for Excellence and Innovation of the Automotive Industry in Matosinhos) to meet the challenge of EDP and also to address many other areas that may benefit from the use of drones. The UAS30 has been tested on missions with speed of 50 km/h. To achieve this speed, deliberately low to ensure the capture of images in the best conditions, researchers from the Air Force Academy resorted to larger wings.



Figure 2.9: UAS 30 (Photo Credit: Portuguese Air Force Academy)

Besides these projects, Portugal has also other companies that design UAVs and components for them. One of these companies is UAVision[17], that was pioneer in the construction of UAVs and quadcopters. Their core business focus on UAVs but also in projects with public interest. Their most awarded product it is the quadcopter Spyro (see Figure 2.10). This quadcopter not only operates almost with no noise but also easily merges with the operational scenario as it is capable of sustaining high winds and

adverse weather. The Spyro represents a new concept of VTOL (Vertical Take-off and Landing) UAV.



Figure 2.10: Spyro UAV designed and built by UAVision[17].

Another important company in the area of UAS for the Aeronautics is SPIN.Works[18]. Taking advantage of its multi-disciplinary competences, they create, develop and deploy innovative, multi-disciplinary and cost-effective solutions, in the areas of structures, mechanisms, guidance navigation and control (GNC) systems, simulation, remote detection systems, and UAVs. FORCAST is a SPIN.Works project with the purpose of building a portable Ground Control Station for unmanned aerial vehicles applied to forest management, specifically for two missions: fire detection, tracking and monitoring, and forest inventory. The project involves the development both the hardware and software components of the ground station, as well as a field test campaign conducted in a realistic scenario. The small unmanned aerial vehicles used for testing have also been entirely developed at SPIN.Works. AN example of such system is shown in Fig. 2.11



Figure 2.11: Spin.Works Integrated UAV system for forest management [18].

## 2.5 Future Work in UAVs

In the military sector, a 2012 Congressional Research Service (CRS) report indicated that in the future, UAVs may be able to perform a variety of tasks beyond their present roles in intelligence, surveillance, reconnaissance and strikes; the CRS report listed resupply, combat search and rescue, aerial refueling, and air to air combat ("a more difficult future task") as possible future undertakings [19].

In the private sector, initial attempts at commercial use of UAVs, such as the Tacocopter company for the food delivery, were blocked by FAA regulation[20]. Amazon.com founder Jeff Bezos December 2013 announcement that Amazon is planning rapid delivery of lightweight commercial products using UAVs was met with skepticism, with perceived obstacles including federal and state regulatory approval,

public safety, reliability, individual privacy, operator training and certification, security (hacking), payload thievery, and logistical challenges[21]. In July 2014 it was revealed Amazon was working on its 8th and 9th drone prototypes, some that could fly 50 miles per hour and carry 5-pound packages, and had applied to the FAA to test them[22].

In December 2013, in a research project of Deutsch Post AG subsidiary DHL, a sub-kilogram quantity of medicine was delivered via a prototype Microdrones “parcelcopter,” raising speculation that disaster relief may be the first place the company will use the technology.



Figure 2.12: Prototype “parcelcopter” of German postal and logistics group Deutsche Post DHL.

# Chapter 3

## Propulsion Systems

### 3.1 Types of Propulsion Systems

Aircraft engines, together with associated fuel tanks and related hardware, are referred to as propulsion systems. The purpose of the propulsion system is to generate a thrust force that propels the aircraft in flight. Although engines and propulsion systems are extremely complicated, detailed knowledge of the engine specifications is not required to analyse flight properties of an aircraft. Rather, the key features for the study of steady flight are the maximum thrust (or the maximum power) that the engine can produce and the rate at which fuel is burned to produce a given thrust level (or power level).

Broadly speaking, airplane propulsion system can be classified into four categories: Piston Engines, Jet Engines, Rocket Engines and Electric Motors. The categories are briefly described in the next sections. The appropriate system depends on the altitude and speed of the aircraft, as illustrated in Fig. 3.1

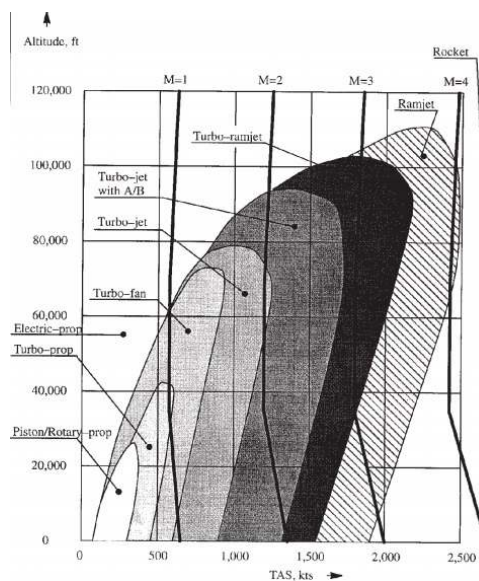


Figure 3.1: Aircraft propulsion systems in relation to flight envelopes.[23]

### 3.1.1 Piston Engines

In piston engines, the combustion process is intermittent as opposed to continuous. Piston engines are normally configured as four-stroke, two-stroke or rotary engines using either spark ignition or compression ignition. The latter are more commonly referred to as Diesel engines.

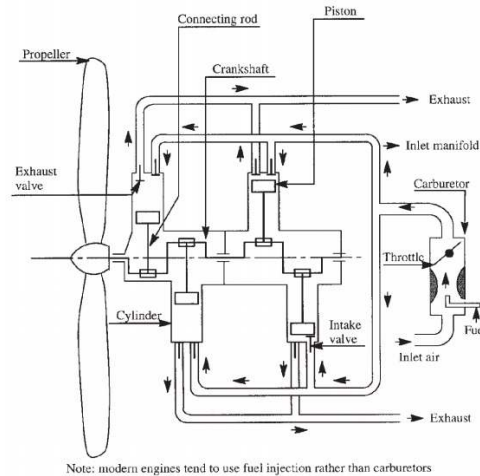


Figure 3.2: Typical cross-section of a four-cylinder piston engine.[23].

The pistons are connected to the crankshaft with a connecting rod. Each piston moves back and forth inside a cylinder with two valves: an inlet valve and exhaust valve. The inlet valve opens and closes as dictated by a so-called cam-shaft (not shown in Figure 3.2) which is driven off the crankshaft. When the inlet valve opens it admits a fuel-air mixture which in turn comes from the inlet manifold. The inlet manifold is fed by a carburetor which is controlled by a throttle. In modern engines, the fuel is injected directly into the cylinder without passing through a carburetor (fuel injection).

### 3.1.2 Jet Engines

A jet propulsion engine is based on Newton's third law of motion, namely, that to every action there is always an equal and opposite reaction. A jet propulsion device uses a gas turbine engines where Newton's third law of motion can be applied in different ways, resulting in different types of gas turbine engines. A jet engine forces the incoming finite air-jet stream to accelerate. It works on the principle that any device forcing a jet stream to accelerate will in turn experience an equal and opposite force of reaction as thrust. The thrust produced by the engine can be calculated by the rate of change of momentum it imparts to the air-jet stream as shown in Fig. 3.3. The physical mechanism by which an air stream, or any other fluid medium, communicates force to the solid surface is through surface pressure and skin friction forces acting at each point over over the surface. If the axial components of these two forces are added and integrated over the complete surface of the engine, the thrust force acting along the axis of the engine is obtained. The principle of producing thrust by a propeller or fan is also the same.

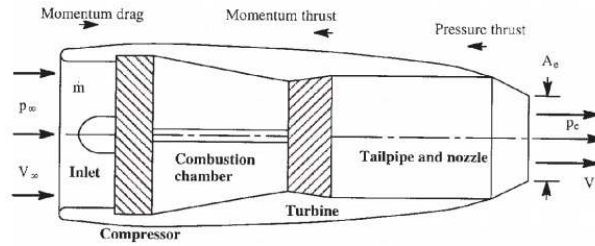


Figure 3.3: Thrust and mass flow of a TurboJet engine.[23].

### 3.1.3 Rocket Engines

At very high altitudes, where air-breathing engines are no longer practical, the rocket engine offers a viable alternative method of aircraft propulsion. Fundamentally, there are two types of rockets: liquid fuel and solid fuel rockets. An example arrangement for a liquid fuel rocket engine is given in Fig. 3.4.

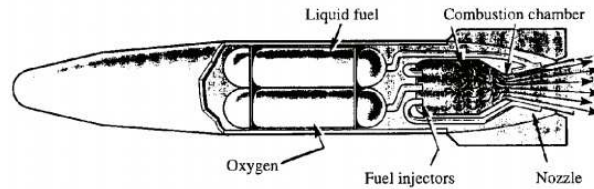


Figure 3.4: Example of a liquid fuel rocket engine (Courtesy of Rolls-Royce plc).

Liquid oxygen and fuel are pumped via a system of lines and valves into a combustion chamber. Once ignited, combustion is continuous until either oxygen or fuel supply is shut off. In most instances the fuel is used to cool the nozzle before being pumped into the combustion chamber. The injectors must be designed so that the oxidizer and the fuel are properly mixed. The combustion process typically yields very high temperatures and pressures.

### 3.1.4 Electric Motors

A significant advantage of electric motors is their rather vibration-free and quiet operation. A disadvantage has been their high weight per unit power output. With the advent of rare earth magnets, electric motors are now considerably lighter than two decades ago. For that reason, they are a candidate for propulsion of certain classes of vehicles. An example is the solar-cell/electric-motor/propeller system used in UAVs. A major problem with electric motor propulsion still is the weight associated with the energy storage (i.e. battery) and/or energy generation system.

## 3.2 LEEUAV Propulsion System

Following what was described in the previous chapter, we will want a propulsion with an high efficiency but also reliable system. Since the mission requirements of the LEEUAV are derived from civilian surveillance applications, such as forest, coast or border patrol, the logical choice will be a brushless motor. This will allow to the UAV to generate a constant thrust linked with an higher efficiency but also an higher

ratio of power to weight. In this thesis the propulsion system will be powered by a power supply, however the LEEUAV will be powered by Lithium Polymer batteries but also from Solar panels.

The propulsion system integrated in the LEEUAV consists of six main components: the solar panels, the solar charge controller, the battery, the speed controller, the electric motor and the propeller. Each of these components has their own performance characteristics and regions of maximum efficiency. The selection of each component is critical in achieving an overall propulsion system which is both efficient and suited to the LEEUAV's mission requirements.

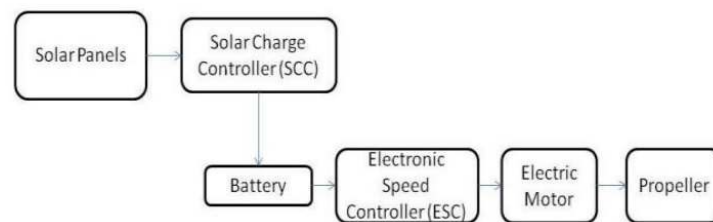


Figure 3.5: Architecture of the LEEUAV propulsion system[1]

## 3.3 Propulsion Components

### 3.3.1 Propellers

The propeller can be placed either in the front or at the rear of the aircraft. The propellers pulling from the front of the aircraft are quite common and they are sometimes referred to as *tractors*, whereas those attached at the back of the aircraft, for pushing forwards, are referred to as *pushers*. In both cases the principle of operation of a propellers and its basic features remain the same.

#### Principle of Operation

The purpose of the propeller is to change the rotary motion of the shaft of a motor into the forward motion of the aircraft. The rotation of the propellers converts the torque (brake power) of the shaft into the thrust power of the aircraft. These conversions are done by drawing a large mass of air and giving it a small increment of velocity (about 10m/s) so that the change in momentum flux of air imparts thrust force on the propeller blades. The imparting of the thrust is through the modification of pressure and skin friction at each point on the surface of the blade; the sum of these components along the axis of rotation of the propeller yields the thrust force. This thrust force when multiplied by the forward airspeed of the aircraft gives thrust power. Thus, the propeller is a device for absorbing the shaft power (brake power) of the engine and generating the thrust power form propelling the aircraft.

#### Propeller Geometry and Pitch

A propeller has blades in the radial directions whose number may vary from two to five depending on the designer; three or four blades are generally quite common. A three-blade propeller is shown in Figure



3.6. All propeller blades are exactly the same shape and are mounted on a conical hub or spinner. The aerodynamic design of a blade requires that it should be able to produce maximum thrust power with minimum consumption of drag power. This design requirement is similar to that for a wing of maximum lift with a minimum drag. A cross section of the propeller blade is very much like that of a low-drag or high subsonic airfoil. The angle between the plane of rotation (the plane of a propeller) and the chord line of the airfoil at any section of the blade is called the *pitch angle* or simply *pitch* and is denoted by  $\beta$ . The pitch angle is not constant along the length of the propeller blade. That is,  $\beta = \beta(r)$ , which means that the pitch angle  $\beta$  is a function of the radial distance  $r$ , which may be measured from the root of the propeller. Figure 3.7 shows the pitch angle is the least (close to zero) at the tip but increases to nearly  $\pi/2$  when one approaches closer to the root of the propeller.

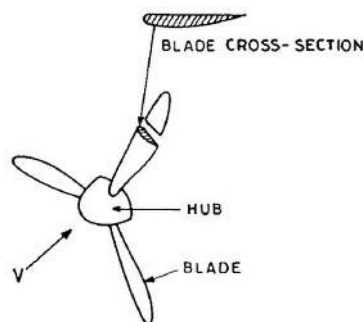


Figure 3.6: Three-blade propeller, showing blade cross section.[23]

### Relative velocity and Its Direction

During the motion of an aircraft, each section of the blade experiences simultaneously the two different velocities, which are generally orthogonal to each other. One is the circumferential velocity  $r\omega$  in the plane of rotation, where  $\omega = 2\pi N$  is the angular velocity of rotation of the propeller that is making  $N$  number of revolutions per unit of time.

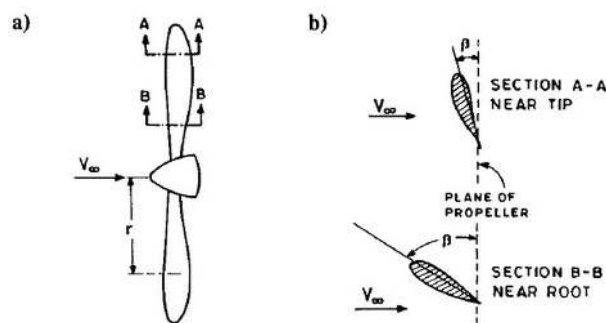


Figure 3.7: Propeller blades showing pitch angle near the tip and root: a) side view of propeller blades and b) top view of airfoil sections.[23].

The other is the forward velocity  $V$  normal to the plane of rotation of the propeller, due to the motion of the aircraft. Each blade section (airfoil), faces the relative (resultant) airspeed  $V_R$ , which is the vector sum of the velocities  $V$  and  $r\omega$  as shown in Figure 3.8. The magnitude of  $V_R$  and its direction  $\phi$  from the plane of rotation are given by:

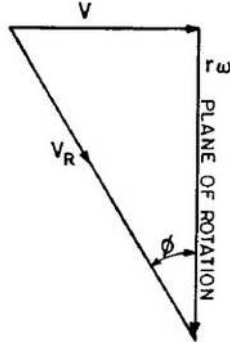


Figure 3.8: Relative airspeed and its direction at a blade section.[23].

$$V_R = \sqrt{V^2 + (\omega r)^2} \quad \phi = \tan^{-1} \left( \frac{V}{r\omega} \right), \quad (3.1)$$

The circumferential velocity  $r\omega$  can be increased either by increasing  $r$  by moving toward the tip of a blade, or increasing  $\omega$  by increasing the rpm of the propeller. The effect of increasing the circumferential velocity is to reduce  $\phi$  which brings the relative airspeed closer to the plane of rotation. Similarly, increasing the airspeed  $V$  brings the magnitude and direction of  $V_R$  closer to that of  $V$ .

Equation 3.1 can be rewritten for the tip ( $r=R$ ) as:

$$M_{R,tip} = M \sqrt{1 + \left( \frac{\pi}{J} \right)^2}, \quad (3.2)$$

$$\phi_{tip} = \tan^{-1} \left( \frac{J}{\pi} \right), \quad (3.3)$$

where  $M_{R,tip}(= V_{R,tip}/a)$  and  $M(= V/a)$  are the Mach numbers corresponding to the resultant and forward velocities, respectively, and  $a$  is the local speed of sound. The quantity  $J$  is called *advance ratio of the propeller*, which is defined as  $J = V/ND$  where  $D(= 2R)$  is the diameter of the propeller whose radius is  $R$ . The advance ratio is an important parameter of propeller motion.

### Angle of Attack

The angle between  $V_R$  and the chord line is defined as the *angle of attack*  $\alpha$  of the airfoil or blade section. As seen from Figure 3.9a the angle of attack is given by:

$$\alpha = \beta - (\phi + \alpha_i), \quad (3.4)$$

Since the angle of attack must be positive to produce a reasonable thrust, it follows that  $\beta$  must be greater than  $\phi$ . The pitch  $\beta$  at a blade section is an important geometric parameter of the propeller because it fixes the angle of attack at the section for a given  $\phi$  or advance ratio  $J$ .

In cases where  $V$  is greater than or comparable to  $r\omega$ , the angle  $\phi$  may exceed  $\beta$  and, therefore, the angle of attack  $\alpha$  would become negative as shown in Figure 3.9b. At such blade sections the thrust would become negative, which is unwanted. It can be easily seen that such situations may arise either

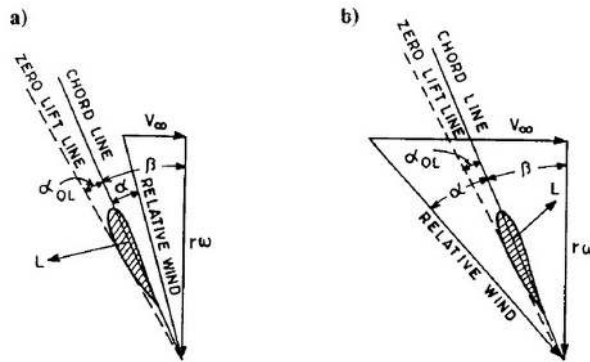


Figure 3.9: Angles of attack of a blade section: a) +ve in advance and b) -ve in advance.[23].

near the roots of the blades or when the propeller is rotating slowly during forward motion.

### Fine-Pitch and Coarse-Pitch Propellers

The pitch angle of a propeller blade decides whether it is a fine pitch or a coarse-pitch propeller. If the pitch angle  $\beta$  is small, this is called fine pitch, and the large pitch is referred to as coarse pitch. Fine pitch is also sometimes called low pitch and coarse pitch is sometimes called high pitch. In modern aircrafts, the pitch angle can be changed during flight. As the pitch changes from fine to coarse at a given rpm, the thrust increases.

A propeller set for fine pitch has less drag (in the plane of rotation), or torque, and consequently rotates at higher speed, enabling the engine to develop greater power. Therefore, a propeller set for fine pitch gives the aircraft better takeoff and climb performance. A coarse pitch gives better performance for high-speed cruising and high-altitude flight.

### Thrust and Torque Calculations of a Propeller

The rotation of the propeller in air produces aerodynamics forces due to changes in pressure and skin friction at each point on the surface of the propeller blades. These forces, when resolved along the normal to the plane of rotation, give the thrust force, commonly known as thrust of the propeller, which is responsible for the forward motion of the aircraft. If the momentum of these aerodynamics forces is taken at each point of the propeller about the axis of rotation of the propeller, this gives the torque experienced by the propeller shaft.

It is possible to calculate the thrust and torque theoretically with reasonable accuracy by properly resolving the aerodynamic forces at each section of the blades. First, the forces on a small section  $dr$  of the blade are obtained, then they are integrated along the length of the blades, and finally they are multiplied by the number of propeller blades, as explained below.

Figure 3.10 shows one blade of the propeller and the forces acting on its section. Let  $l$  and  $d$  denote the lift and drag forces, respectively, per unit length of the blade at a radial distance  $r$ . If  $F_r$  and  $Q_r$  are the sectional thrust and torque, respectively, per unit length of the blade, at a radial distance  $r$ , they can be expressed as:

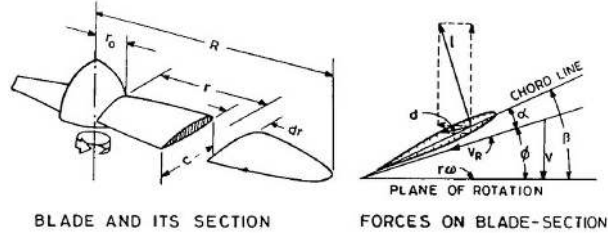


Figure 3.10: Blade of a propeller and forces acting on its section.[23].

$$F_r = l \cos \phi - d \sin \phi \quad Q_r = (l \sin \phi + d \cos \phi)r, \quad (3.5)$$

where the quantity inside the parenthesis in Equation 3.5 is the force per unit span of the blade in the plane of rotation, but normal to the radial direction. Representing the sectional lift and drag coefficient per unit length of the blade by  $C_l$  and  $C_d$  respectively, the  $l$  and  $d$  can be expressed as:

$$l = C_l \rho V_R^2 c / 2 \quad d = C_d \rho V_R^2 c / 2, \quad (3.6)$$

where  $V_R = V / \sin \phi$ . Equations 3.5 can now be written as:

$$F_r = \rho V^2 c (C_l \cos \phi - C_d \sin \phi) r / (2 \sin^2 \phi) \quad Q_r = \rho V^2 c (C_l \sin \phi - C_d \cos \phi) r / (2 \sin^2 \phi), \quad (3.7)$$

The variation in  $F_r$  along the length of the blade is shown in Figure 3.11. The inner portion of the blade close to the hub produces hardly any thrust, which justifies putting a fairly big hub at the center of the propeller. The space inside the hub can be utilized for installing a pitch change actuator system.

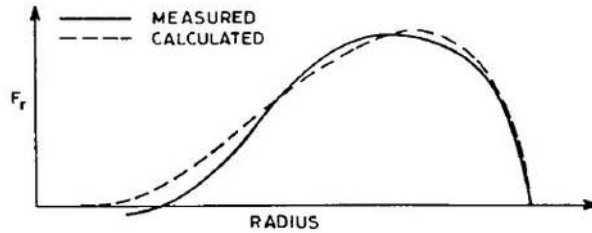


Figure 3.11: Calculated and measured  $F_R$  along the blade length.[23].

The total thrust  $F$  and the total torque  $Q$  produced by the propeller would be respectively, given by:

$$F = B \int_{r_0}^R F_r dr \quad Q = B \int_{r_0}^R Q_r dr, \quad (3.8)$$

where  $B$  is the number of blades of the propeller,  $R$  is the radial distance of the tip of the blade, and  $r_0$  is the external radius of the hub where the root of the blade is fixed. The thrust and torque, respectively, can now be obtained as:

$$F = B(\rho V^2 / 2) \int_{r_0}^R (c / \sin^2 \phi) (C_l \cos \phi - C_d \cos \phi) dr, \quad (3.9)$$

$$Q = B(\rho V^2/2) \int_r^R (c/\sin^2 \phi)(C_l \sin \phi + C_d \cos \phi)rdr, \quad (3.10)$$

where the quantities inside the integral sign vary non-linearly along the radial direction. It is generally not possible to evaluate these integrals analytically. The determination of  $F$  and  $Q$  depends on the accuracies at which  $C_l$  and  $C_d$  can be calculated. The sectional lift and drag coefficients are calculated by either the blade element theory or vortex theory, which have been developed for a propeller after the earliest and simplest Rankine-Froude momentum theory of the propeller[23].

### Propeller Parameters

The important characteristic parameters of a propeller are its advance ratio,  $J$ , thrust coefficient  $C_T$ , torque coefficient  $C_Q$ , power coefficient  $C_P$  and the propeller efficiency  $\eta$ . Similar to many other aerodynamic problems, the aerodynamics of the propeller also make it convenient to express the thrust  $T$ , the torque  $Q$ , and the power  $P$  in suitable non-dimensional forms. If  $D$  represents the diameter of the propeller making  $N$  revolutions per unit of time, take the reference length as  $D$ , reference area as  $D^2$ , reference velocity as  $ND$  and the reference pressure as  $\rho(ND)^2$ . The non-dimensional coefficients of thrust, torque and power can be respectively, defined as:

$$C_T = \frac{F}{\rho N^2 D^4}, \quad (3.11)$$

$$C_Q = \frac{Q}{\rho N^2 D^5}, \quad (3.12)$$

$$C_P = \frac{P}{\rho N^3 D^5}, \quad (3.13)$$

If the quantities  $C_T$ ,  $C_Q$  and  $C_P$  are known for a specific propeller, the thrust, torque and power of the propeller, or another similar propeller, can be obtained from the following relations, respectively:

$$F = C_T \rho N^2 D^4, \quad (3.14)$$

$$Q = C_Q \rho N^2 D^5, \quad (3.15)$$

$$P = C_P \rho N^3 D^5, \quad (3.16)$$

The thrust, torque and power of a propeller strongly depend on its diameter and rpm, and are directly proportional to the density of air. The coefficients of a propeller's thrust, torque and power would generally depend on the shape of its blade, pitch angle, Reynolds number ( $Re$ ), Mach number and advance ratio, i.e.,

$$C_T = C_F(shape, \beta, Re, M, J), \quad (3.17)$$

$$C_Q = C_Q(shape, \beta, Re, M, J), \quad (3.18)$$

$$C_P = C_P(shape, \beta, Re, M, J), \quad (3.19)$$

Since a propeller is streamlined during rotation, the influence of Reynolds number is very weak. The propellers are generally used well below transonic speeds so that the maximum relative velocity at the tip of the blade is less than the sonic velocity incorporating no compressibility effects. It follows that for a given propeller, the above relations would simplify for:

$$C_F = C_F(\beta, J) \quad C_Q = C_Q(\beta, J) \quad C_P = C_P(\beta, J), \quad (3.20)$$

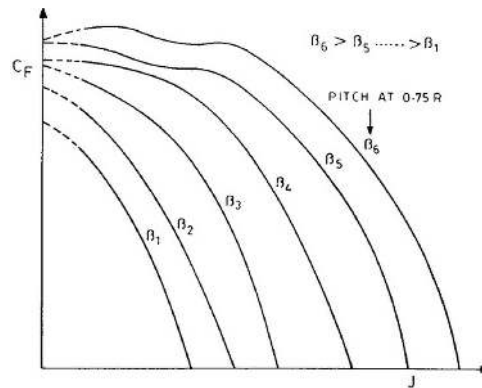


Figure 3.12: Thrust coefficient versus advance ratio for different pitch angles.[23]

This shows that the coefficients  $C_F$ ,  $C_Q$ , and  $C_P$  depend only on the pitch angle  $\beta$  and the advance ratio  $J$ . A typical variation of  $C_F$  against the propeller advance ratio  $J$  for different values of the pitch angles is shown in Figure 3.12. Since the pitch angle varies along the radial direction, the pitch at  $0.75R$  is specified to distinguish different pitch angles of the same propeller.

If Torque  $Q$  is known, the power  $P$  is obtained from the relation  $P = 2\pi NQ$  which after using the equations (3.15) and (3.16) can be written as  $C_P = 2\pi C_Q$ .

### Propeller Efficiency

The propeller efficiency is an important characteristic parameter of the propeller arising due to its rotation in the air. It answers the question, how efficiently is the engine power (power input) converted to thrust power (power output). It is defined as the ratio between power output to power input:

$$\eta_T = \frac{P}{P_e} = \frac{FV}{Q_e 2\pi N}, \quad (3.21)$$

### 3.3.2 Electric Motors

Basically, electric motors are electromechanical machines that convert electrical input power into mechanical output power. The general power supply used in the UAVs is DC (Direct Current).

Most common types are brushed and brushless motors. Brushed motors use mechanical commutation and brushless motors use electronic commutation in order to change the direction of electric current and generate a pulling magnetic force between the stator and the magnets. Brushless motors have numerous advantages such as higher efficiency than brushed motors, longer lifetime, less noise and higher power to weight ratio. Therefore they are more reliable for the UAV applications. Two types of brushless motors exist, In-runner and Out-runner. In the in-runner configuration, the magnets are placed on the shaft of the motor and the windings are at the outer part of the motor. Whereas the out-runner configuration has the magnets turning around the stator. The low inertia of in-runner motor shaft makes them reach to higher rotation speeds compared to out-runner motors. However, the out-runner motors are commonly preferred for their cooler running and high torque specifications which eliminates the use of additional gear-box.

#### Brushless DC Motor Theory

Brushless motors operate by means of stationary current-carrying coils and rotating permanent magnets[24]. Figure 3.13 illustrates the two physical BLDC motor configurations - inner-rotor and outer-rotor. The inner-rotor places the magnets in the centre, surrounded by the coil windings. The outer-rotor places the coil windings enclosed by an outer casing composed of permanent magnets [4]. This configuration is favoured over the inner-rotor configuration in model aviation due to the need for lower energy magnets, reduced copper losses, reduced production costs, and greater rotor inertia [4].

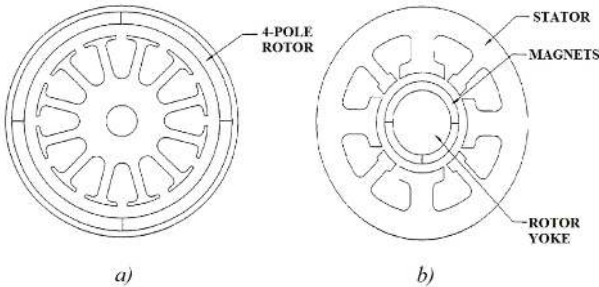


Figure 3.13: The two BLDC motor configurations: a) Outer-rotor BLDC motor, b) Inner-rotor BLDC motor[25].

Figure 3.14 is a simplified illustration of BLDC motor construction. A brushless motor is constructed with a permanent magnet rotor and wire wound stator poles. Electrical energy is converted to mechanical energy by the magnetic attractive forces between the permanent magnet rotor and a rotating magnetic field induced in the wound stator poles. In this example, there are three electromagnetic circuits connected at a common point. Each electromagnetic circuit is split in the centre, thereby permitting the permanent magnet rotor to move in the middle of the induced magnetic field. Most BLDC motors have a three-phase winding topology with star connection. A motor with this topology is driven by energizing

two phases at a time.

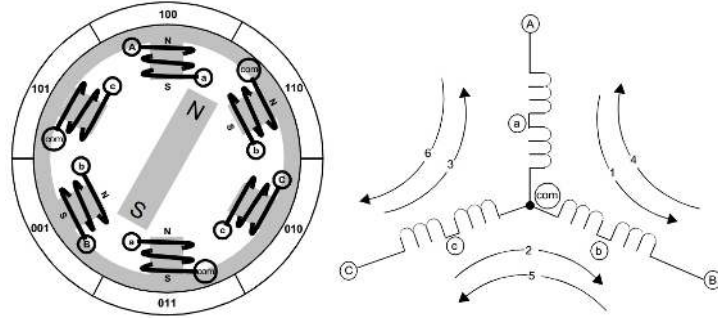


Figure 3.14: Simplified brushless motor diagram [26].

The rotor can be made to rotate clockwise 60 degrees from the A to B alignment by changing the current path to flow from terminal C to B, noted as path 2 on the schematic. The suggested magnetic alignment is used only for illustration purposes because it is easy to visualize. In practice, maximum torque is obtained when the permanent magnet rotor is 90 degrees away from alignment with the stator magnetic field.

To simplify, we are going to start from a simplified expression of a DC motor, since our brushless motor works with DC current. In this model, we are not going to take in account the temperature effect on the winding which affects directly its performance, as such we will assume a constant temperature ( $\bar{T}$ ) on the windings.

Internal voltage  $v_m$  is assumed to be proportional to the rotation rate  $n$  according to the speed constant  $K_v$  of the motor. Applying basic equations of circuit theory, as the energy conservation, we obtain the motor parameters above in function of the current  $i$  and the motor terminal voltage  $v$ . The presented expressions are function of the motor constants,  $R$ ,  $i_0$  and  $K_v$ , internal resistance, no load current and the speed constant, respectively, which are obtained by bench tests or given by the motor manufacturer. As a reminder,  $K_v$  is usually given in RPM/Volt in motor specifications, however here it is taken as rad/s/Volt:

$$n = (v - iR)K_v, \quad (3.22)$$

$$Q_m = \frac{(i - i_0)}{2\pi K_v}, \quad (3.23)$$

The shaft power is then:

$$P_{shaft} = 2\pi n Q_m = (i - i_0)(v - iR), \quad (3.24)$$

Defining the electric power:

$$P_{elec} = vi, \quad (3.25)$$

Results for the motor efficiency:



$$\eta_m = \frac{P_{shaft}}{P_{elec}} = \left(1 - \frac{i_0}{i}\right) \left(1 - \frac{iR}{v}\right), \quad (3.26)$$

Since the main goal of this thesis it is to connect an electric motor to a propeller, equation (3.22) should be written in function of the current  $i$ :

$$i = \left(v - \frac{n}{K_v}\right) \frac{1}{R}, \quad (3.27)$$

In this way, substituting the right side for the equations (3.23), (3.24) and (3.26), we obtain the three most important parameters of the motor in function  $n$  and the motor voltage  $v$  are obtained:

$$Q_m = \left[\left(v - \frac{n}{K_v}\right) \frac{1}{R} - i_0\right] \frac{1}{2\pi K_v}, \quad (3.28)$$

$$P_{shaft} = \left[\left(v - \frac{n}{K_v}\right) \frac{1}{R} - i_0\right] \frac{n}{K_v}, \quad (3.29)$$

$$\eta_m = \left[1 - \frac{i_0 R}{v - \frac{n}{K_v}}\right] \frac{n}{v K_v}, \quad (3.30)$$

### 3.3.3 Electronic Speed Controller (ESC)

Regardless of the type used, an ESC interprets control information not as mechanical motion as would be the case of a servo, but rather in a way that varies the switching rate of a network of field effect transistors, or FETs. The rapid switching of the transistors is what causes the motor itself to emit its characteristic high-pitched whine, especially noticeable at lower speeds. It also allows much smoother and more precise variation of motor speed in a far more efficient manner than the mechanical type with a resistive coil and moving arm once in common use.

Most modern ESCs incorporate a Battery Eliminator Circuit (or BEC) to regulate voltage for the receiver, removing the need for receiver batteries. BECs are usually either linear or switched mode voltage regulators. DC ESCs in the broader sense are PWM (Pulse-Width Modulation) controllers for electric motors. The ESC generally accepts a nominal 50 Hz PWM servo input signal whose pulse width varies from 1 ms to 2 ms. As represented in Figure 3.15, when supplied with a 1 ms width pulse at 50 Hz, the ESC responds by turning off the DC motor attached to its output. A 1.5 ms pulse-width input signal drives the motor at approximately half-speed. When presented with 2.0 ms input signal, the motor runs at full speed as illustrated in Fig. 3.15 a).

The speed of the motor has nothing to do with voltage or amps, but instead the timing of the current fed into it. By increasing and decreasing the wave length (frequency) of the trapezoidal wave on the 3 phases, the ESC causes the motor to spin faster and slower. The ESC switches the polarity of the phases of the motor to create the waves. This means that the voltage through any given winding flows 'alternately' one direction then the other. This creates a push-pull effect in the magnetic field of each winding, making the motor more powerful for its size and weight. The motor and the load that is placed

on it, is what determines the amp draw from the ESC and the battery.

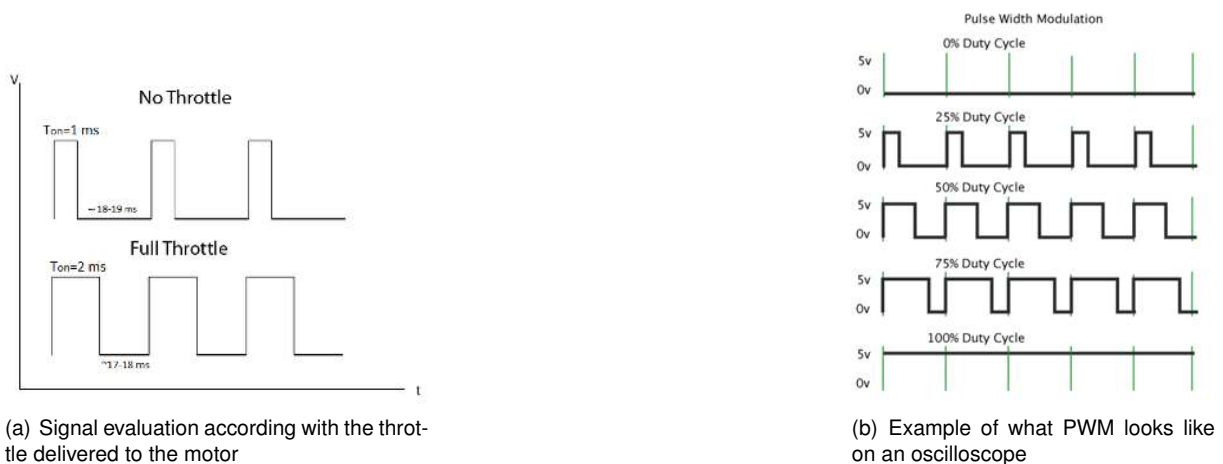


Figure 3.15: PWM representations.

Selecting a speed control is a matter of determining the conditions under which it must operate, and then choosing one with specifications that fit those conditions. The parameters to consider are number of cells, expected current draw, space available, weight limits, need for a BEC, need for a brake.

A brake is a necessity if flying a glider and you the propeller to fold when the motor stops. It is actually better for a propeller to stop spinning than to free wheel, since it creates less drag that way.

### 3.3.4 Power Supply/Battery

Many small UAVs are electrically powered. Furthermore, for these electrically powered vehicles, the power storage system, in most cases a battery, represents the largest component by weight in the vehicle. Improvements in power storage represent the largest "target of opportunity" to decrease the weight of the vehicle and/or improve the performance. While in general it can be said that chemistry improvements provide weight savings, other factors may influence whether there is a net gain. For example, in the case of recent developments in rechargeable Lithium based batteries, the radio-controlled model aircraft demands for higher current draw batteries has caused a decrease in the total storage capacity for a given weight. Such tradeoffs are useful for applications such as 3-D aerobatic aircraft where run time is limited and thrust-to-weight is a primary motivating factor. However, for longer endurance UAVs, the surge current requirement is likely to be far less so there would be a net penalty involved in using the higher current draw rated battery. As battery chemistry and manufacturing technologies improve, they will need to be focused on the small UAV application needs in order to provide an overall improvement to the vehicle system. Testing will also be required to ensure that these new battery types are capable of withstanding the duty cycles intended for UAV application[27].

From what we can see and understand from the Figure 3.16, since we would like a battery that can be lighter but also can deliver a good amount of power to the motor, the natural choice for our UAV will be a Lithium Polymer (LiPo) battery due to its large energy density.

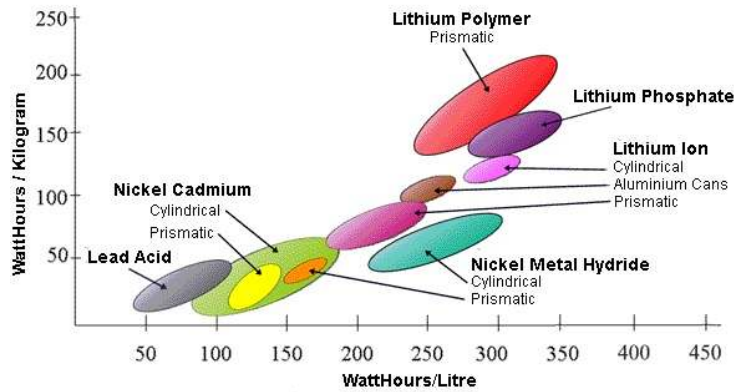


Figure 3.16: Comparison of energy densities for various chemistries [27]

### Lithium Polymer (LiPo) Batteries

Lithium polymer (also known as Li-Poly or Lipo) batteries are the most common type of battery used in present-day UAVs. They are commonly used as the main power source for the UAV's propulsion system, and/or as a secondary power source for electronic subsystems. Their high energy density and discharge rates make them ideal for use in flying vehicles. However, they can be easily damaged or even pose fire hazards if not used or maintained properly.

The main parameters used when selecting a battery are its number of cells (sometimes referred to as "S", for example 3S is a 3-cell battery), its capacity (expressed in milliamp-hours or mAh), and the batteries discharge rating (called the C rating)(see Figure 3.17). The number of cells determines the voltage of the battery pack. Since each cell has a nominal voltage of 3.7 Volts and a maximum voltage of 4.2 Volts, a 3 cell battery pack would have a maximum Voltage of 12.6 volts. Higher voltages will allow the motor to deliver more power, but care must be taken not to exceed the motor current rating, or electronics voltage ratings when selecting the voltage of the battery.

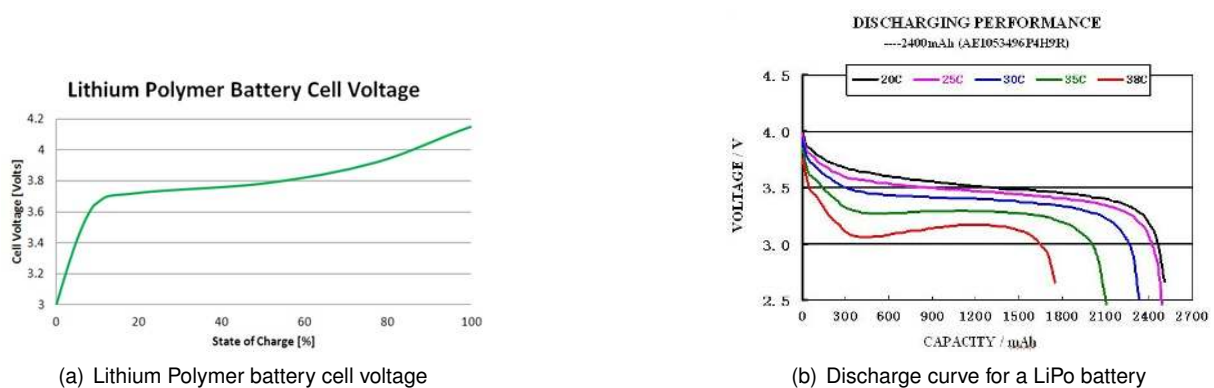


Figure 3.17: Characteristic curves for a LiPo battery

The battery capacity specifies how much energy the battery can store. For example, a 1000 mAh (milliamp-hour) battery can deliver 1000 milliamps for one hour. Similarly, the run time in hours for any other current draw can be calculated by dividing the capacity in milliamp-hours by the current draw in milliamps. As see in Fig. 3.17, with the discharge curve the aproximate run time of a LiPo battery can be

predicted. Using 1000 mAh battery as an example; if it has a 20C discharge rating, that would mean it could sustain a maximum load up to 20,000 milliamps (or 20 amps). From a purely theoretical time stand point, this equals 333 mAh of draw per minute so the 1000 mAh pack would be completely exhausted in about 3 minutes if subjected to the maximum rated 20C discharge rate the entire time.

The C rating specifies the maximum current the battery can safely provide. Some batteries specify a 'continuous' C rating and a higher 'burst' C rating. While the continuous C rating specifies the maximum current at normal operation, the burst rating gives a higher value that can be safely achieved for short periods of time (a few seconds). Another important factor in battery selection is the weight of the battery.

The battery capacity is the main driver of the weight, adding roughly 1 gram for each 10 mAh of capacity.

## Chapter 4

# Test Rig Requirements

Before the test rig can be designed, it is necessary to establish what its testing limits will be. Our test stand will measure several data during each test, so it becomes necessary first to establish what will be the output/input data. As shown in Figure 4.1, the brushless motor, the wind tunnel, the ESC (Electronic Speed Controller) and the propeller tested will be associated to several measured parameters. Each of these parameters will be briefly described during this chapter including its maximum possible value.

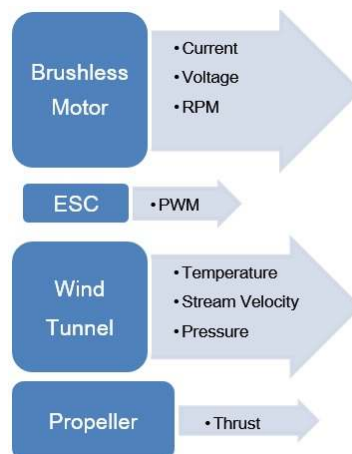


Figure 4.1: Output Data taken from the system.

The three main requirements that conditioned the maximum values measured in the test rig were:

- Propeller Diameter: 9" Minimum, 27" Maximum.
- Diameter of the motor: 15 millimetres minimum, 65 millimetres maximum
- Wind tunnel speed: 50m/s Maximum

Defined the three main constraints of our test stand, it is necessary to study each parameter measured in the test rig, in order to understand its maximum value. This procedure is very important since it will define the design structure of the test rig.

# 4.1 Propeller

According to the requirements, it was decided to design this test stand with a capability to test propellers up to 27” of diameter. This decision will be central in the study of our test stand requirements. According to the available propellers, it was decided that the minimum diameter of propellers would be 9”.

Choose the range of diameters that the test rig can test, it was necessary to describe what would be the range of loads, generated by the propeller, which the structure would then be subjected. As it was described in figure 4.1, the propeller induces thrust. Each propeller will generate a different quantity of thrust. It was studied what were the maximum possible values for each of the propellers tested. Due to the high number of present propellers, it is only shown three sizes of propellers. The smaller propeller, a medium 16” diameter propeller and the biggest propeller.

## Thrust

According to the propeller manufacturer, APC - Advance Precision Composites[28], for a propeller of a given size, the main parameters at a certain RPM were found. As in the previous chapter, knowing the coefficient of thrust, it will be able to compute its value. As it was described before, it will be presented only three propellers to study the range of values of thrust that the structure will be subjected. The smaller will be a 9”x6”E, the mid range propeller will be 16”x10”E and the biggest propeller will be a 27”x13”E. Note that the notation for referring the propeller is DiameterxPitch will be necessary to estimate the maximum rotation that the motor can deliver to the propeller. To know this, without knowing the exact motor that will be used during the tests, it was made a research for the brushless motor manufacturer, Hyperion[29] and AXI[30]. Each of these manufacturers have available on their website tests made with different type of propellers. Selecting the three size of propellers described before, it is possible to find the maximum possible rotation of this propeller. It is also possible to estimate the maximum rotation of each motor knowing their constants  $K_v$ , R, maximum current and maximum power. Knowing the maximum current limit of Li-Po cells available to each motor, it becomes possible to estimate the maximum RPM for each motor. Naturally, this RPM obtained with equation (3.22), is the RPM without any propeller attached. When the propeller is attached, the maximum possible RPM of this motor becomes smaller. After this study, for the three sizes of propellers it was possible to estimate the maximum RPM for each propeller (see Table 4.1).

Propeller	Max RPM
9x6E	12000
16x10E	9000
27x13E	6000

Table 4.1: Maximum possible values of RPM for each propeller

In Figure 4.2 it is shown the thrust coefficient as a function of advance ratio  $J$  and the ratio of pitch to diameter,  $p/D$ , for a typical model propeller profile. All curves have the same shape and  $C_T$  range from about 0.0 to about .095. Maximum thrust is achieved at the lowest advance ratio, decreasing essentially linearly to 0 as  $J$  increases. The values are not reliable in the region at the top where the curves goes

to a null value of  $J$ . In this region a portion of the blades become stalled. The greater the pitch ratio the larger the range of  $J$  affected by stalling. All these curves go to zero as  $J$  increases, meaning that the thrust also goes to zero. The underlying reason is that the angle of attack,  $\alpha$ , becomes zero so the blade does not provide lift or thrust. Using the chart in Fig. 4.2, the equations for  $J$  and the  $C_T$ , the maximum thrust can be estimated assuming null  $J$  (static condition).

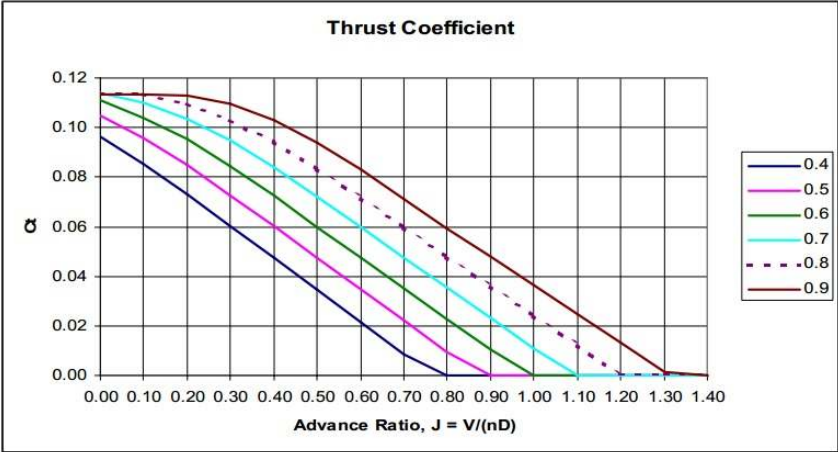


Figure 4.2: Thrust coefficient versus advance ratio for different  $p/D$  [31].

The thrust can be computed with the above correlation:

$$T = C_T \rho N^2 D^4 \tag{4.1}$$

Parameters	Propeller 9x6E	Propeller 16x10E	Propeller 27x13E
$\frac{p}{D}$	0.666	0.625	0.48
$C_T$	0.115	0.110	0.099
$RPM_{max}$	12000	9000	6000
Thrust [Kgf]	1.57	8.44	27.37

Table 4.2: Maximum and minimum values of thrust presented in the structure

According to table 4.2, the maximum value of thrust will be around 30 Kgf. This corresponds to propellers with large diameters. For the smallest propeller, the value of thrust will be around 2 Kgf. To refer that the computation of Thrust using this method has some error. Graphical interpretation can generate errors, but also the performance data of the propeller manufacturer can have experimental error associated.

As the graph presented in fig. 4.3, according to the range of propellers that the test rig is going to be designed, it is clear that three groups of propellers will need different measuring sensors. As it was demonstrated before, the test rig will be able to test values of thrust up to 30kg.f. With the graphic presented in fig. 4.3, one can predict that the test rig will need three measuring systems with three different ranges to achieve a better measurement quality.

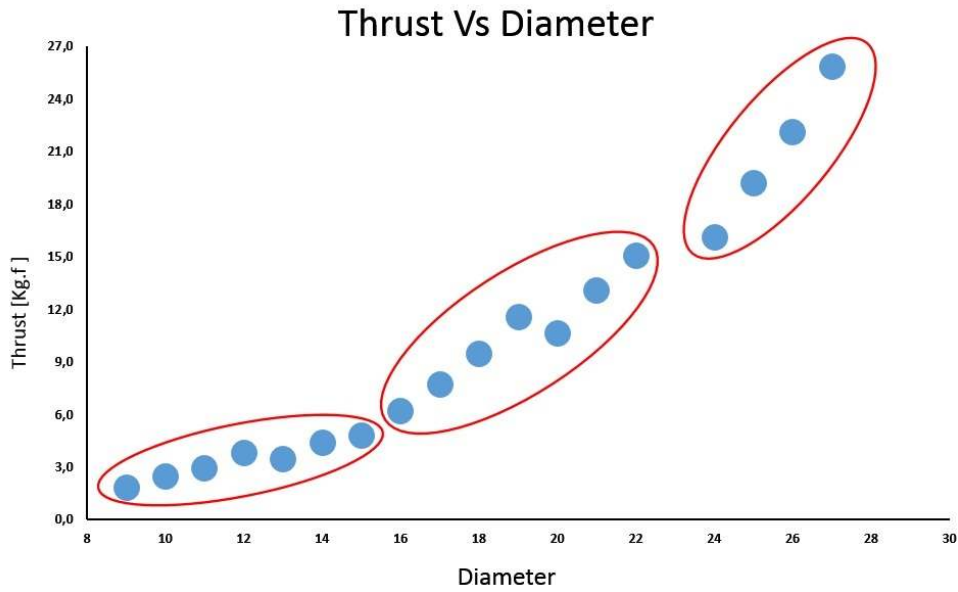


Figure 4.3: Thrust versus diameter of propeller

### Propulsive Power

To estimate the absorbed mechanical power for the propeller and the power consumed by the power supply, it is necessary to compute the power generated by the propeller. This depends on the propeller efficiency, which is constant for a certain RPM and velocity. The power coefficient,  $C_P$ , is a function of advance ratio  $J$  and the pitch to diameter ratio  $p/D$  as shown in fig. 4.4. In this case, the power increases as the fifth power of diameter and the cubic power of the revolution rate. The maximum value of the coefficient of power will not be obtained for a null advance ratio. Also to refer that the graphs are not so reliable for low values of advance ratio. This can be demonstrated through the values of  $C_P$  presented in the performance data sheet. This problem was described by W. B. Garner[31]. Using the chart presented in Figure 4.4, the values for the three propellers are obtained. Note that in this case the values of  $C_P$  are obtained for a specific value of advance ratio and not for a null value of  $J$  as seen with thrust.



Figure 4.4: Power coefficient versus advance ratio,  $p/D$  a parameter [31]



Rewriting, the propulsive power can be computed as:

$$P_{prop} = C_P \rho N^3 D^5, \quad (4.2)$$

This propulsive power is computed counting already the propeller efficiency. Is also interesting to compute the propeller efficiency for each propeller size.

Parameters	Propeller 9x6E	Propeller 16x10E	Propeller 27x13E
$\frac{p}{D}$	0.666	0.625	0.48
$C_P$	0.047	0.042	0.032
$J$	0.4	0.4	0.3
$RPM_{max}$	12000	9000	6000
$P_{prop}$ [KW]	0.39	1.93	5.95

Table 4.3: Propulsive power for three ranges of propellers

Of interest is the power efficiency defined as the ratio of thrust power to motor power as defined in graphic 4.3. The higher this ratio, the more efficient the propeller. Note that thrust power is defined as the product of the thrust,  $T$ , and the forward speed,  $V$ . This is the conventional definition in which useful work is done only when there is actual motion.

$$\eta = \frac{C_T \times J}{C_P} = \frac{T \times V}{P_{Mechanic}} \quad (4.3)$$

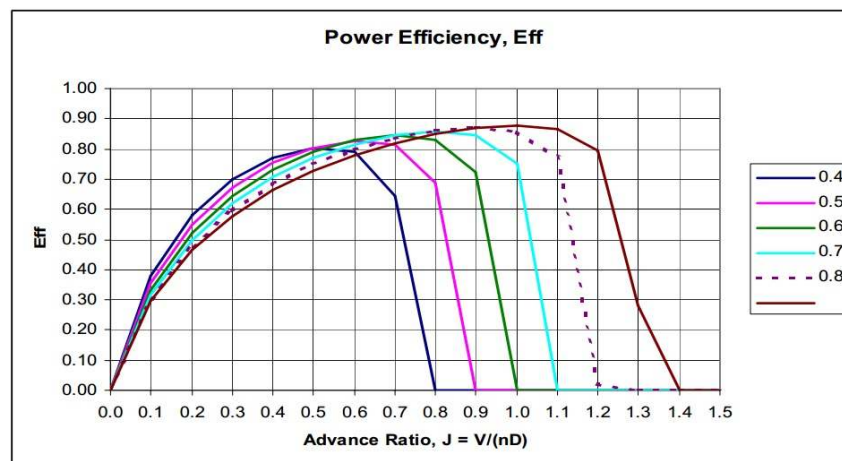


Figure 4.5: Propeller efficiency coefficient[31].

The efficiency is zero at  $J = 0$  when the propeller is not advancing. The peak efficiency is a function of the pitch to diameter ratio, being the least for the lowest ratio and the greatest for the highest ratio. For the examples of the three propellers, using figure 4.5 for  $J$  and  $p/D$  for each propeller, it is obtained the data in table 4.4.

Parameters	Propeller 9x6E	Propeller 16x10E	Propeller 27x13E
$\frac{p}{D}$	0.666	0.625	0.48
$J$	0.4	0.4	0.3
<i>Efficiency</i>	0.72	0.73	0.67

Table 4.4: Propeller efficiency for each propeller for a certain advance ratio

## 4.2 Brushless Motor

As it was described in the first section of this chapter, the motors to be installed in the test rig would have to be capable of testing propellers up to 27". Naturally, it would be almost impossible to use only one type of motor for testing every size of propellers proposed. With this in mind, it was decided to also select three different brushless motors for each group of propellers (small, mid-range and large). It was done a study through the suitable brushless motors manufacturers and it was decided to provide the test rig with AXI motors. This choice was based mainly to the large range of motors available of this manufacturer but also due to their high efficiency.

For the three ranges needed, it will be presented some characteristics that the motors must have to generate a correct amount of electrical power to the system. For the three group of propellers, according to the propeller manufacturer, it is known the recommended number of Li-Po cells that the system must have. It was presented in the chapter 3 how much LiPo cells can deliver to an electrical motor. Knowing the range of LiPo cells that the three groups of propellers would need and also knowing the maximum accepted current for each kind of motor, it is possible to present the minimum electrical power that the motors must have in table 4.5.

Parameters	Propeller 9x6E	Propeller 16x10E	Propeller 27x13E
Desirable LiPo Cells	3S	4S-7S	$\geq 8S$
Maximum efficiency current	4-8A ( $\geq 72\%$ )	18 - 40 A ( $\geq 84\%$ )	25 - 63 A ( $\geq 85\%$ )
Minimum Electrical Power	51 W	303 W	840 W
Diameter	27.7 mm	49.8 mm	63 mm

Table 4.5: Minimum electrical power for the testing motors [30].

In table 4.5, it is possible to see the expected values for the electrical power necessary to perform the tests. The values presented in the table are only an approximation of the values for the electrical power the motor is going to demand. To perform this approximation, it is possible to fix one of the constants in the electrical power that is the voltage. Knowing generically what the number of LiPo cells are needed for each group of propellers, it is possible to know the voltage needed for the motor. Regarding the current, it will be different for every RPM of the motor. Logically, for a higher/lower value of RPM, a higher/lower value of current will be demanded by the motor. It is not possible to know the exact value of current for each RPM of the motor, since there are too many parameters that depends on this value - type of motor, his efficiency, voltage, etc. In this case, it was use the lowest value of current in the range where the motor works with maximum efficiency. Also to refer that the range of values of current were taken from data sheets from motors of the manufacturer AXI [30]. The choice of these motors was made according to the size of propeller to use. Theoretically, this study can be accepted for choosing a suitable motor,

however practically it is likely that the motor will demand a higher value of current since the tests will be performed for a wide range of RPM.

### 4.3 Power Supply

The electrical source that is going to be used in the test rig will vary according to the type of propeller that is going to be tested. Smaller propellers will demand a lower value of voltage and current to the electrical source and larger propellers will, demand higher values of voltage and current. With this, it is also interesting to know what the range of propellers that will demand a usage of LiPo batteries or a stabilized power supply is. It is also possible to perform tests that demand a higher value of current and voltage with battery, however the LiPo battery will run out of energy too quickly, preventing the test rig to perform a test for a suitable period of time. Hereupon, it was necessary to first know what was the normal current capacity for a LiPo cell. There are several models of LiPo batteries, each with different capacity and discharge rate.

For presenting the estimated duration of a LiPo cell battery, due to the wide range of batteries, it has to be assumed a battery with:

- Energy capacity of 5Ah.
- Discharge rate of 40C.
- During the test it is providing the nominal tension.

It was also assumed that the power needed for testing is the propulsive power generated by the propeller at their maximum RPM, and that, since the type of motor that is going to be used in the testing is unknown, their electrical efficiency is assumed to be 80%.

With these values, it is only necessary to estimate a fixed value of current for a certain RPM to determine how long can a test be performed with this form of electrical supply. For this, for each size of propeller it was taken from the Performance Data of the brushless motor Hyperion and AXI[30] typical values of current for a certain RPM with APC propellers. These tests performed by the motors manufacturers can be found in the appendix A in the table A.1 in this appendix. Also in this appendix A on the table A.1 can be found the table with all the parameters used to plot the graph in figure 4.6 and 4.7.

It was first studied the range of consumed electrical power for each propeller size. A stabilized power supply will be able to delivery a lower electrical power to the motor, however a battery will supply an higher value of electrical power. In figure 4.6 it is plotted the graph of the electrical consumed power for each propeller. The data to plot this graph was obtained for the assumptions described. According to the available power supplies, as it is shown that it is possible to use stabilized power supplies to perform the tests for propeller up to 13". Power supplies with more than 2KW will be too expensive and it will be necessary the use of batteries for propellers larger than 13".

It is also interesting, knowing that for propellers with a certain size, it will be necessary to use LiPo cells battery, how long does a battery will last until it runs out of energy. As the graph presented in figure

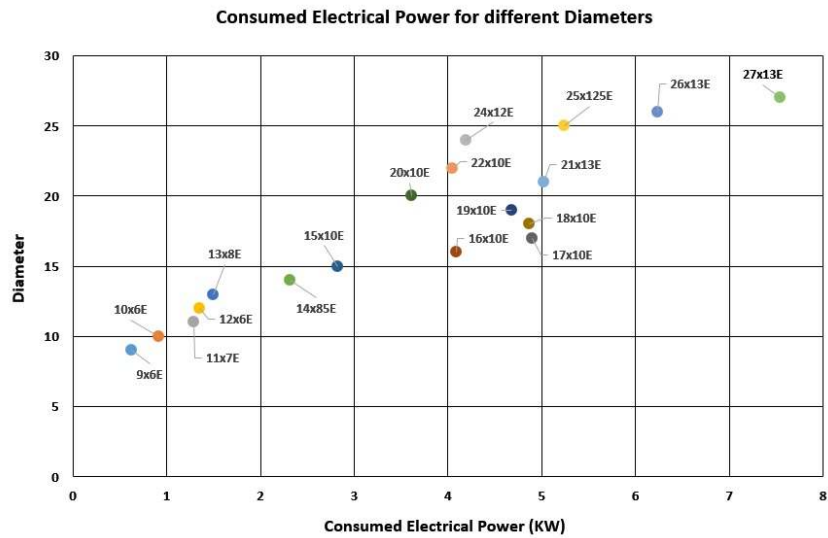


Figure 4.6: Estimated required electrical power for different propellers

4.7 shows, for lower propellers diameter (up to 14”), it is possible to use LiPo cells since this one will be able to deliver a good amount of current to the system for a suitable time. Also to know that this study was based on the maximum current. Experimentally, the system will not be running at the maximum RPM during all time. For propellers larger than 14”, it is shown that at the maximum RPM, the battery will run out in less than 3 minutes. One solution would be also to use batteries with an higher energy capacity or increase the number of LiPo cells of the battery.

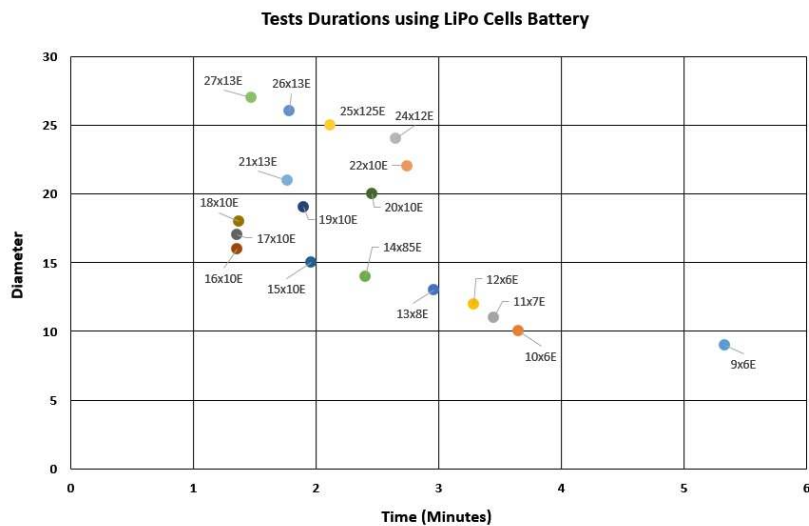


Figure 4.7: Estimated battery duration for different propellers

Also another important fact to refer is the maximum current reached during the test, as it is possible to see in the appendix A in the table A.1, reached more than 200 A, which is the maximum current that the battery can deliver to the system. This might lead to use batteries with an higher discharge rate, to achieve a higher current delivered to the system. It is also necessary to install the system with connection cables capable of receiving such amount of current.

## 4.4 Electronic Speed Controller

The electronic speed controller present in the test rig will have to be sized for the motors and propellers to be tested. This device, will allow to vary the RPM of the motor with the PWM signal as described in section 3.3.3. The two parameters that will determine the choice of the ESC are the maximum current allowed in the motor and also the number of LiPo cells allowed on the ESC. Also in this case it will not be possible to have a single ESC to perform all the tests. It was studied the typical maximum current for the three types of motors used with the three propellers in study before (9",16" and 27").

Parameters	Propeller 9x6E	Propeller 16x10E	Propeller 27x13E
LiPo Cells	3S	4S-7S	≥ 8S
Maximum Continue Current - Motor	10A	60A	75A
Maximum Desirable Current - ESC	≥ 20A	≥ 75A	≥ 90A

Table 4.6: Required maximum current of the ESC[30]

As it is possible to see in table 4.6, the test rig will need at least 2 different ESC for controlling the motor to be installed on it. This need relates to the fact that even the maximum current of the motor is fixed, when reaching this current, the motor always suffers peaks of current, demanding always more current than the maximum current allowed for the motor and ESC. For this, it is always necessary to have an ESC with a maximum allowed current higher than the maximum current of the motor to prevent cause any damage on the motor.

## 4.5 Wind Tunnel

### Physical Limitations

Because the test rig is going to be mounted inside the aero-acoustic wind tunnel at IST (see Figure 4.8), which is an anechoic chamber, it will only be available a limited space for fixing the structure to the ground. This will only be possible thanks to the grids that allow the users to walk inside the chamber (see figure 4.9 b)). All the interior of the chamber was measured. With this, it would allow to define how high the structure could be and how it would fit inside the chamber.



Figure 4.8: Aero-acoustic wind tunnel at IST

To achieve the requirement of the test rig be capable of testing propellers up to 27", it was necessary to limit the total height of the structure. Limiting the height of the structure was a step that was defined mainly for the diameter of the wind tunnel nozzle. To achieve always the best measurement possible, it was necessary that the centre of the propeller coincides always with the centre of the wind tunnel nozzle. With this, it is possible to guarantee that the uniform flow coming from the wind tunnel nozzle is always covering the entire propeller. With this, it was possible to define the maximum height of the structure, around 1.3 meters. To add this value, still missing the height to the ground.

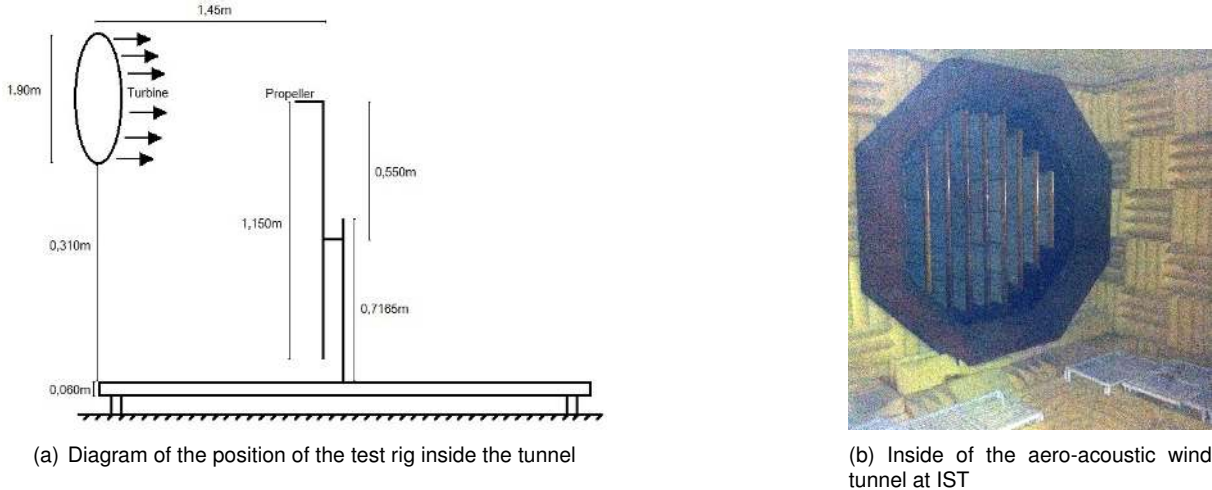


Figure 4.9: Outside view of the test chamber of the aero-acoustic wind tunnel at IST

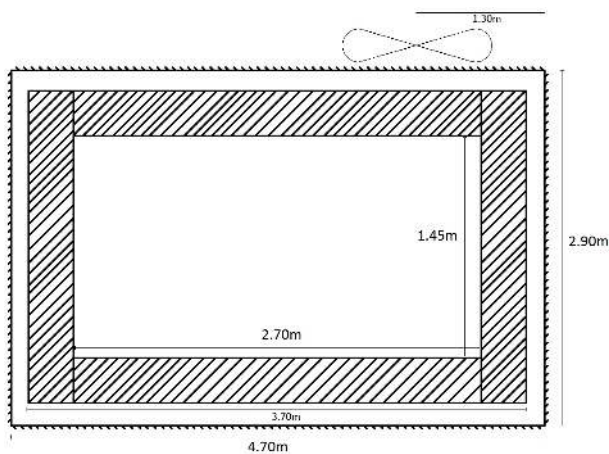
In the figure 4.9 a), it is shown the side view of the tunnel with a draft of the structure already centred vertically with the centre of the wind tunnel nozzle. Also it is described in this figure the distance of the structure from the wind tunnel nozzle.

The support of the structure has to be centred according to the grid present inside the wind tunnel. As figure 4.10 a) shows, the structure have to be distanced around 1.45 meters from the wind tunnel nozzle. It is important that the structure is centred according to the wind tunnel nozzle since if the structure is too far away from the nozzle, it can generate distorted results.

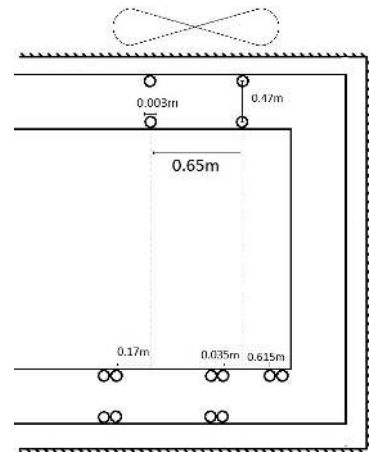
The supports of the structure have also to conform the limits of the wind tunnel. As it is described in figure 4.10 and also represented before, the floor of the wind tunnel is not accessible due to the interior having been converted into an anechoic chamber. With this, it will only be possible to install the structure on the existing supports of the grids. This will limit the number of supports of the structure and also the maximum width of the structure. According to figure 4.10 b), it assumed that the structure could only have a maximum of 0.68 meters in width. Also the non-alignment of the supports of the grids of each side will force to install a secondary support system.

**Temperature**

The temperature at which the tests will be performed will remain almost constant. Since the chamber is well insulated, during the static tests it will be assumed a constant temperature of 20°C (ambient temperature). During the dynamic tests, it will be assumed to have a range of temperatures since the



(a) Inside top view of the aero-acoustic wind tunnel



(b) Diagram of the position of the test rig inside the tunnel

Figure 4.10: Internal measures of the wind tunnel

environment will not be static. It is expected to have a temperature measuring equipment that would be capable of measuring temperatures from 0 °C up to 50°C. Since the density of the air is changing with the temperature, it is also expected that these two measures vary along the dynamic tests.

### Stream Velocity

The stream velocity of the wind tunnel is also a parameter that will limit the systems present in the test rig. The aero-acoustic wind tunnel is capable of reaching a maximum speed of 50 m/s. With this, it is necessary to provide to the test rig systems capable of measuring pressures differences that could measure a maximum of 50 m/s of stream velocity. According to the type of tests, it was decided to install a stream velocity measurement system of the type of Pitot Tube, capable of measuring the total and static pressure, thus allowing the estimation of the speed from the dynamic pressure according to the Bernoulli equation[23]:

$$V = \sqrt{\frac{2}{\rho}(p_{total} - p_{static})} \quad (4.4)$$





# Chapter 5

## Test Rig Design

After defining the main requirements of the test rig in chapter 4, it is now possible to design and validate the proposed structure. As it is possible to see in figure 5.1, it was chosen to verify the structure only after the design of the complete structure due to the small loads that this structure will be subjected.

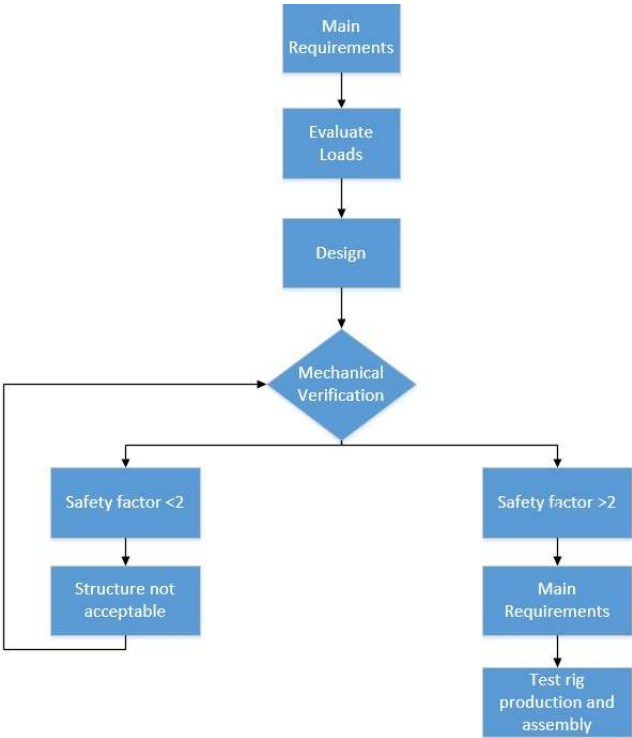


Figure 5.1: Design flowchart for the structure

### 5.1 Measuring Method

As it was described in the previous chapter, the test rig will need at least three measuring systems with different ranges. However, the first step that it is necessary to do is to choose the method of measuring the loads that the test rig will be subjected, namely the motor thrust. In the beginning several systems

that could be installed on the test rig were studied. As it is known, the motor will cause a load on the main beam of the structure. It is possible to measure this with different ways. In figure 5.2, there are several ways to measure the thrust generated by the propeller.

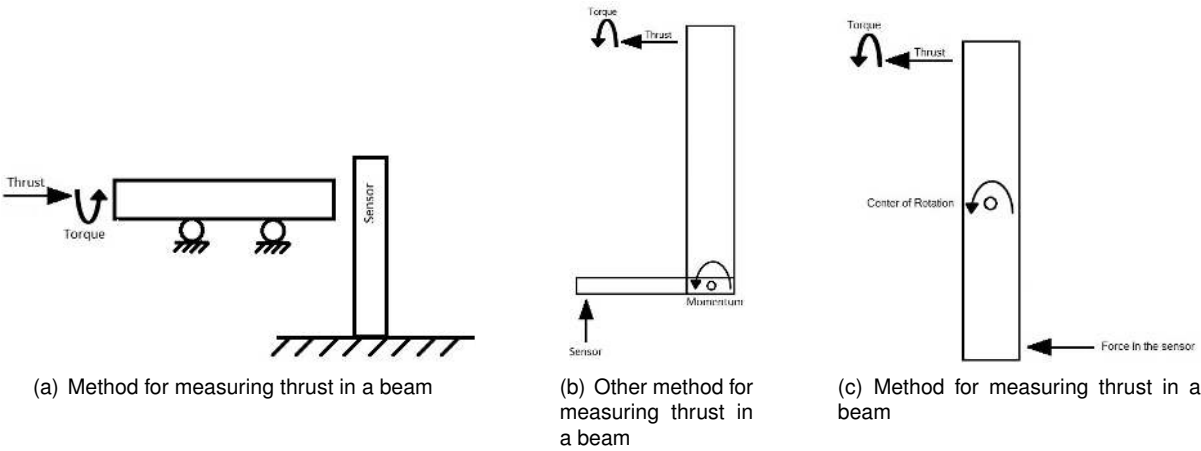


Figure 5.2: Free body diagram for several different ways to measure thrust in a beam

It was first studied a direct measure, right behind the motor (see figure 5.2 a)). This will generate simple measure however, to ensure a good measuring quality, it will be necessary to change the load cell to every propeller since an optimal measure is the one that fills most of the range of the load cell. In the market, there are already a few systems that allow to measure propulsive systems like the one described in this paragraph. In figure 5.3, it is possible to see the model of the manufacturer Turnigy [32], that allows to measure small thrust loads. It is also necessary to refer that the type of load cell to be installed has to hold bending loads and not compression/traction loads.



Figure 5.3: Turnigy thrust stand[32]

Another solution was to take advantage of the momentum generated by the beam (see figure 5.2 b)). This is a good solution since the load measured by the thrust system can be adjusted to the real load generated by the propeller thanks to the distance from the centre of rotation until the place where the thrust is applied. One simple example of this system is shown in figure 5.4, having a simple scale as the load cell for measuring the thrust generated by the propeller. The type of cell for this load would be a load cell that would only have to hold traction/compression loads. However, this system would not fulfill with the requirement of height that the test rig has to have to be centred with the wind tunnel. Also,

for space matters, this is not a suitable solution since it would require to fix the sensor or the measuring system to the ground which it could be more complicated.

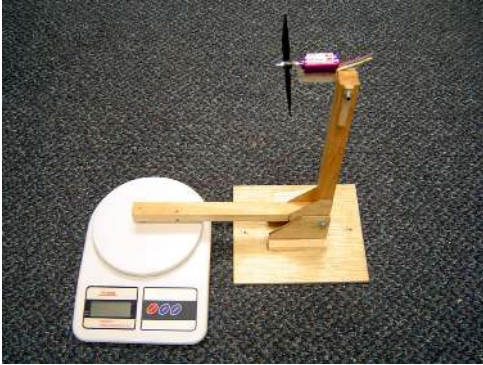


Figure 5.4: Example of a simple thrust measurement

After these two solutions, the decision was to adopt a system similar to the one sketched in figure 5.2 c) but with a variable position of the sensor. This will allow the test rig to measure, with the same load cell, several values of thrust and even adjust the position of the sensor in order to fill most of the range of the load cell. The load cell would only have to hold traction/compression loads and could be installed on the back of the main beam.

## 5.2 Studied Solutions

After choosing the measuring method for the load that will be present in the structure, it is necessary to study different ways to support the structure. During this thesis, several drafts of possible solutions were made and each of them were studied until reaching to the final solution.

The first assumption that was made was to install all the system in one main beam. This beam would have a pin, placed at mid height of the beam, that would have be the centre of rotation. This pin would be the part responsible for holding all the weight of the beam and its structure. Next, it was studied several solutions to couple this pin.

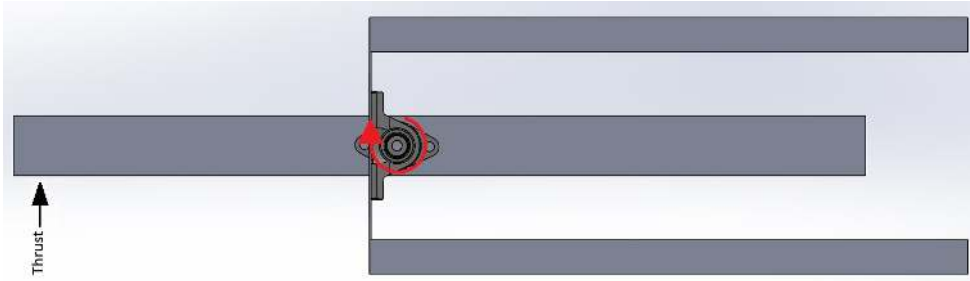


Figure 5.5: Sketch of how the option with the table works.

The first solution that was approached was having a table fixed to the ground, or to a support foundation. The main feature for this solution was the use of four bearing housing units, that would be responsible for holding the structure and handle the momentum to the main beam. The housing unit

would be fixed to the table, which would allow the pin to rotate with the same momentum as the main beam, transmitting in this way the load of the thrust to the load cell that would be installed along the beam. This solution is sketched in figure 5.5.

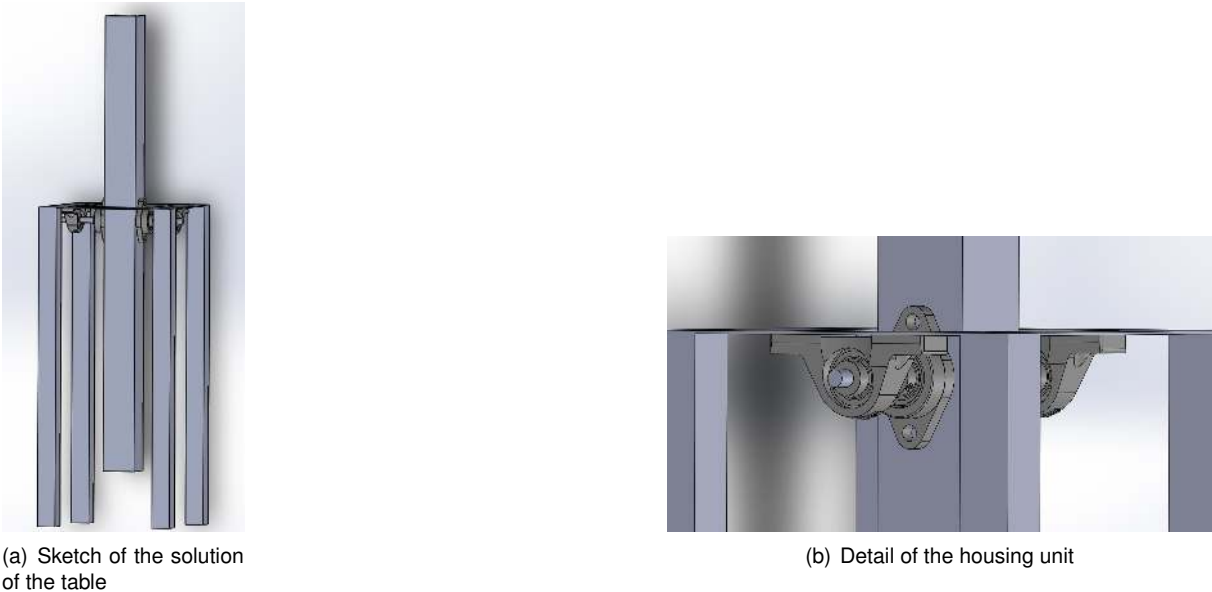


Figure 5.6: First version of the test rig

As it is possible to see in figure 5.6, with the housing bearing unit it would be possible to hold the main beam and allow a free rotation of the beam, having the table fixed to the ground. However, this solution was not practical due to the amount of supports, the not practical assembling but also the presence of the table could generate additional forces in the structure when performing a dynamic test. It was decided that, for the test rig, it would be much more effective and practical to use only two supports, which would be attached directly to the support foundation that would be built.

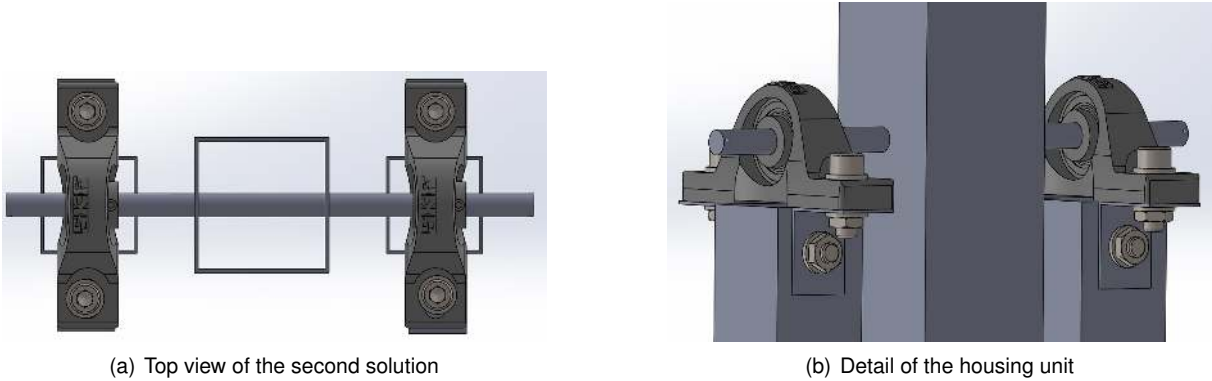


Figure 5.7: Second version of the test rig.

After reviewing the structure, the supports were reduced to two, and the housing units were rotated so that they can be in the horizontal position. As it is possible to see in figure 5.7, this would improve the assembling of the structure into the wind tunnel, reducing the number of supports by two. However, as it is possible to see in figure 5.7 b), the mounting of the load cell would be a problem since the main beam is aligned with the support beams. Also, with this type of mounting, it would be necessary to have

a beam with a length similar to the housing unit length to stabilize it. The new concept for the proposed structure is presented in the next section and can be seen in figure 5.8.

### 5.3 Proposed Structure Design

After re-designing the second version, it resulted in the structure represented in figure 5.8. The final structure was re-designed in order to assembly correctly the load cell but also the bearing housing unit was rotated to a vertical position due to the advance of the main beam. With this, it was ensured a stable structure.

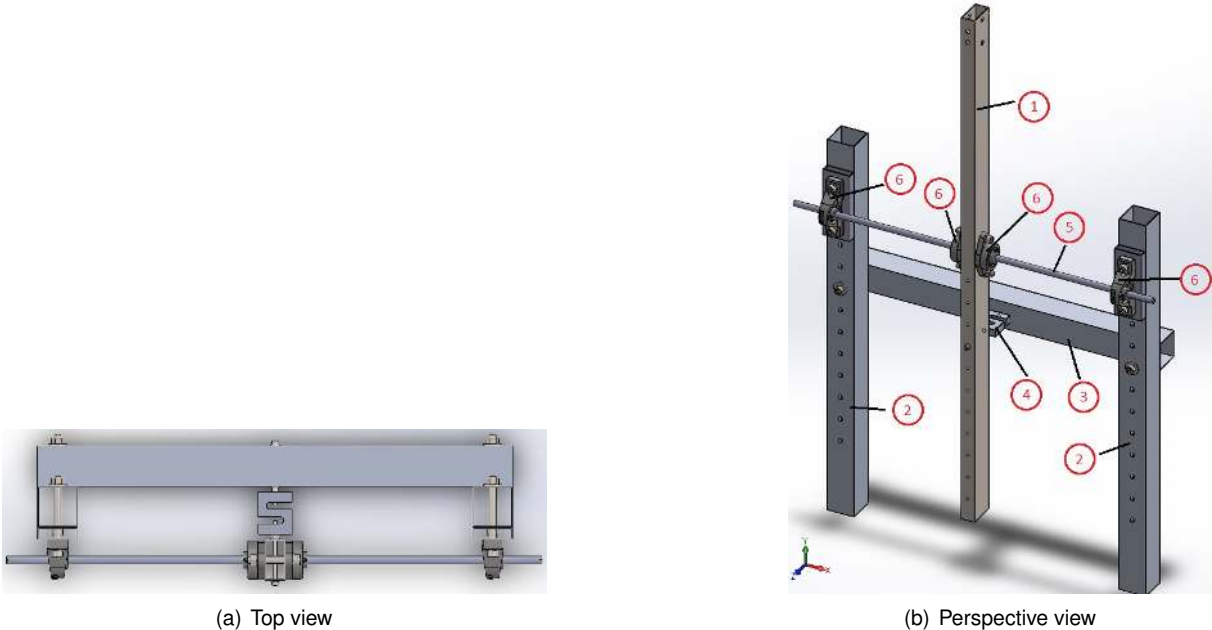


Figure 5.8: Proposed solution for the measuring system of the test rig.

In figure 5.8 b), it is possible to see the several different components that the structure will contain. Table 5.21 briefly describes the components present in the structure.

Component	Name
1	Main beam
2	Support Beam
3	Rear beam
4	Load cell
5	Pin/Rod
6	Bearing Housing Unit

Table 5.1: Description of the components present in the structure

The proposed solution for the structure, will have to comply with the load requirements and physical constraints defined in the previous chapter 4. Thus, with this solution it will be possible to comply with:

- Maximum 27", Minimum 9"
- Flexibility to install and change more than one load measuring system in the test rig.

- Have a system that can guarantee a good quality of measuring with the same load cell.
- Ensure that all the structure can withstand with a maximum load of around 27 Kg of load generated by the propulsive system.
- Assure that the motor axis is coincident with the centre of the wind stream.
- The structure should have a distance of 650 millimetres between the centre of the axis of the support beams.
- The support beams should have the necessary height to accommodate the bearing housing unit.
- All the components present in the structure, when loaded with the maximum load have to present a safety factor of at least 2.
- The maximum displacement of any component should not exceed 5 millimetres.

### 5.3.1 Overall Dimensions and Components

Thus, according the requirements defined in the previous chapter and also in the previous section, it will be possible to define the overall dimensions of the structure sketched in figure 5.9.

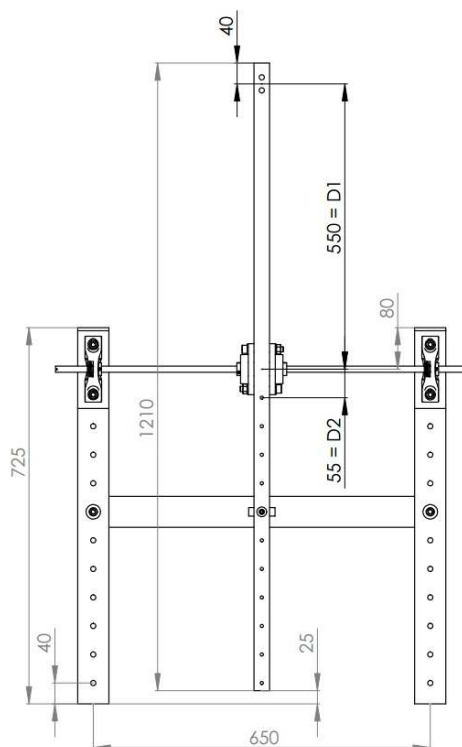


Figure 5.9: General dimensions for the structure

The total height of the main beam, 1210 millimetres, was defined due to the physical requirement of matching the axis of the motor to the centre of the stream of the wind tunnel. Positioning the centre of the motor 40 millimetres from the top of the main beam was related to the distance from this point until the pin. This distance would be 550 millimetres.

Also, as it was said previously, the load cell will have a variable position in the main beam. The value measured in the load cell will depend where the user of the test rig will position the load cell. Each position of  $D_2$  is distanced 55 millimetres from each other. Since the distance from the pin until the lower part of the main beam would be more than 550 millimetres, in this structure will be possible to measure a load lower than the load generated by the motor. In table 5.2 it is possible to see the available relations for  $\frac{D_1}{D_2}$  that this structure will have. Noting the the distance  $D_1$  is the distance from the pin to the axis of the motor and the distance  $D_2$  is the distance from the pin to the axis of the load cell.

Relation $\frac{D_1}{D_2}$
10
5
3.33
2.5
2
1.67
1.43
1.25
1.11
1
0.91

Table 5.2: Relations  $\frac{D_1}{D_2}$  available in the main beam

Also to refer that the holes where the bolts will attach the rear beam to the support beam have to match with the location where the load cell will be positioned in the main beam.

**5.3.2 Main Properties of the components**

Presented the main components of the structure, it becomes necessary to present their material and geometric properties. The material for the components is still unknown since a complete load analysis will be performed in the next section using aluminium and steel. At this point, it is only known the specific geometry of each section.



Figure 5.10: Different profiles used in the structure

In figure 5.10 it is possible to see the different profiles used for the different components. The exact dimensions for this components will be presented after the load analysis performed in the next section. Also in the table 5.3 it is possible to see the mechanical properties for steel and aluminium alloys used for the study.

Material	Yield Stress , $\sigma_{yield}$ [MPa]	Ultimate Stress, $\sigma_u$ [MPa]	Young Modulus [GPa]
Steel AISI 1035HR	270	495	200
Aluminium 5052-H34	210	262	70.3
BOZD	820	-	-

Table 5.3: Mechanical properties of the materials used in study

### 5.3.3 Load Analysis

After defining the main components of the structure, in this section it will be studied the main loads that the main components are subjected and also their safety coefficients present when applied the maximum allowable load expected for the test rig. Each component will be studied independently, using its free body diagram. The loads presented in the structure are generated mainly by the propeller and motor. During this study, the weight of the motor was discarded. This decision was made mainly because the weight of the motor is much smaller compared to the weight of the beam and also compared to the load that the propeller generates.

To compute the stress, the Von Mises Criteria it will be used. With this, it will be possible to compute the stress present in the structure due to moment, shear and torsion force as.

$$\sigma' = \frac{\sigma_{yield}}{n} = \sqrt{\sigma_M^2 + 3(\tau_T^2 + \tau_V^2)} \quad (5.1)$$

A good exercise would be to compute the stress due to bending moment, shear force and torsion given respectively by:

$$\sigma_M = \frac{M \times c}{I}, \quad \tau_V = \frac{V_{eq}}{A}, \quad \tau_T = \frac{T \times r}{J}, \quad (5.2)$$

$M$  represents the maximum moment,  $c$  represents the maximum distance to the neutral axis and  $I$  the inertia moment,  $T$  represents the maximum torque present in the body,  $r$  is the distance between the rotational axis and the farthest point in the section (at the outer surface).

To design the optimal dimensions according to the requirements described at the beginning of this section, it becomes necessary to consider the most critical situation for the structure. As it was said in the previous chapter, for our tests, the most critical load that it will be possible to have would be 27.37 Kg.f. With the measuring system of the test rig, it becomes necessary to first define the maximum load capacity according the available load cells at the market. Thus, it was decided to limit the load cell capacity to 75 Kg.f. With this, analysing the relation  $\frac{75}{27.37} \approx 2.74$ , the maximum load that the test rig would have to subject, would be with the load cell positioned 220 millimetres from the centre of rotation. This case would correspond to a relation  $\frac{D_1}{D_2} = 2.5$ . In table 5.4 it is represented the loads when testing the maximum load on the test rig.

$F_{motor}$	268.5 N
Safety Coefficient	$\geq 2$
$\frac{D_1}{D_2}$	2.5

Table 5.4: Critical load present in the structure



## Component 1 - Main Beam

Starting with the main beam, this will be the component of the structure that will directly support the loads generated by the propeller. As it was said before, in this beam it will be present the thrust load and torque generated by the propeller. In figure 5.11 it is possible to see the free body diagram of the main beam with all the relevant loads represented.

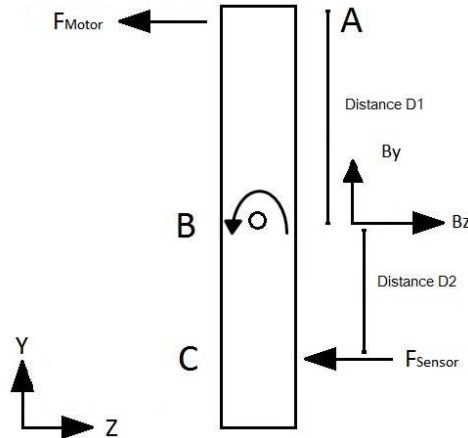


Figure 5.11: Free body diagram of the forces presented in the main beam.

The solution proposed is based on a fixed centre of rotation located in the middle of the beam. In this centre of rotation will be installed a pin that will be responsible for performing the junction to the supports of the structure. This centre of rotation will be constrained, only allowing rotation. Remembering one of the requirements of the test rig, due to the large variety of propellers to test, it will be necessary to use three measuring systems (sensors). When measuring a magnitude, it is important to fill as most as possible the range of the sensor. Since it will be presented a diverse range of thrust and torque values, it is desirable that the sensors installed will always be measuring almost their full capacity. Thus, it was thought to install the sensor in a variable position along the beam. This variable position will allow to measure values of thrust bigger or smaller than the values generated by the propeller, approaching them to the limit of the sensor. The centre of rotation will be situated in the middle of the beam. Below that, it will be installed the various positions of the thrust sensor. It is possible in this way to compute the necessary correlations to compute the main loads and reactions present in the main beam. Assuming the momentum conservation in equation (5.3) around the centre of rotation, it is possible to write the equation that relates the measured load in the sensor according with the load generated by the propeller.

$$\sum M_0 = 0 = -F_{sensor} \times D_2 + F_{motor} \times D_1, \quad F_{sensor} = \frac{D_1}{D_2} F_{motor}, \quad (5.3)$$

With the previous equations, it is possible to compute the maximum load that the measuring system will be able to measure. Also to note the fact that the relation  $\frac{D_1}{D_2}$  will vary along the beam according to the position that the load cell will be. This will mainly depend on the load that the propulsive system will generate. It is possible also to compute the value of the reaction presented in the centre of rotation. Applying the summation of loads in the axis z and y:

$$\sum F_Z = 0 = -F_{sensor} - F_{motor} + B_Z, \quad B_Z = F_{sensor} + F_{motor} = F_{motor} \left( \frac{D_1}{D_2} + 1 \right), \quad (5.4)$$

Finally, it is only necessary to compute the reaction in the Y direction. As it was said before, in this study, due to his small value comparing to the other loads present, it will be discarded the weight of the motor. Also one assumption that was made was discarding the beam own weight.

$$\sum F_Y = 0 = B_Y = 0, \quad (5.5)$$

With this, all the loads present in the main beam are defined. According to the requirements presented in the previous chapter, it will be possible to compute the maximum values of the reactions and loads presented computing a maximum load on the motor of 27 Kg.f and position the load cell in the smallest distance from the pin (55 millimetres). To see the maximum loads in each section of the main beam, it is necessary to compute the shear force and bending moment diagrams for this beam.

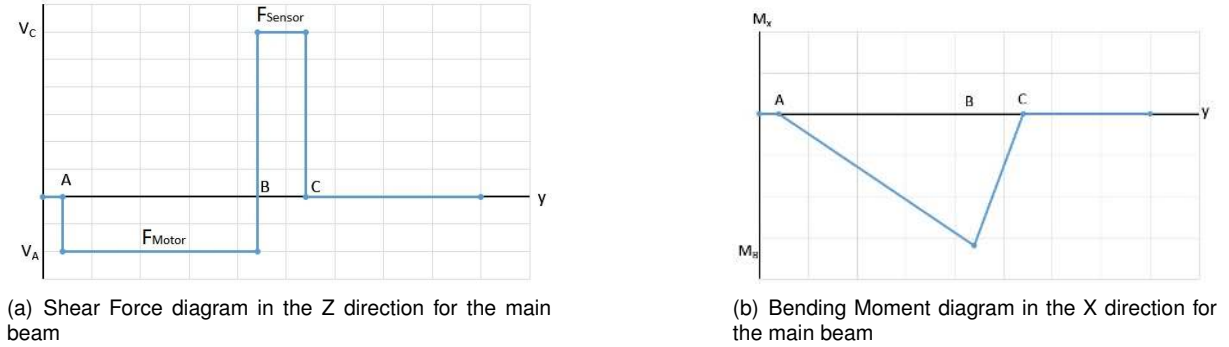


Figure 5.12: Shear and bending moment for the main beam

As it is shown on figure 5.12 a), the shear has null value until the position where the load of the motor is applied. After this, the shear force has a negative shear force until the position B of the main beam (where the pin is). Here increases to a positive shear force value and remains constant until the point where the load cell is located. After this point the beam has null value of shear force. The bending moment (see figure 5.12 b)) is null until the point where the load of the motor is generated and then decreases linearly until B. From B increases linearly until C where it has a null value. Thus, it is possible to say that in this beam, the critical section would be the section B-C having the beam the maximum bending moment at C. Computing the value for the shear force and bending moment:

$$V_C = F_{Sensor} = \frac{D_1}{D_2} F_{motor} = 671.24N, \quad M_B = -F_{Motor} \times D_1 = -147.7Nm \quad (5.6)$$

As it was said before, the geometry selection will depend of the safety coefficient presented for each case. It will be presented three different dimensions for the main beam choosing the suitable one after checking the safety coefficient. Table 5.5 presents the geometric parameters for each dimension studied. Also in figure 5.13 it is possible to see the generic cross section for the main beam.

Thus, it is possible to compute the stress due to bending and shear force and the total Von Mises

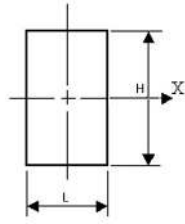


Figure 5.13: Cross section for the main beam

Cross Section L×H [mm]	30x30	30x40	30x50	30x60
$I_{xx}$	$2.32 \times 10^{-8} m^4$	$4.6 \times 10^{-8} m^4$	$7.89 \times 10^{-8} m^4$	$1.233 \times 10^{-7} m^4$
Area	$9 \times 10^{-4} m^2$	$1.2 \times 10^{-3} m^2$	$1.5 \times 10^{-3} m^2$	$2.61 \times 10^{-4} m^2$
$c = \frac{H}{2}$	0.015 m	0.020 m	0.025	0.030 m

Table 5.5: Geometric parameters of the main beam for thickness of 1.5 millimetres

stress (see table 5.6). Remembering the correlation to compute the stress due to bending, shear force and the Von Mises stress:

$$\sigma_M = \frac{M_B \times c}{I_{xx}}, \quad \tau_V = \frac{V_C}{A}, \quad \sigma' = \frac{\sigma_{yield}}{n} = \sqrt{\sigma_M^2 + 3(\tau_T^2 + \tau_V^2)} \quad (5.7)$$

Geometry [mm]	30x30	30x40	30x50	30x60
$\sigma_{Bending}$ [MPa]	95.44	64.17	46.80	35.93
$\tau_V$ [MPa]	3.93	3.34	2.91	2.57
$\sigma_{VonMises}$ [MPa]	95.68	64.43	47.07	36.21

Table 5.6: Stress present in the main beam for different geometries

With this, the equivalent Von Mises stress is computed to each proposed section. It becomes interesting now the selection of the material, never forgetting about the maximum displacement. In table 5.7 is represented the computed values for the safety coefficient using aluminium. As it is possible to see, using aluminium, the suitable geometry for the main beam would be a square beam with 30x30 millimetres of section with 1.5 millimetres of thickness.

However, it is also necessary to compute the safety coefficient for the four different geometries using steel. This is described in the table 5.8. As is it possible to see, using steel in this component the safety coefficient will be higher presenting a more stable structure. With this, it is still necessary to comply with the requirement of the main component do not have a displacement higher than of 5 millimetres. This validation was done using a FEM, and it was done for the beam 30x30 using steel and aluminium. For this simulation, the beam was loaded with the two loads, simulating the load of the sensor and the load of the motor. Two boundary conditions were introduced, one at each side of the beam. The boundary condition was introduced at the point of the centre of rotation and that cylindrical support was constraint and only allowed a rotation at that section. The results are presented in figure 5.14.

As it is possible to see, both materials comply with the requirement of the maximum displacement. Thus, the choice for steel or aluminium will depend only on the cost of the material and also the machining easiness. Also, according to the available machining tools at the shop, it would be much more

Geometry [mm]	30x30	30x40	30x50	30x60
$\sigma_{VonMises}$ [MPa]	95.68	64.43	47.07	36.21
$\sigma_{Yield}$ [MPa]	210			
Safety Coefficient, n	2.19	3.25	4.46	5.79

Table 5.7: Safety coefficient for an aluminium main beam present in the different geometries

Geometry [mm]	30x30	30x40	30x50	30x60
$\sigma_{VonMises}$ [MPa]	95.68	64.43	47.07	36.21
$\sigma_{Yield}$ [MPa]	280			
Safety Coefficient, n	2.92	4.34	5.94	7.73

Table 5.8: Safety coefficient for a steel main beam in the different geometries.

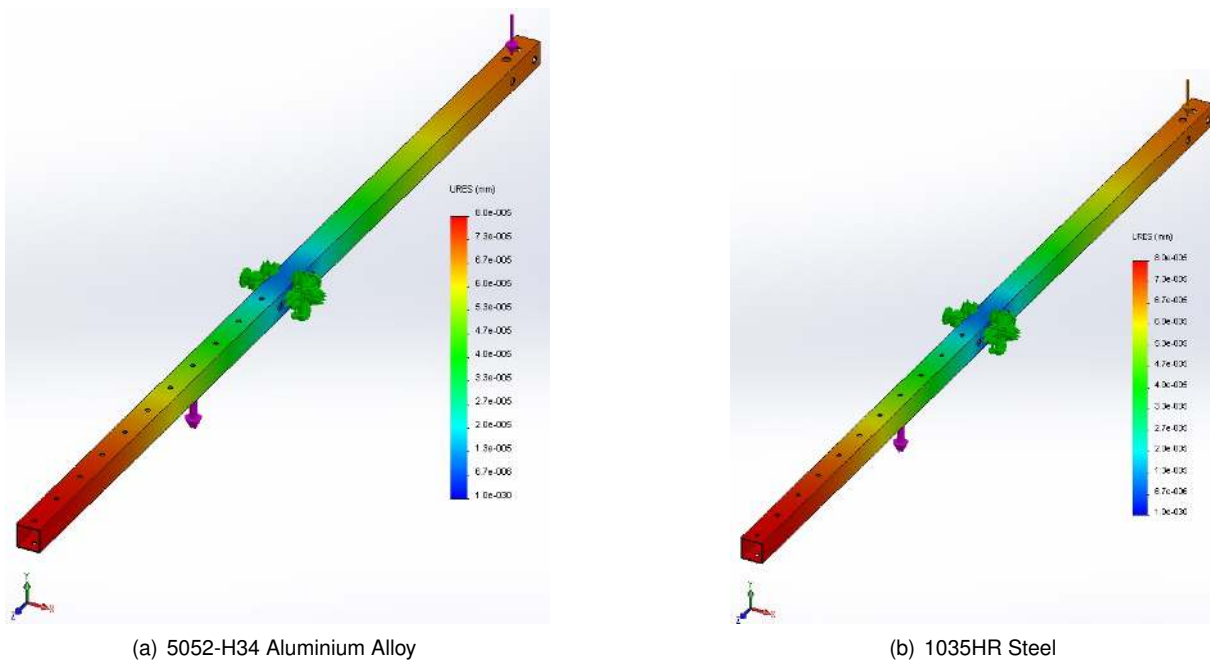


Figure 5.14: FE study for the main beam using different materials.

desirable the use of aluminium.

### Component 3 - Rear Beam

The rear beam will be the component responsible for holding the reaction generated by the load cell. In figure 5.15 it is represented the free body diagram for this beam.

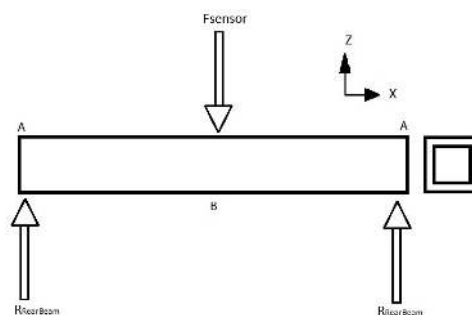


Figure 5.15: Free body diagram for the rear beam

This component will only have the load of sensor and their two reactions acting in its section. To compute the value of the reaction it is necessary to perform the summation of forces in the Z axis.

$$\sum F_Z = 0 = -F_{Sensor} + 2 \times R_{RearBeam}, \quad R_{RearBeam} = \frac{F_{Sensor}}{2} = \frac{D_1 F_{motor}}{2 D_2}, \quad (5.8)$$

Simplified all the loads, it is possible do sketch the shear and bending moment diagram in figure 5.16.

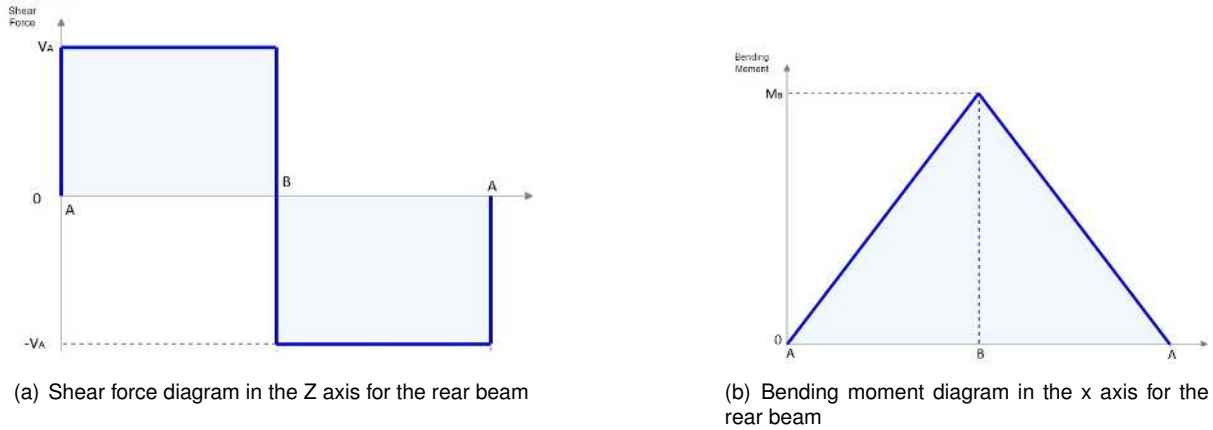


Figure 5.16: Rear beam load diagram.

As it is possible to see, the shear force is constant during all the beam, whereas the bending moment increases linearly until the point B and then decreases linearly. Note that the total distance of the beam is also the total distance from the central axis of the support beams, with the value of 650 millimetres.

$$V_A = R_{RearBeam} = \frac{D_1 F_{motor}}{2} = 335.62N. \quad M_B = V_A \times \frac{L}{2} = 109.07Nm \quad (5.9)$$

Also, with this component, to have a lighter structure as possible, it will be desirable to perform also a geometry and material analysis for this beam. In this case, it will be assumed always a square beam. The choice for square beam was mainly due to the higher inertia moment of thus types of beams that would generate stress in the sections. In table 5.9 it is represented the cases proposed to study. To refer that the thickness considered would be again 1.5 millimetres.

Cross Section L×H [mm]	30x30	40x40	50x50	60x60
$I_{xx}$	$2.32 \times 10^{-8}m^4$	$5.72 \times 10^{-8}m^4$	$1.14 \times 10^{-7}m^4$	$2.0 \times 10^{-7}m^4$
Area	$1.71 \times 10^{-4}m^2$	$2.31 \times 10^{-4}m^2$	$2.91 \times 10^{-4}m^2$	$3.51 \times 10^{-4}m^2$
c	0.015 m	0.020 m	0.025	0.030 m

Table 5.9: Geometric parameters of the rear beam

After this, it is now possible to compute the stress due to shear force, bending and the equivalent Von Mises stress. All this data it is present in table 5.10.

For the selection of the material, it is again considered the same aluminium alloy and steel alloy. With this information, it is possible to compute the safety coefficient for each section. With table 5.11, it is possible to state that the suitable square profile for this component, using the 5052-H34 aluminium

Cross Section L×H [mm]	30x30	40x40	50x50	60x60
$\sigma_{Bending}$ [MPa]	70.48	38.17	23.88	16.33
$\tau_V$ [MPa]	1.96	1.45	1.15	0.96
$\sigma_{VonMises}$ [MPa]	70.57	38.25	23.96	16.42

Table 5.10: Stress present in the rear beam for different cross-section sizes

alloy would be a 30x30 millimetres beam with 1.5 thickness. Also, using steel (see table 5.12), the most suitable beam to use would be a beam with a 30x30 millimetres beam with 1.5 thickness.

Cross Section L×H [mm]	30x30	40x40	50x50	60x60
$\sigma_{VonMises}$ [MPa]	70.57	38.25	23.96	16.42
$\sigma_{Yield}$ [MPa]	210			
Safety Coefficient, n	2.97	5.49	8.76	12.78

Table 5.11: Safety coefficient for an aluminium rear beam for different cross-section sizes.

Geometry [mm]	30x30	40x40	50x50	60x60
$\sigma_{VonMises}$ [MPa]	70.57	38.25	23.96	16.42
$\sigma_{Yield}$ [MPa]	280			
Safety Coefficient, n	3.96	7.32	11.68	17.05

Table 5.12: Safety coefficient for a steel rear beam for different cross-section sizes.

Thus, it is only necessary to verify the component relating with the maximum displacement. Again, using a FEM, the selected geometry was studied. In figure 5.17 it is possible to see the maximum displacement for this component. Once again, using aluminium, the maximum displacement does not exceed 5 millimetres. Thus, for this component an aluminium beam will be used which represents a cheaper and more efficient option.

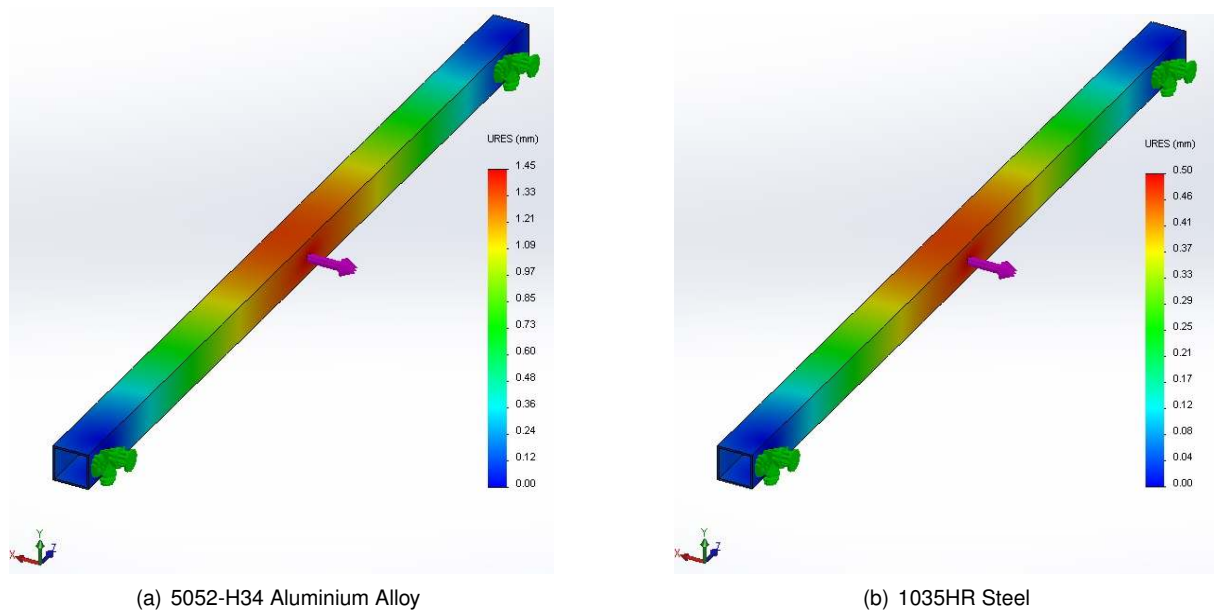


Figure 5.17: FE study for the rear beam using different materials.

### Component 5 - Rotation Pin

It will be only studied in the pin the load in the direction Z. Since the main beam was discarded, the only considerable load are the loads generated by the motor and sensor. Thus, computing the load summation in the direction Z:

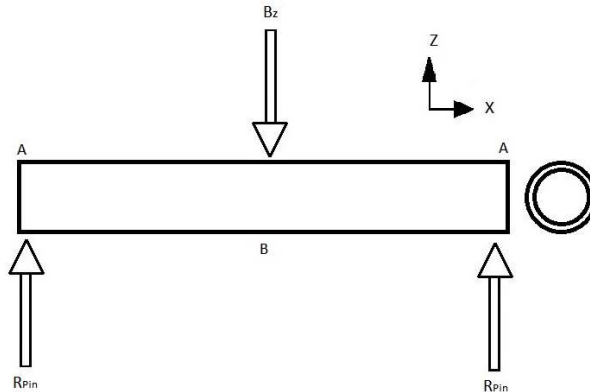


Figure 5.18: Free body diagram of the pin in the main beam of the structure.

$$\sum F_Z = 0 = -B_Z + 2 \times R_{Pin}, \quad R_{Pin} = \frac{B_Z}{2} = \frac{F_{sensor} + F_{motor}}{2} = \frac{F_{motor} \left( \frac{D_1}{D_2} + 1 \right)}{2} \quad (5.10)$$

Similarly of what was done with the other two components, it was sketched in figure 5.19 the shear force and bending moment diagrams for this component:

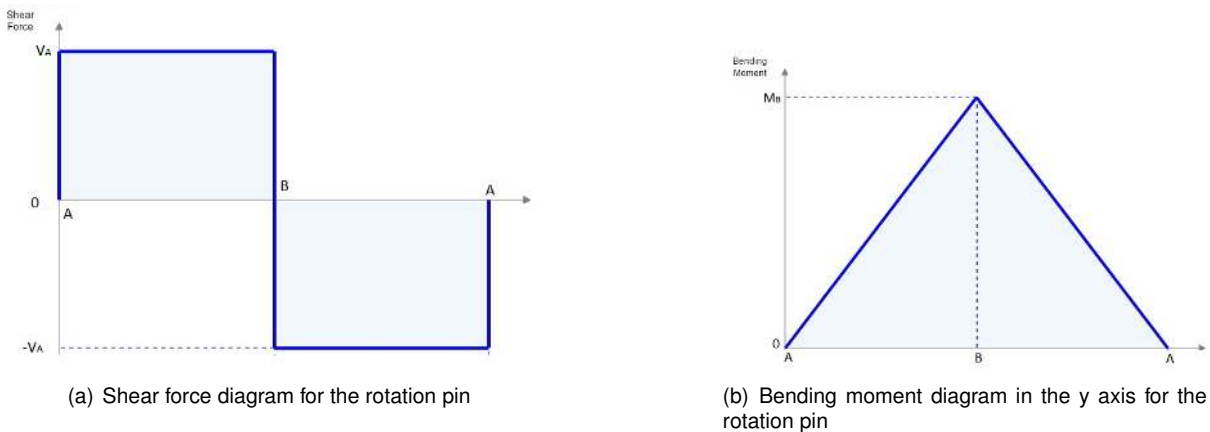


Figure 5.19: Rotation pin load diagram.

With this, it is possible to compute the values for shear force and bending moment on the critical section, B.

$$V_A = R_{Pin} = 469.87N \quad (5.11)$$

To compute the bending moment at the critical section it is necessary to refer that load  $B_Z$  it is applied in the middle of the main beam. The distance from the point A to the point B it will be half of his width,

325 millimetres.

$$M_B = V_A \times 0.325 = 152.70Nm \quad (5.12)$$

To design and study the dimensions of the profile for this component, it will be required a special material since the moment generated it too big due to the high distance from the supports. With this, it was searched for special steels for machine and steel tools. The study, will have in mind the dimensions of the main beam, which are 30x30 mm.

Diameter [mm]	12	15	17	20
$I_{xx}$	$1.01 \times 10^{-9}m^4$	$2.49 \times 10^{-9}m^4$	$4.1 \times 10^{-9}m^4$	$7.85 \times 10^{-9}m^4$
Area	$1.13 \times 10^{-4}m^2$	$1.77 \times 10^{-4}m^2$	$2.27 \times 10^{-4}m^2$	$3.14 \times 10^{-4}m^2$
r	$6 \times 10^{-3}m$	$7.5 \times 10^{-3}m$	$8.5 \times 10^{-3}m$	0.010 m

Table 5.13: Geometric parameters for different diameters of the pin.

Diameter [mm]	12	15	17	20
$\sigma_{Bending}$ [MPa]	900.11	460.86	316.59	194.44
$\tau_V$ [MPa]	4.15	2.66	2.07	1.50
$\sigma_{VonMises}$ [MPa]	900.14	460.88	316.61	194.44

Table 5.14: Stress present in the pin for different diameters

As it is possible to see in table 5.14 that pin, with a diameter larger than 15 millimetres may be suitable for the test rig. Due to the high Von Mises stress present in the pin, it would be necessary the use of a special material/steel for this component. After some market research, it was chosen the re-seller Ramada Aços[33] for the pin. For this part, it was decided to use steel mainly due to the high stress presented in this component but also it was desirable to have a stiff material that would not allow such high displacement when loaded. The mechanical properties of this steel can be consulted in table 5.3.

Diameter [mm]	12	15	17	20
$\sigma_{VonMises}$ [MPa]	900.14	460.88	316.61	194.44
$\sigma_{Yield}$ [MPa]	820			
Safety Coefficient, n	0.91	1.77	2.58	4.21

Table 5.15: Safety coefficient for a steel pin for different diameters

As it is possible to see, the suitable diameter for the pin will be 17 millimetres. One great concern that it must to be taken into account is the diameter of the bearing housing unit. Searching on the database of the manufacturer, it is clear that the diameter 17 is available for this component. Details about the housing units can be found in appendix B.

## Component 2 - Support Beam

The loads that will be presented in the support beams are the load transmitted from the main beam and the rear beam. The load will be transmitted from the main beam to this beam through the pin that crosses the bearing housing unit and the main beam. Also the rear beam will be attached to each support beam



that will transmit a load to this component. In figure 5.20 it is possible to see the free body diagram of this component.

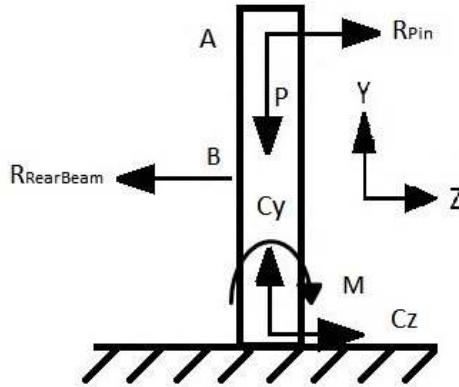


Figure 5.20: Free body diagram of the forces present in the support beam

This beam will be a cantilever beam. In point C, this beam will have reactions in both Y and Z directions but also a momentum. Also the load P could be assumed as the load of the weight of the main beam, divided by two, since the main beam is supported by two support beams. However, as it was assumed before, it was discarded the own weight of the main, so in this case this load could be considered null. Applying the summation of loads in the direction Y:

$$\sum F_Y = 0 = B_Y - P, \quad B_Y = 0 \quad (5.13)$$

Also, to compute the reaction in the point B in the direction Z, the support beam will only have the reaction of the pin present in this direction. As it was said before and discarding again the beam own weight, this load will be half of the reaction Z in the pin on the main beam. Performing the equilibrium of forces in the Z direction:

$$\sum F_Z = 0 = R_{Pin} - R_{RearBeam} + C_Z \quad (5.14)$$

$$C_Z = R_{RearBeam} - R_{Pin} = \frac{D_1 F_{motor}}{2} - \frac{F_{motor} \left( \frac{D_1}{D_2} + 1 \right)}{2} = -\frac{F_{Motor}}{2} \quad (5.15)$$

After this, it is only necessary to compute the moment present at the cantilever base. This can be computed with the momentum balance at the point C. To refer that the distance from the point C and the point where the load is applied is 645 millimetres.

$$\sum M_C = 0 = M_C - R_{Pin} \times 0.645 + R_{RearBeam} \times 0.425 = 0 \quad (5.16)$$

$$M_C = R_{Pin} \times 0.645 - R_{RearBeam} \times 0.425 = \frac{F_{motor}}{2} \left( \left( \frac{D_1}{D_2} \right) \times 0.220 + 0.645 \right) \quad (5.17)$$

Similarly to the main beam, the support beam will have almost the same shear force and bending

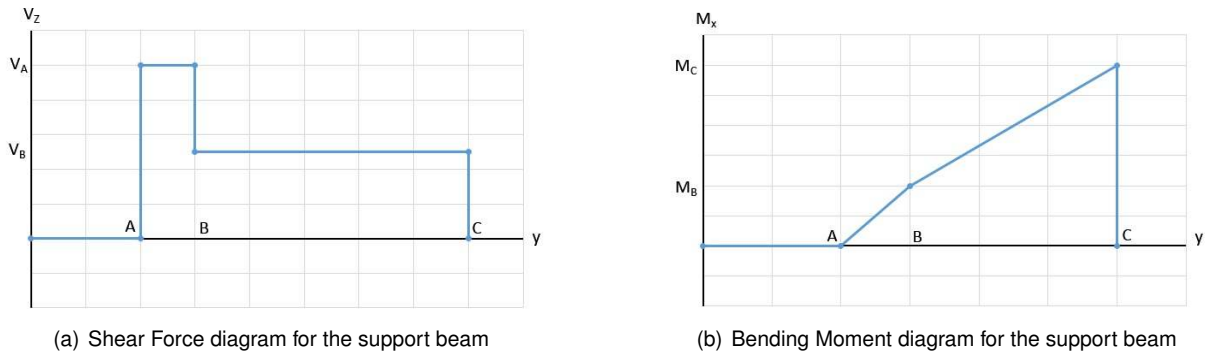


Figure 5.21: Load diagram for the support beam

moment diagram. As it is shown in figure 5.21 a), the shear force will have a positive and maximum value at the point where the load  $R_{Pin}$  is applied and at the point B, the shear force decreases to  $V_B$  where remains constant until the point C. The bending moment (see figure 5.21) a) will increases linearly from the point A and at point B increases with a smaller slope until the point C. where is maximum.

Finally to the last component it was done the same study for the dimensions of the profile and also the study for the material selection. It will be assumed for this component a square beam:

Geometry [mm]	30x30	40x40	50x50	60x60
$I_{xx}$	$2.32 \times 10^{-8} m^4$	$5.72 \times 10^{-8} m^4$	$1.14 \times 10^{-7} m^4$	$2.0 \times 10^{-7} m^4$
Area	$1.71 \times 10^{-4} m^2$	$2.31 \times 10^{-4} m^2$	$2.91 \times 10^{-4} m^2$	$3.51 \times 10^{-4} m^2$
c	0.015 m	0.020 m	0.025	0.030 m

Table 5.16: Geometric parameters of the support beam

With the figure 5.21 it is possible to compute the maximum shear force and bending moment present in the beam:

$$V_A = \frac{F_{motor} \left( \frac{D_1}{D_2} + 1 \right)}{2} = 469.87N, \quad M_C = V_B \times 0.725 = \frac{F_{Motor}}{2} \times 0.645 = 86.59Nm \quad (5.18)$$

Geometry [mm]	30x30	40x40	50x50	60x60
$\sigma_{Bending}$ [MPa]	55.95	30.30	18.96	12.97
$\tau_V$ [MPa]	2.75	2.03	1.61	1.34
$\sigma_{VonMises}$ [MPa]	56.16	30.51	19.16	13.17

Table 5.17: Stress present in the support beam for different cross-section sizes

Similarly to what was done previous, it is going to be presented the safety coefficient for an aluminium and steel. Alloy beam, in tables 5.18 and 5.19, respectively.

With this, it is clear that the choice will focus on the square beam 30x30 mm with 1.5 mm thickness. The aluminium beam will present a more well designed beam, since its safety coefficient is closer than two. However, it is still necessary to validate the maximum displacement that this beam would have using steel and aluminium.

Geometry [mm]	30x30	40x40	50x50	60x60
$\sigma_{VonMises}$ [MPa]	55.95	30.30	18.96	12.97
$\sigma_{Yield}$ [MPa]	210			
Safety Coefficient, n	3.75	6.93	11.07	16.19

Table 5.18: Safety coefficient for an aluminium support beam for different cross-section sizes

Geometry [mm]	30x30	40x40	50x50	60x60
$\sigma_{VonMises}$ [MPa]	55.95	30.30	18.96	12.97
$\sigma_{Yield}$ [MPa]	280			
Safety Coefficient, n	5.0	9.24	14.76	21.58

Table 5.19: Safety coefficient for a steel support beam present for different cross-section sizes

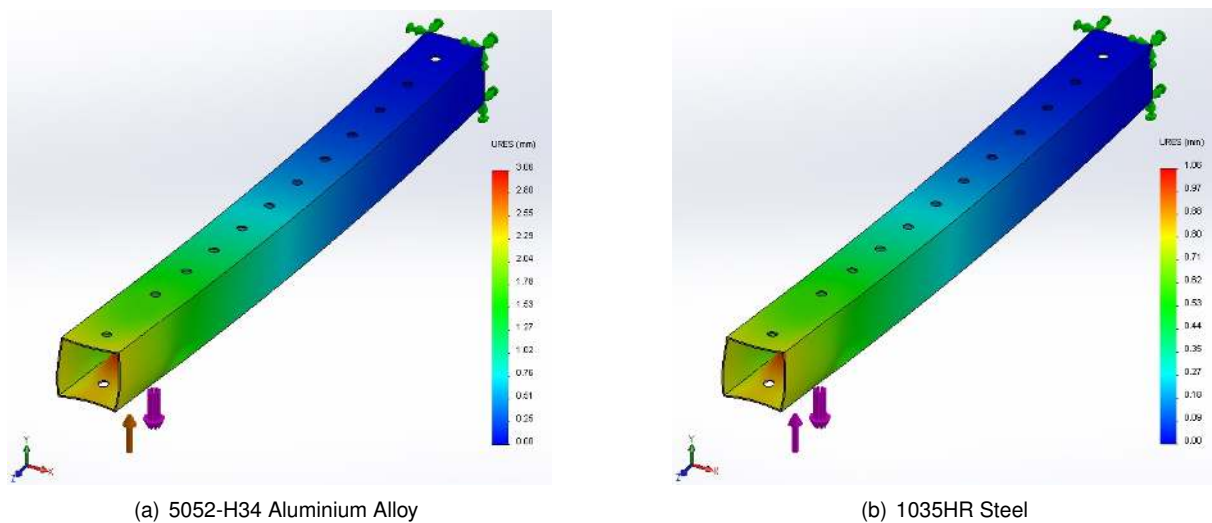


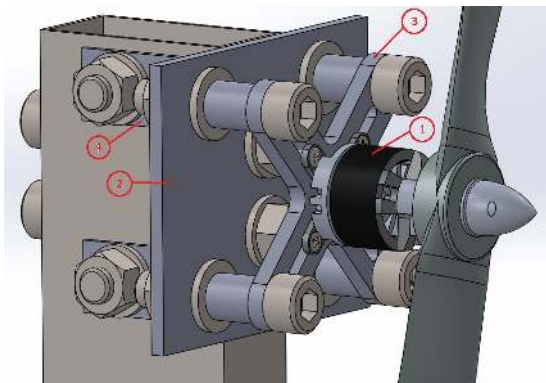
Figure 5.22: FE study for the support beam using different materials.

As it is possible to see in figure 5.22, the component is validated with both materials, 1035HR Steel and 5052-H34 Aluminium Alloy. For the reasons presented before, it was chosen the aluminium material.

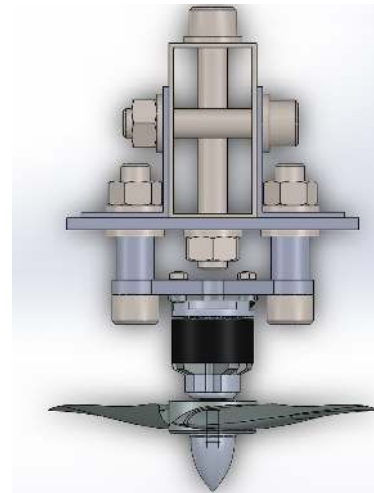
## 5.4 Assembly Motor+Propeller

Finally, it is only necessary to design the connection propeller-motor-beam. The main requirement for this connection was the flexibility that will allow to test different motors. As it was said in the previous chapter, the test rig has to be capable of testing at least three different diameters of motors that will perform tests to three different ranges of propellers. With this, it was designed the structure presented in figure 5.23.

In the table 5.20 it is possible to see described the main components for this structure. Due to the designed cross, this will allow to attach motor with a minimum diameter of 15 millimetres and a maximum diameter of 55 millimetres. This 55 millimetres refers to the diameter of the fixation system that each motor has. In practice the motor can have a large diameter. It was also installed reinforcements to have a better stabilization of the plate to the beam. It was installed on the back of the plate, L plates to connect the beam and the plate. With figure 5.23 b) is possible to see the top view of the structure. The



(a) Perspective view



(b) Top view

Figure 5.23: Complete support structure for the motor in the main beam

Component	Name
1	Motor
2	Support Plate
3	Structural Cross
4	L connection

Table 5.20: Description of the components present in the structure motor+propeller

plate is supported by six bolts that crosses the beam. Two directly attached from the beam to the plate and another four from the L plate attached to the beam and the plate. The L plates were designed in such way that the bolts could cross the beam without interfere with the other two bolts that are passing through the beam.

Also, it was installed in each support of the cross, a spacer to allow the assemble of the cross on the beam. Due to the nuts and washer attached on the plate, to not interfere with the cross, it was designed this solution.

For the verification of this components, in this section it was used a simulation based on FEM. Since the beam was already verified to safety in the previous section, it was consider only important to test and check the stresses (Von Misses) present in the structural cross that was designed.

In figure 5.24 it is possible to see the result of the FE simulation to the component when loaded with the critical load that the motor generates. Since the cross as a great variety of bores, which represent areas where there are large stress concentrations, the area of the part that would have an higher value of stress would be around the bores. However, as it is possible to see in the figure, the maximum value is 21.5 MPa, a value which is very small when compared to the yield stress of the material used for this component (Steel AISI 1035 CD).

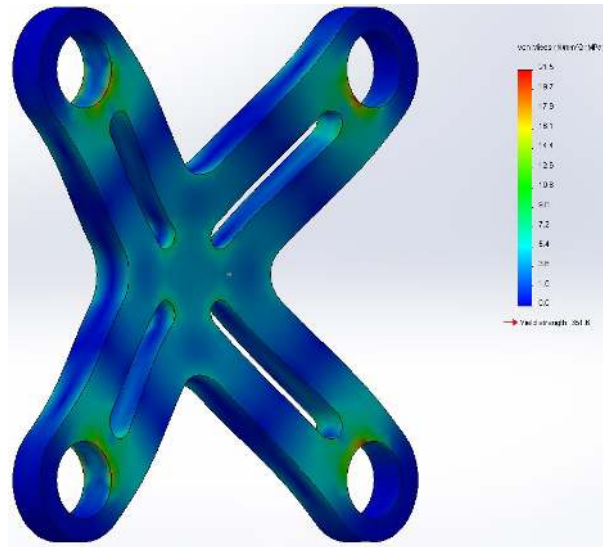


Figure 5.24: FE simulation of the designed motor support cross

## 5.5 Support Foundation Design

The support foundation is the base that will hold all the structure. This support foundation must take into account the present physical requirements of the wind tunnel. As it was described in chapter 4, the structure will be positioned 1.45 meters from the wind nozzle tunnel, having a maximum width of 0.68 meters. Another factor to consider is that the supports where the foundations of the structure are going to be settled are not aligned with the other side of the wind tunnel floor.

### 5.5.1 CAD Model

For this, as it was said before, the main constraint that would define the structure were the physical requirements made by the mounting area (wind tunnel). The first structure/solution that was sketched is represented in figure 5.25.

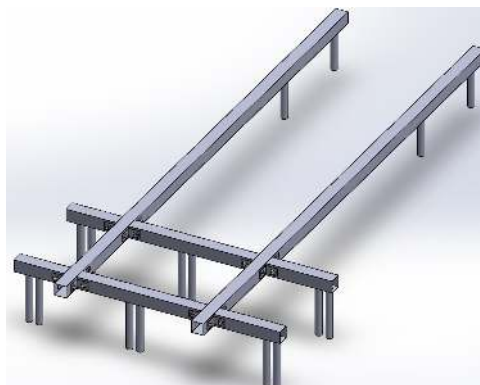


Figure 5.25: Sketch of the foundation of the structure

This foundation represents a good structural foundation, that will hold a good amount of height. However, as it is possible to see, it could be difficult to build due to the amount of beams involved in the structure. Also the probability of having a wrong measure is high due to the amount of beams and

also supports that this foundation has. Thus, it was designed a much simple foundation, represented on figure 5.26 a), having only three beams. These three beams will be attached one above the other. As it is possible to see, the amount of supports was substantially reduced as well as the connections between the beams.

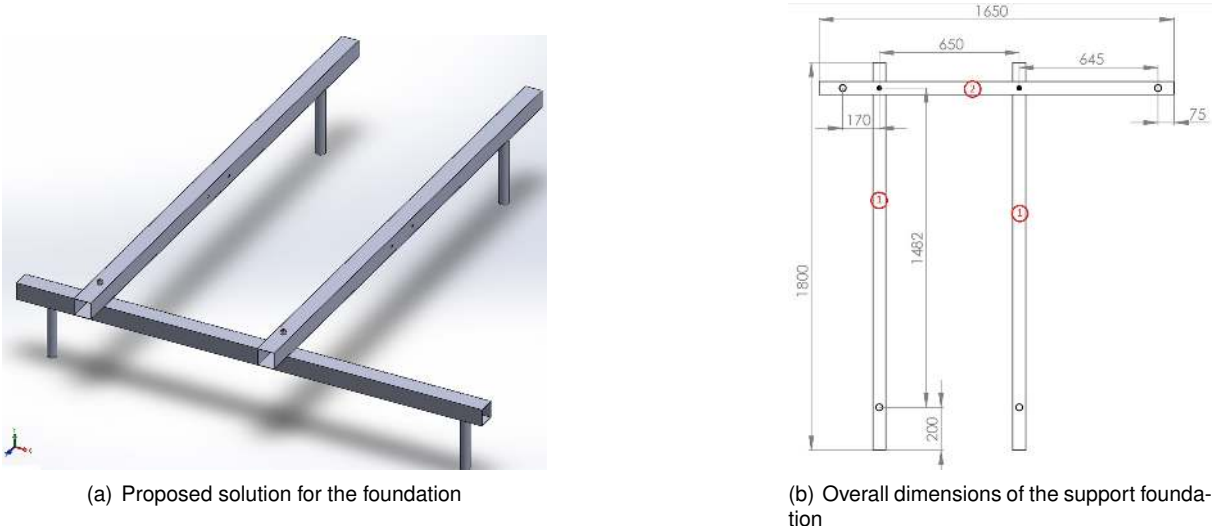


Figure 5.26: Main characteristics of the support foundation

### 5.5.2 Overall Dimensions and Components

After defining the CAD design, it becomes necessary to define the overall dimensions of the foundations (see figure 5.26 b)). These dimensions, as it was said before, are constraint by the dimensions of the wind tunnel testing area.

Component	Name	Dimensions [mm]
1	Primary Beam	30x60x1800 (t=1.5)
2	Secondary Beam	30x60x1650 (t=1.5)

Table 5.21: Description of the structural components present in the support foundation

### 5.6 Aerodynamic Shielding

As it was introduced in the previous sections, since the structure will be subjected to dynamic forces generated for the wind, it was necessary to design an aerodynamic structure, whose main purpose would be to protect the main beam from the wind to not influence the results measured. This shielding had to be enough aerodynamic to generate the lowest noise possible. Also, the vibration generated by the wind passing through the shielding would generate vibrations that could add additional forces to the load cell or even damage the main beam.

Thus, first it was decided to use a square aluminium beam 50x50 millimetres to accommodate the main beam. It was decided to install between the two secondary beam of the foundation, a solid wood

table in order to have a solid place to fix the shielding and the beam of the shielding. Also having the solid table would help the user to have a stable place to be whenever it is necessary changing a motor, propeller or even correct some wiring problem. With this, it was used the square beam with 1.2 meters of length. When assembling the main beam inside this one, the big concern that come up was to accommodate it in order to never touch on the inside walls of the square beam. In figure 5.27 it is sketched the purposed assemble described during this paragraph. Also referring to this beam, it is necessary to drill the beam with the exact holes of the main beam in order to be possible to attach from outside the screws to attach the load cell to the main beam. Finally, as it is possible to see, the bearing housing units installed on the main beam do not have only 10 millimetres of height. In order to install correctly it without any disturbance, it was machined 2 tears on the square beam to allow the bearing housing units to be outside of the square beam without touching it but also to maintain the flexible assemble of the structure.

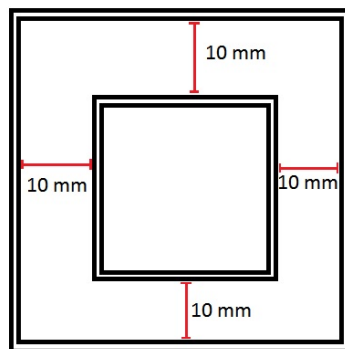


Figure 5.27: Top View assemble of the shielding square beam

Defined and machined the square beam, it is now necessary to define the aerodynamic profile to be installed on the shielding. For this, first it was chosen an aerodynamic profile from the database available[34]. It was chosen the structural airfoil profile EPPLER 863 STRUT AIRFOIL. The main reason for choosing this airfoil was for being an structural and symmetrical airfoil but due to the mounting dimensions the profile would have an high chord/thickness ratio. Chosen the airfoil, it was made an aerodynamic analysis using the software XFOIL[35]. When validating this airfoil, it would be desirable to have the lowest drag coefficient as possible to generate the lowest force on the square. Also it would be desirable to have separation of the boundary layer as far as possible of the square beam since to generate the lowest noise and to reduce at maximum the vibrations. As it is described on the plot generated from the software (see figure 5.28), the airfoil selected complies with the requirements defined during this paragraph. Noting that for this analysis a wind speed of 30 m/s was considered using a Reynold number based on a air density at 20°C.

Validated the airfoil based on the aerodynamic analysis, it passed to the production of the airfoil. Choosing the material for this airfoil depended to the available cutting tools present in the laboratory. It was available a hot wire cutting machine in the laboratory (see figure 5.29) equipped with CNC software. Thus, it was decided to use foam XPS, mainly used for coating of houses. This material present a good structural reliability but it is also easy to machine. Before starting to cut, first it was necessary to

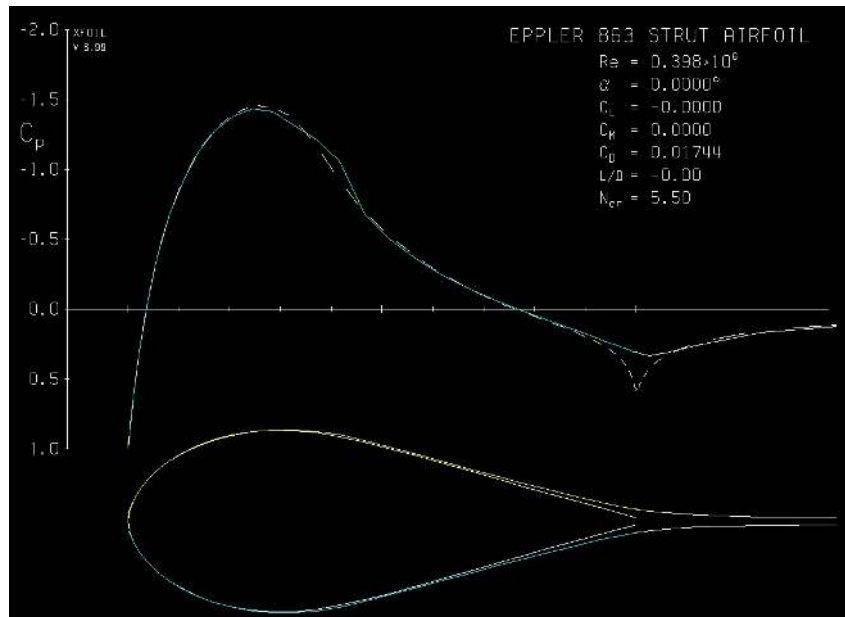


Figure 5.28: Aerodynamic study of the airfoil EPPLER 863 STRUT AIRFOIL using the software XFOIL

calibrate correctly the machine, to have a good surface finish. It was tried different voltages on the wire until reached a good surface finish when cutting.

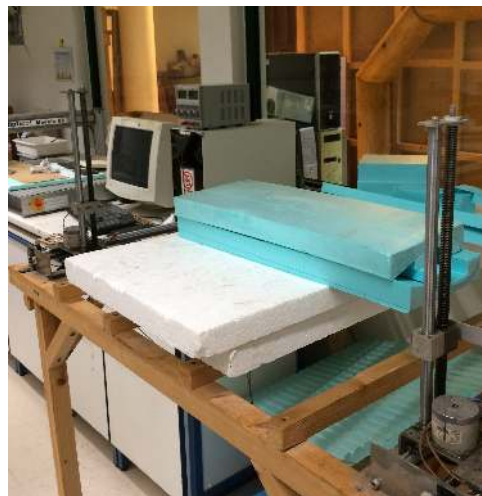


Figure 5.29: Hot wire cutting machine present in the laboratory

After this, it was loaded the profile of the airfoil on the computer and then cut. After cutted the outer shape, it was then cutted the housing where the square beam would be fitted. This cut generated several problems since the foam would only have around 10 millimetres between the cut and the profile what sometimes damage the profile due to the high temperature of the wire gets closer of the lowest thickness on that area. After removing the housing, the airfoil was then cutted in two halves in order to be easy to assemble the structure. It is possible to see in figure 5.30 the different phases of the cutting process of the wing. To note that due to the dimension of the foam and also to have a more stable cut the airfoil was divided in three sections.

Cut the three sections, it was necessary to cover the wing to allow a better structural stability but also





(a) Progress during the cut of the airfoil



(b) Airfoil already cut and ready to be covered

Figure 5.30: Different phases of the cutting process of the airfoil

to join the two halves of the airfoil. It was decided to use aluminium ductape to cover all the wing. In figure 5.31 it is possible to see the final design for the shielding. As it is possible to see, it was left enough space in the middle of the square beam so it could be possible to accommodate the bearing housing unit.

## 5.7 Final Design and Build

After reviewed and build all the components, it was possible to assemble all the structural components in the wind tunnel. First it was mounted the structure without any sensors just to check if everything fitted correctly on the foundation. Then it was mounted the solid table that would allow to fix the wing and the user to stand near the test rig. Then finally the whole structure was mounted inside the wind tunnel. This process is possible to see in figure 5.32

Power coefficient versus advance ratio,  $p/D$  a parameter



(a) Side view



(b) Back view

Figure 5.31: Final design for the aerodynamic shielding



(a) Foundation and support



(b) Main beam and pin



(c) Bottom plate



(d) Final assembly

Figure 5.32: Process of assembling the structure of the test rig

# Chapter 6

## Sensing, Data Acquisition and Control

After the assembly of the test rig, it is necessary to install several sensors that will allow to measure and produce the desired output. In chapter it will be presented the selected sensors that were installed in the test rig, their wiring layout and specially the user interface created to enable the use of test rig in a simple and practical way.

### 6.1 Summary of Measuring Quantities

Before starting to introduce the selected sensors, it would be a good exercise to review all the output data that will be generated on the test rig. This is summarized in table 6.1.

Measured Quantity	Min	Max
Interior Temperature	0°C	50°C
Motor Temperature	0°C	65°C
Thrust	0 Kg	30 Kg
Current	0 A	77.5 A
Tension	0 V	50 V
RPM	0 RPM	20000 RPM
Air Stream Velocity	0 m/s	30 m/s

Table 6.1: Summary of measured quantities and respective ranges

### 6.2 Sensor Selection

#### 6.2.1 Load Cell

For the load cell it was chosen a sensor that enables an assemble in the designed structure but also provides an adequate measuring range. It was chosen a S-type load cell from the manufacturer Vishay[36].


The load cell can be loaded either in traction or compression, and used for single or multiple-cell applications if the output is rationalized. As it was written before, it would be necessary at least three ranges of measuring thrust due to the variety of propellers sizes. It was order three load cells with a load capacity of 5,10 and 25 Kg.f. The signal conditioner BA660[36] was used to amplify the analog voltage output of the load cell, from mv to V in order to have a better fillment of the range values. In figure 6.1 it is possible to see the load cell and the signal conditioner used. Their DataSheet can be found on the Appendix B.



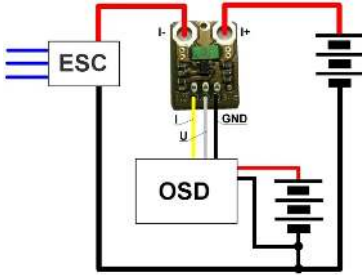
Figure 6.1: Load Cell

**6.2.2 Voltage and Current Sensor**

After some research, it became apparent that the best solution was to use a sensor that could read both voltage and current, since it would simplify the wiring and lower the cost. In figure 6.2 it is possible to see the characteristics of the Pitlab 75A sensor[37] that was selected. It was chosen the 60 V version. Also in the same figure, it is represented the wiring layout for this sensor.

Sensor	Max Voltage	Max Current
 Pitlab's 75 A current sensor	36 V	75 A
	60 V	75 A

(a) 75A PitLab



(b) Wiring layout

Figure 6.2: Voltage and current sensor

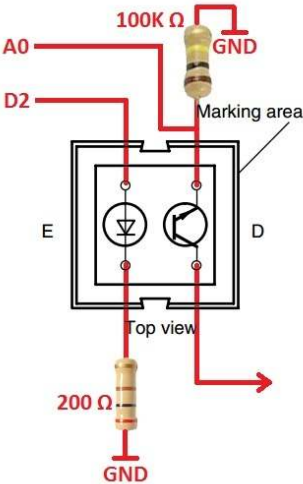
**6.2.3 RPM Sensor**

During the market search for a solution for RPM measurement, several different solutions were found that could be used in the test rig. First it was applied an LDR sensor. This light-dependent resistor (LDR) or photocell is a light-controlled variable resistor. The resistance of a photoresistor decreases with increasing incident light intensity; in other words, it exhibits photoconductivity, however it was clear

that it was not a suitable solution since the RPM measured were not stable and also the measure was not clear. With this, it was chosen the Reflective Optical Sensor with Transistor Output CNY70 from Vishay[36]. This sensor produced stable RPM readings and the range of RPM allowed was also of large scale. For measuring the RPM of the motor a tape with a white and black part was installed around the all Diameter of the motor . When passing to the black part of the tape, the sensor will generate a signal (and Voltage) with a different frequency. That change in frequency when multiplied by 60 ( seconds in 1 minute) will give the exact number of RPM of the motor. In figure 6.3 it is possible to see the sensor used. Also, its datasheet is present on the Appendix B.



(a) Optical Sensor CNY 70 from Vishay



(b) Wiring layout

Figure 6.3: Reflective optical sensor Vishay CNY70

### 6.2.4 Temperature Sensor

The temperature sensor was necessary for measuring the temperature of the air stream but also to measure the temperature of the motor. After market research, it was chosen the Thermocouple TMP36GZ produced by Analog Devices[38]. This Thermocouple allowed temperature from -40°C up to 125°C. The sensor is represented figure 6.4 and its DataSheet is also present on the Appendix B.



Figure 6.4: Temperature sensor Analog Devices TMP36GZ

### 6.2.5 Air Speed Sensor

To measure the air stream speed sensor the wind tunnel test section a dynamic and static pressure was employed. With the total and static pressure measured, the sensor gives the difference between both and then it is possible to compute the velocity through Bernoulli equation as explained in section 4.5. The sensor used was a Freescale Semiconductor MPXV7002DP. The system acquisition has two sensors integrated in a printed circuit built purposely. The first sensor measures the static pressure and the second the "active" or total pressure. The sensor is shown in the Figure 6.5. Also in the Appendix B is presented the DataSheet for this sensor.



Figure 6.5: Differential sensor Freescale Semiconductor MPXV7002DP

### 6.3 Motor Speed Control

For controlling the speed of the motor, as it was said before it is necessary to install an Electronic Speed Control(ESC). This device allows to control the speed of the motor through a PWM signal (Pulse Width Modulation). To ensure a better usage of the test rig, this control is performed through the LabView Interface. The input of the motor is a PWM signal with a frequency of 500 Hz, corresponding to a period of 2 ms. In the modulation, the duty cycle of the signal is varied so that 0% of duty cycle corresponds to 0% of throttle. The term duty cycle describes the proportion of 'on' time to the regular interval or 'period' of time; a low duty cycle corresponds to low power, because the power is off for most of the time. Thus, when a 100% duty cycle is applied, the period of the signal remains the same, however the time that the signal is on increases. This procedure is described in figure 3.15.



Figure 6.6: Servo tester used in the first test runs

However, during the first phase to calibrate and test the motor, a Servo Tester was used. This device

generates a PWM signal which is sent to the ESC and can be varied through a knob. The servo tester used is represented in figure 6.6.

For generating the signal in labview it was use the block *Simulate Signal*. This block generates a square wave with a constant period with which is attached a slide bar to regulate the duty cycle. However since 0% of duty cycle represents a wave with 1 ms "on", it was necessary to perform a simple rule of three to calculate the real duty cycle that corresponds to the simulated signal. This signal would be exactly the same as the one generated by the servo tester. The block used for generating the PWM can be seen in figure 6.7.

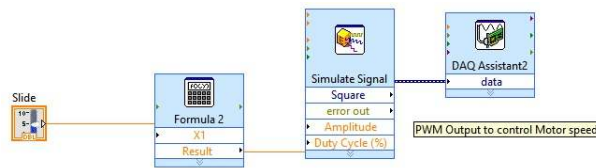


Figure 6.7: Block used on LabView to generate the PWM signal to control the motor speed

## 6.4 Data Acquisition System

To read all the sensors outputs and record them, a data acquisition (DAQ) system will be used. This system will be comprised of a data acquisition board connected to a computer. The DAQ board, previously acquired, is the National Instrument NI PCIe-6321 (Figure 6.8)[39], which has 16 analogue +/-10 V inputs, connected to a computer running LabView, to read, convert and record the data acquired from the sensors.

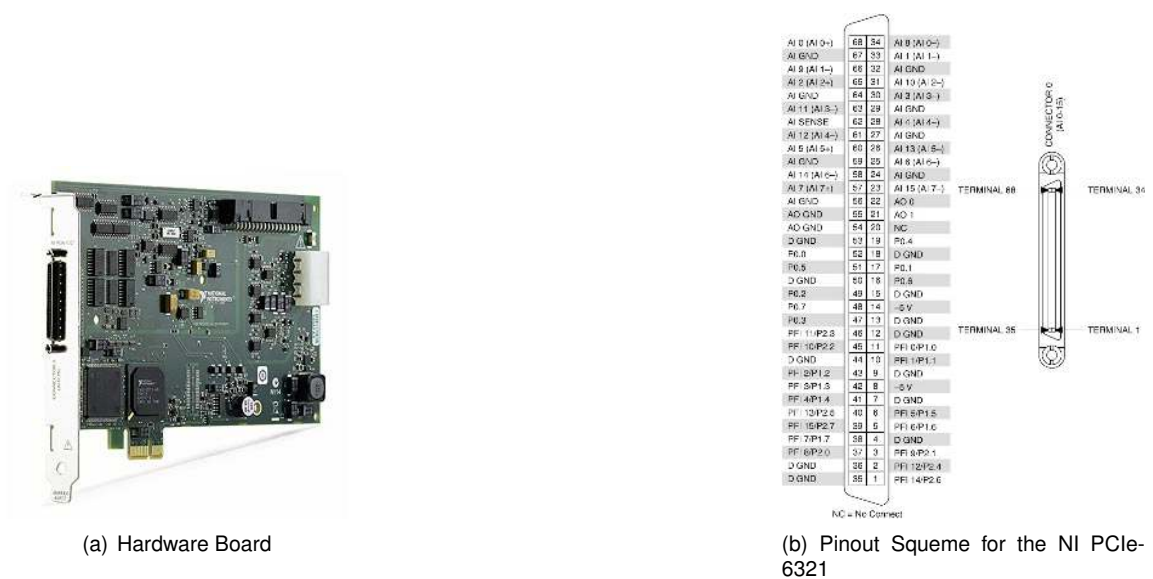


Figure 6.8: National Instruments NI PCIe-6321[39]



### 6.5 Wiring Layout

In this section, all the necessary wiring connections made during the set up of the sensors. The diagram present in figure 6.9 represent the detailed wiring of all the sensors installed in the test rig. In the real test rig, the Grounds of all sensors were connected to the respective Ground of the Analog Input on the NI DAQ. In the layout these were simplified. Also to refer that the load cell was calibrated to be continuously excited with a DC Voltage of 10 Volts. Also the NI DAQ does not have enough +5V to feed all the sensors. The +5V were connected to a breadboard were were available the +5V for all the sensors.

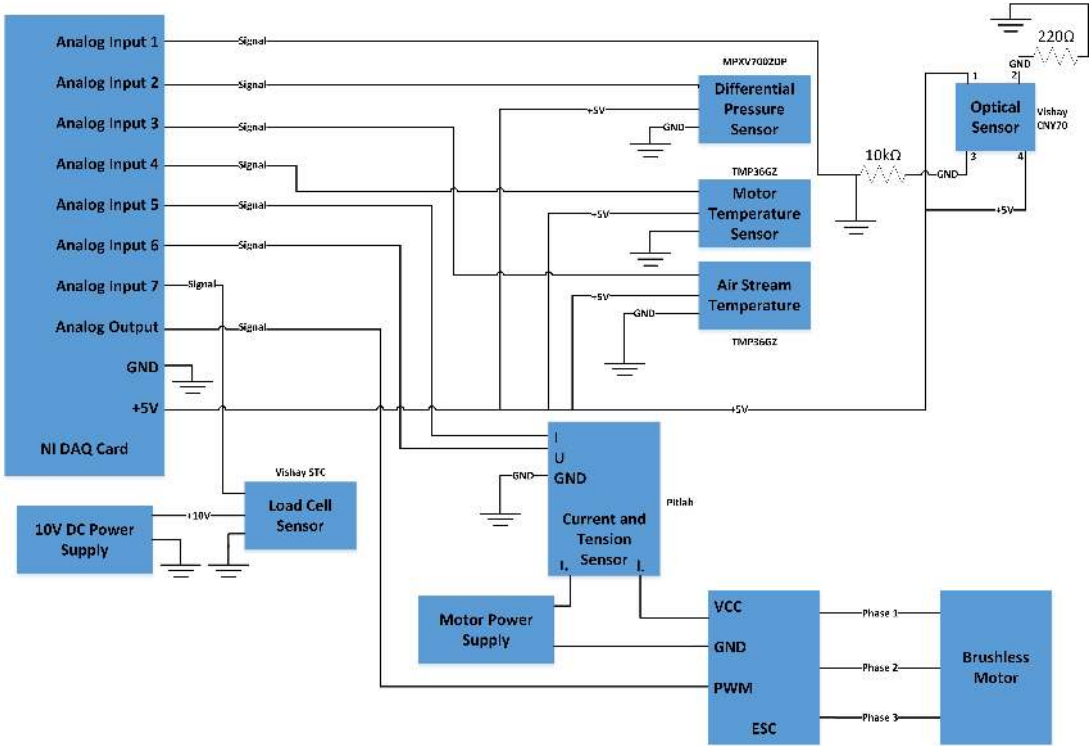


Figure 6.9: Electrical layout of the test rig

### 6.6 User Interface

As it was discussed before, the user would have to be capable of working with the test rig in a simple way but also have to be capable of see the output data generated from the test rig. For this purpose, a graphical interface on the software LabView was created. This interface is shown in figure 6.10.

In this interface, before starting the test, the user needs to give the correct position of the load sensor using a select box with all the values of possible relations  $\frac{D_1}{D_2}$ . This is necessary since the correct thrust value depends on the position of the load cell. After this, the user can start the program. To increase the throttle of the motor, the user has a slide button which goes from 0% up to 100%. Then the program is equipped with several gauges that allow the user to see the different values measured with the sensors.

An overview of the blocks used in the labview interface is shown in figure 6.11.

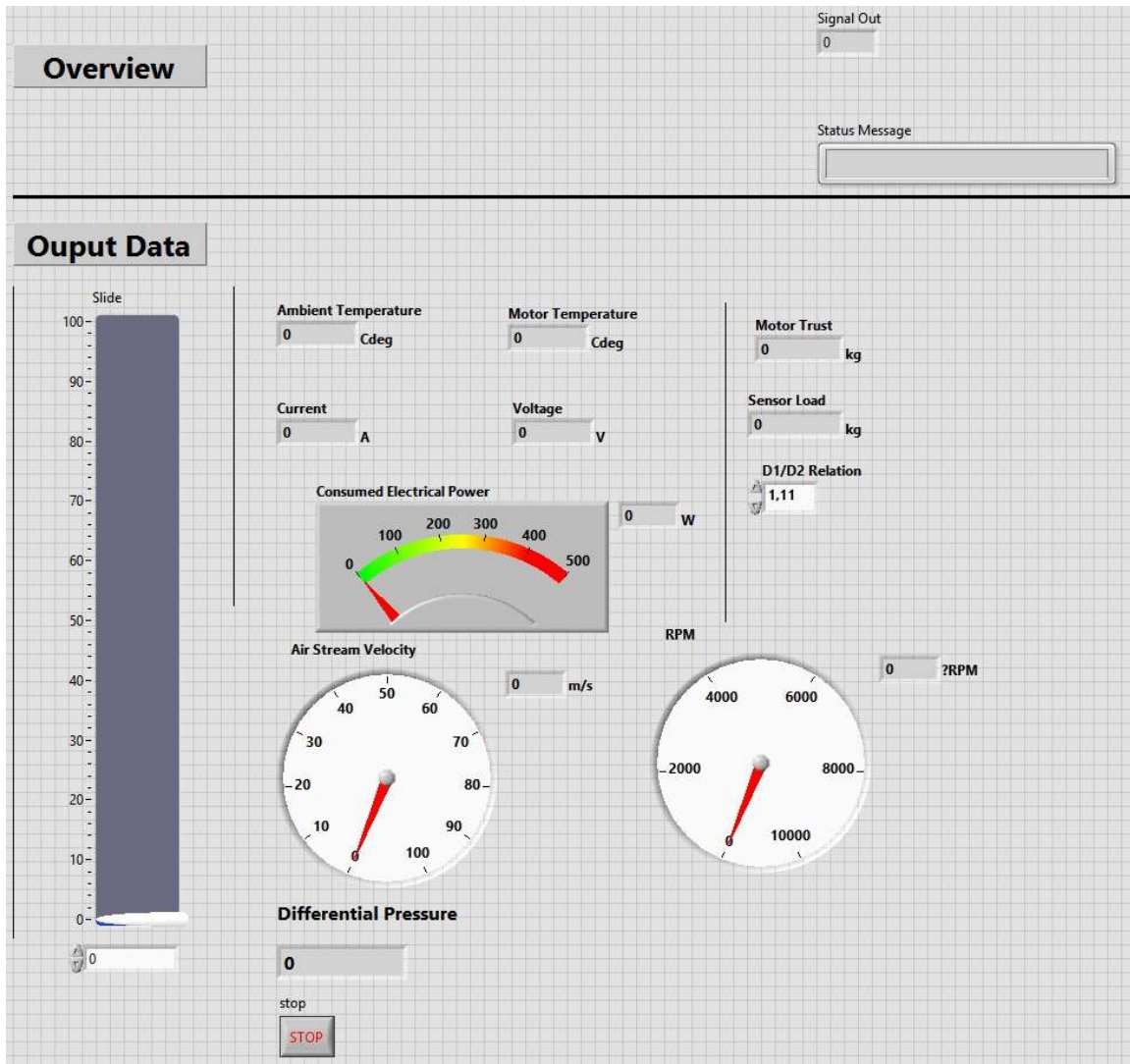


Figure 6.10: Graphical Interface for Operating the test rig

## 6.7 Recorded Data

The recorded data of each test will be done in the excell. Labview will record the data in an excel file where which colum has the value recorded at each millisecond or depending the recording chosed. This table can be seen in figure 6.12.

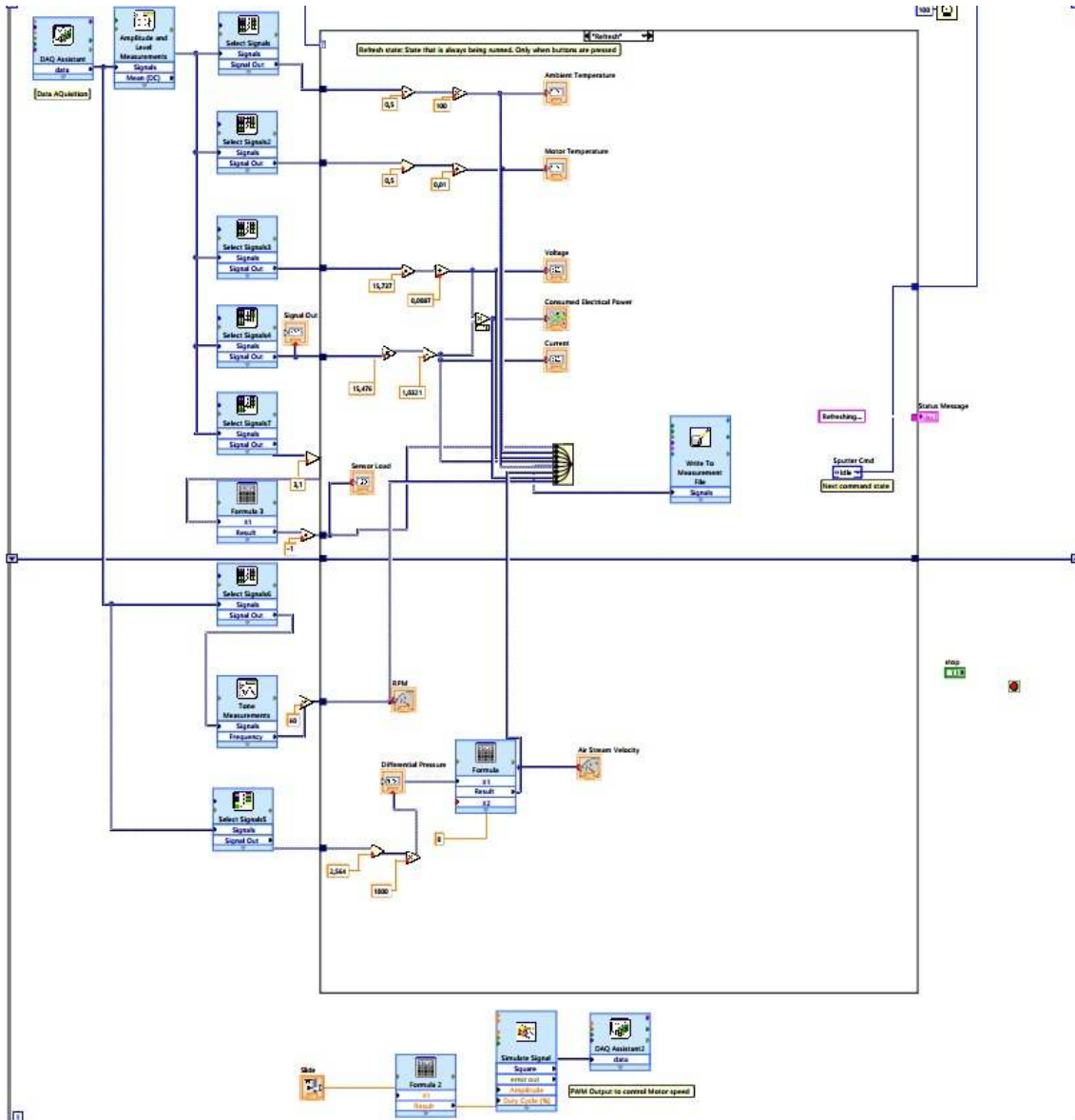


Figure 6.11: Labview block arrangement

Time	Time*	Load_Cell (Formula Result)	Motor_Temp (DC Voltage)	Voltage (DC Voltage)	Current (DC Voltage)	Ambient_Temp (DC Voltage)	Air_Velocity (Formula Result)	Voltage (DC Voltage) 1	RPM (Detected Frequency)
29/04/2015 10:32:04.389 AM	0	0.064494443	24.50772888	12.95771663	-1.686206274	22.09981002	1.922902427	-21.8464009	3030.011499
29/04/2015 10:33:44.854 AM	0.0001	0.064193005	24.5033378	12.95885172	-1.693403431	21.94372867	2.252003028	-21.94541000	3216.072471
29/04/2015 10:33:45.854 AM	0.0002	0.064251102	24.54752852	12.95922753	-1.679806926	21.89631859	2.126845633	-21.76900016	2990.135044
29/04/2015 10:33:45.294 AM	0.0003	0.064302238	24.55495228	12.95978878	-1.679387830	22.00940897	2.427076706	-21.70767208	3012.836493
29/04/2015 10:33:45.454 AM	0.0004	0.064248346	24.55339568	12.95807366	-1.677769663	21.93227283	2.538306317	-21.74101664	3035.659449
29/04/2015 10:33:45.854 AM	0.0005	0.064245733	24.54509581	12.95883429	-1.678133027	22.00537867	2.126845633	-21.75035346	2835.802113
29/04/2015 10:33:45.854 AM	0.0006	0.064271219	24.52020216	12.95798892	-1.679206221	21.93287971	2.538306317	-21.73943828	2819.524777
29/04/2015 10:33:45.854 AM	0.0007	0.064301577	24.44786825	12.95920160	-1.678453381	21.94404035	2.31204245	-21.75141385	2832.068608
29/04/2015 10:33:45.254 AM	0.0008	0.064320335	24.50064164	12.95820204	-1.678985329	21.96309499	2.843548271	-21.75325111	2920.262530
29/04/2015 10:33:45.454 AM	0.0009	0.064323717	24.54034484	12.95781494	-1.677773221	21.95407997	3.172423848	-21.74023288	2990.538744
29/04/2015 10:33:45.854 AM	0.001	0.064330413	24.49100778	12.95910853	-1.678390549	21.94165773	3.412959001	-21.74914936	3092.780427
29/04/2015 10:33:45.854 AM	0.0011	0.064333961	24.56857172	12.95885757	-1.677155811	22.00393195	3.372541848	-21.73355031	3115.001196
29/04/2015 10:33:47.054 AM	0.0012	0.064310109	24.50386388	12.95888840	-1.678886082	21.93800755	3.492254444	-21.75054444	2904.987682
29/04/2015 10:33:47.254 AM	0.0013	0.064405006	24.55190156	12.95798357	-1.677903627	21.948684747	3.162896242	-21.74225573	3081.36738
29/04/2015 10:33:47.454 AM	0.0014	0.064229527	24.55266668	12.95857557	-1.678875728	21.98100835	2.984505080	-21.75583759	3042.073969
29/04/2015 10:33:47.854 AM	0.0015	0.064390797	24.48291484	12.95897917	-1.676004628	21.96394987	3.119797387	-21.72729737	3080.945256
29/04/2015 10:33:47.854 AM	0.0016	0.064437959	24.52304658	12.95968735	-1.677140545	21.93794627	3.591457801	-21.73516357	3179.948291
29/04/2015 10:33:48.854 AM	0.0017	0.064335844	24.58040852	12.95897051	-1.675954238	21.94540555	2.745402117	-21.77004696	3084.086421
29/04/2015 10:33:48.254 AM	0.0018	0.064352135	24.46889024	12.95904284	-1.677490741	21.93481018	3.248379905	-21.78003113	3121.768930
29/04/2015 10:33:48.454 AM	0.0019	0.064454573	24.53697404	12.958372	-1.676957063	21.89914339	3.075041463	-21.72555082	3251.518648
29/04/2015 10:33:48.854 AM	0.002	0.064437059	24.48526516	12.95988298	-1.675105917	21.92893267	2.938234923	-21.70972828	1248.993967
29/04/2015 10:33:48.854 AM	0.0021	0.064445051	24.48922738	12.96018822	-1.677211784	21.98308663	2.784849753	-21.78080504	2028.040172
29/04/2015 10:33:49.854 AM	0.0022	0.06443045	24.47959644	12.95856522	-1.676372318	21.92076827	2.538036817	-21.72337823	3050.591977
29/04/2015 10:33:49.254 AM	0.0023	0.064477704	24.46962236	12.95842208	-1.678025241	21.93130093	2.483466979	-21.75426442	2822.189802
29/04/2015 10:33:49.454 AM	0.0024	0.064378892	24.45738652	12.95815238	-1.674972839	21.91933171	2.845482771	-21.70548611	3035.855111

Figure 6.12: Example of data recorded

# Chapter 7

## Test Rig Testing

After the assembly of all structural components of the test rig, and mounted and connected all sensors, it becomes necessary to test the test rig. Due to the fact that some discrepancies can occur during the manufacture of sensor, and to understand how accurate they can be, all used sensors were calibrated whenever possible.

### 7.1 Sensor Calibration

#### 7.1.1 Load Cell Sensor

To achieve a more correct measure for the load, due to the importance of this sensor, it was mounted a temporary structure near the test rig to calibrate it, illustrated in figure 7.2. For this, known weights were used to generate the linear regression to apply for the load cell. It was mounted a sheave in front of the motor and attached a hire to it. The wire should be perfectly straight from the motor and the sheave in order to have a more accurate calibration. Then the load cell was mounted in the position where the relation  $\frac{D_1}{D_2}$  was unity. Without any weight, the load cell was zeroed by applying an offset in the LabView software where the measurement of all the sensors happens. Then five known weights were applied and then the values of the Load Cell Generate were registered. After, it was generated a linear regression that was applied to the sensor. The plot that generated the calibration is shown in figure 7.1.

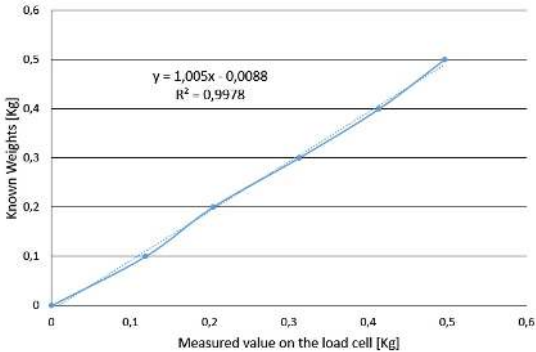


Figure 7.1: Load cell calibration and linear regression result.



Figure 7.2: Structure used for the calibration of the load cell

### 7.1.2 Voltage and Current Sensor

Both PitLab 36 V 75 A electrical sensors were calibrated using an available professional grade multimeter. To calibrate these sensors, two tests were executed. The first, aimed to calibrate the voltage sensor, was done by connecting both the sensor and the multimeter to a variable power supply, that could go from 12 V up to 30 V. Then the voltage was increased by 1 V, from 12 V to 30 V, and the readings from the multimeter and sensor were recorded. The readings from the sensor had some interference, so the reading was done by collecting 20 samples at 20 Hz and running it through a filter that averaged those samples, displaying that average in a numeric readout, as well as in a chart, and recording it in a file. For the calculations, four averages were used. Screenshots of the developed LabView program are displayed on figure 7.3.

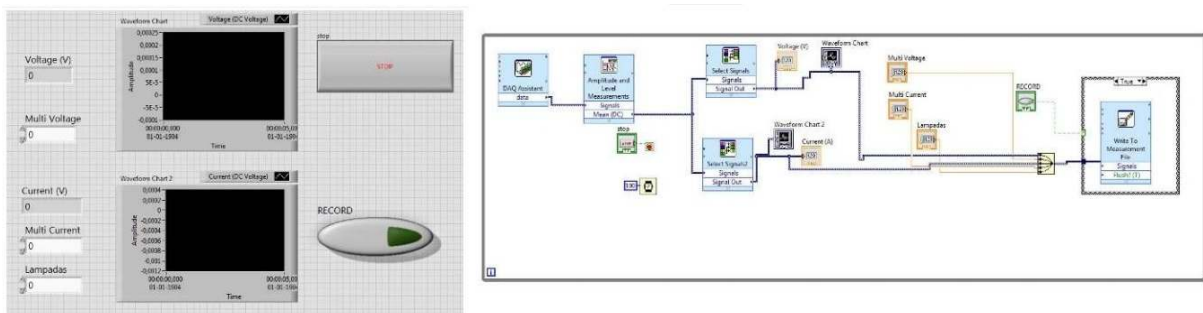


Figure 7.3: Screenshots of the developed LabView program for voltage/current sensor calibration

The program enabled to manually enter, the value or current value read in the multimeter, so that the readings from the sensor and the multimeter were written together in the same data file. To limit the size of the data file, a record button was added to allow the control of only writing the desired data. After obtaining the data, it was plotted and a linear regression was used to obtain the calibration formula

for the sensor. The results can be seen in figure 7.4. The current calibration was done using 12 V 21 W automotive light bulbs. Considering high power rated resistors are difficult to acquire as well as expensive, this was considered the best option, enabling low and high currents by changing the electrical system connected to the power supply. The data acquisition program was the same as the previous test, as the program was made with both tests in mind. The data treatment was also done similarly to the voltage calibration.

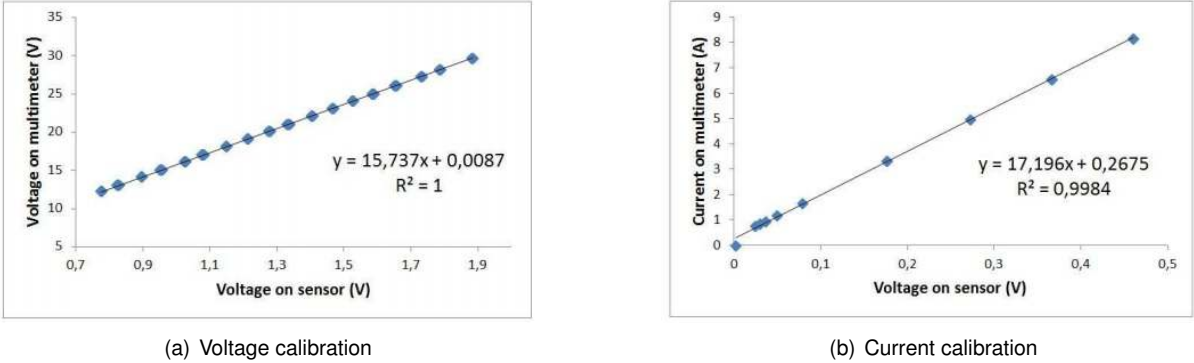


Figure 7.4: Voltage and current calibration test of the sensors.

The information from the manufacturer stated that these sensors had a voltage divider of 16:1 and a voltage to current conversion of 15.39 A measured (AM) per V output (VO). As can be seen in the previous results, figure 7.4 a), for this sensor the conversion factor for the voltage was 15.737 measured V per output V (VM/VO) with a zero offset of 0.0087 V, with a approximation factor of 100%. This result is very close to the manufacturer information. For the current sensor, the factory information was less accurate. As it can be seen in figure 7.4 b), the conversion factor is 17.196 AM/VO, quite far from the 15.39 AM/VO of the manufacturer, and an offset of 0.2675 A, which means that low current measure is not accurate enough to be considered valid. The approximation factor of the current linear regression is 99.84%, which is quite good. Both approximation factors are good, which means that the behaviour of the sensor is approximately linear. The second sensor has a voltage factor of 15.753VM/VO and an offset of 0.0162V, with an approximation factor of 100%, and has a current factor of 17.245AM/VO with and offset of 0.522A and an approximation factor of 99.7%.

### 7.1.3 Air Stream Velocity Sensor

The Pitot tube installed in the test rig was calibrated according to a Pitot tube that was already installed in the wind tunnel and correctly calibrated. It was provided the relation between the frequency of the electrical motor that drives the wind tunnel fan and the true airspeed inside the tunnel. This information is shown in figure 7.5.

After this, the procedure done for calibrating this sensor was similar to the one performed for the load cell. First the sensor was reset so it can measure zero, and then a linear regression was applied based on the values presented in figure 7.5. Six measurements were done through the tests and the speed measured by the sensor was compared to the true value. The linear regression obtained is shown in

figure 7.6.

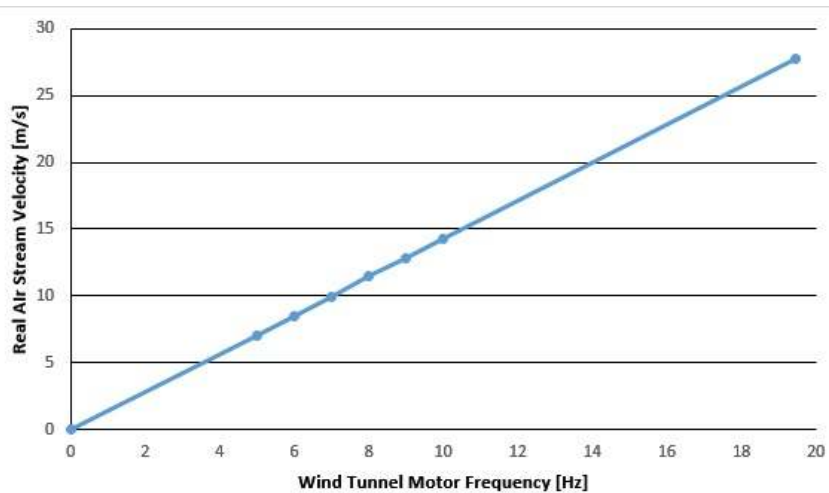


Figure 7.5: Relation of wind tunnel motor frequency with the true wind airspeed

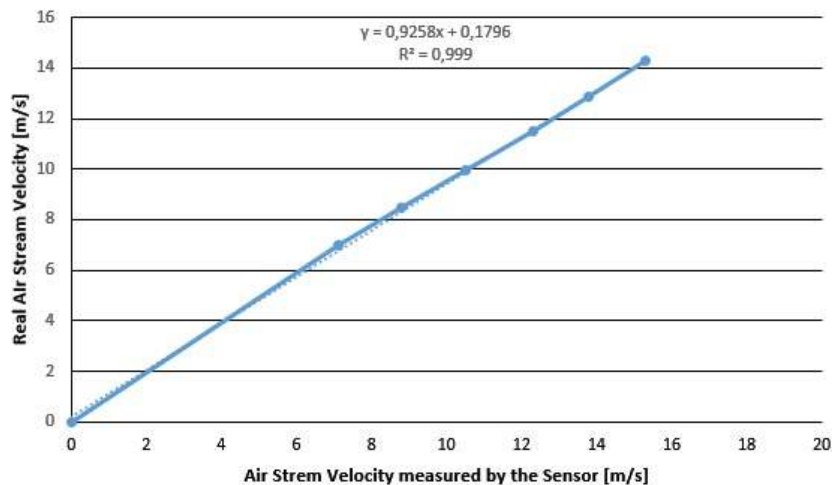


Figure 7.6: Linear regression applied to the airspeed sensor

## 7.2 Static Test

For testing the test rig, due to the lack of time for testing more than one motor and propeller, it was decided to test the motor AXI 2826/10[30] assembled with an APC 14x7E[28] propeller. The static test was performed using only one run. The test rig was turned on and the throttle set at 10%. Then it was increased with 5% steps until reaching 85%. The results are shown above in figures 7.7 and 7.8.

For this type of motor during this test run it was consumed a maximum electrical power of 472W. This value was computed through the maximum current and voltage consumed during the test run. For the thrust generated, the maximum value registered was 0.028, producing a maximum thrust load of 2.465 Kg.f at 7100 RPM. To check the operability of the test rig, it becomes necessary to establish some reference to compare the results generated. For the propeller manufacturer APC[28], consulting

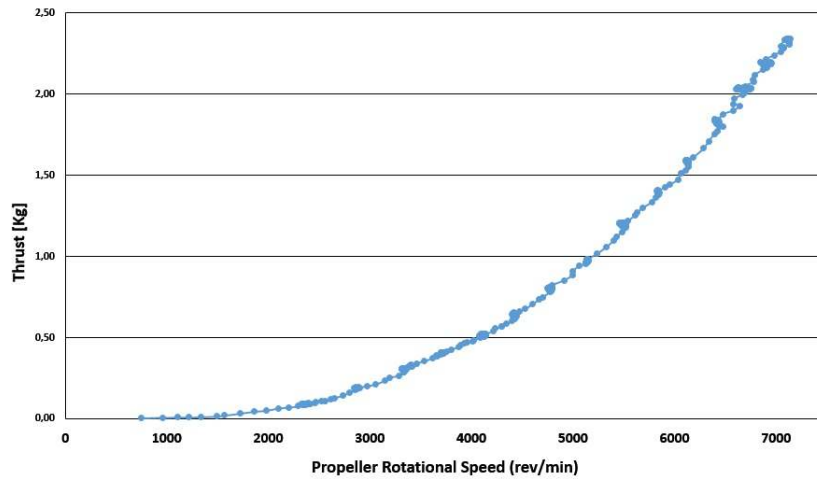


Figure 7.7: Thrust versus rev/min for the APC 14x7E propeller

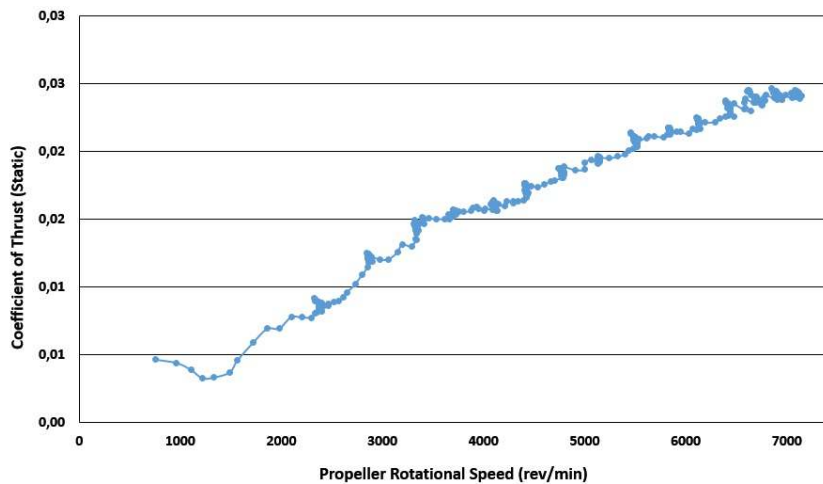


Figure 7.8: Thrust coefficient versus rev/min for the APC 14x7E propeller

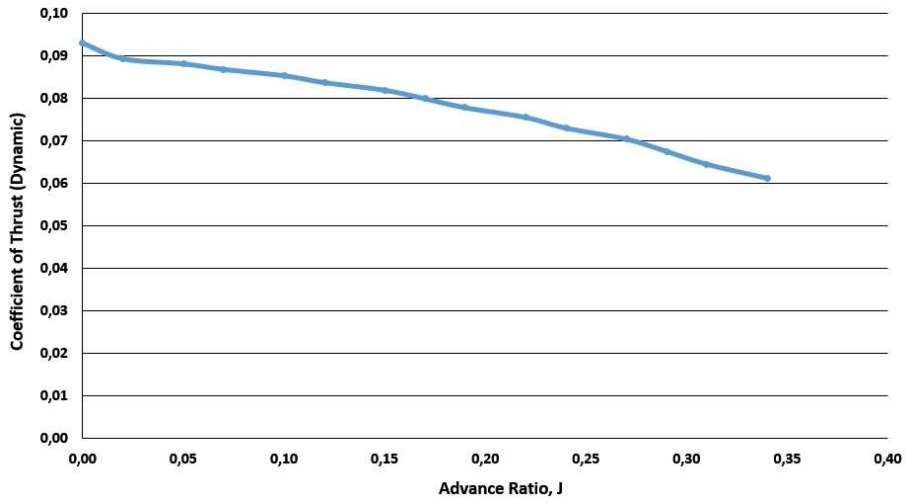
their performance data for the selected propeller, at 7000 RPM the nominal thrust produced is 2.54 Kg.f producing 0.036 to teh coefficient of thrust. Thus, with this results, it is clear that it is possible to validate the test run performed as well the operability of the test rig.

### 7.3 Dynamic Test

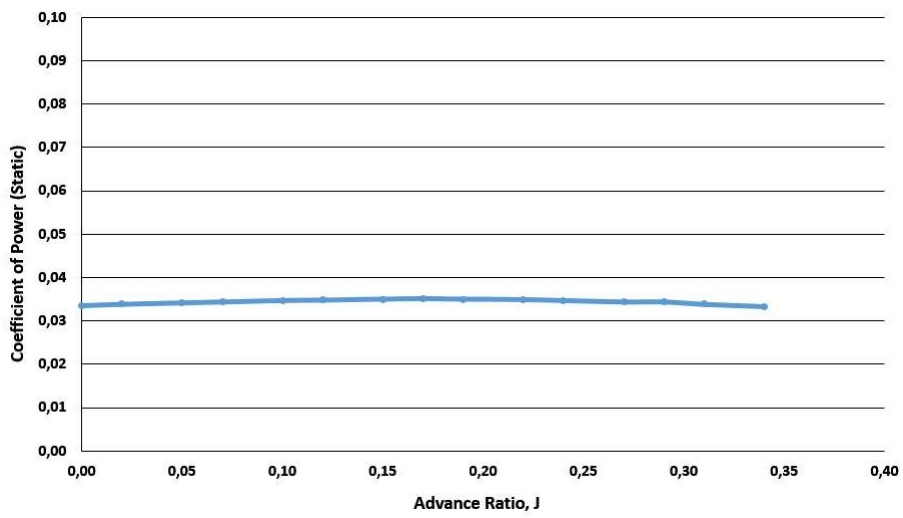
For the dynamic test, three tests were performed at different RPM. Each test consists in starting the motor and maintain it at a certain RPM and increasing the air stream velocity until the thrust generated by the system is null. This test was performed for a rotation of 3000, 5000 and 7000 RPM. The results are described in figures 7.9, 7.10 and 7.11. Similar to the static tests, the values generated were compared with the values given by the propeller manufacturer APC[28]. For N=3000 rev/min, the propeller generated a coefficient of thrust, power and efficiency of 0.061, 0.033 and 0.0625 respectively. For N=5000 rev/min, the propeller generated a coefficient of thrust, power and efficiency of 0.0805, 0.0385 and 0.045 respectively. For N=7000 rev/min, the propeller generated a coefficient of thrust, power and efficiency of 0.08, 0.041 and 0.0425 respectively. As it is possible to see in all three figure, the plots were not



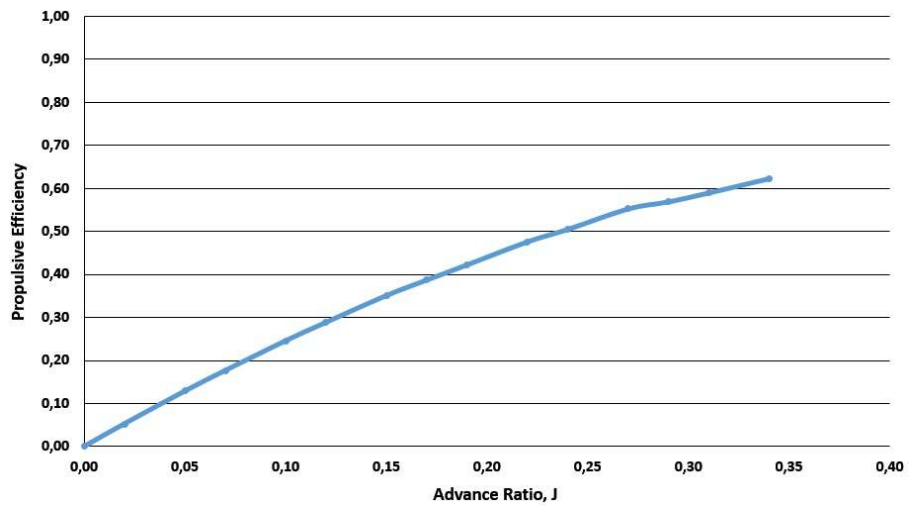
constant during all the test runs. This was caused by some interferences that lead to perturbations on the recorded data. This perturbations could be caused by the wind tunnel, or even to the power supply of the motor.



(a) Coefficient of Thrust versus Advance Ratio

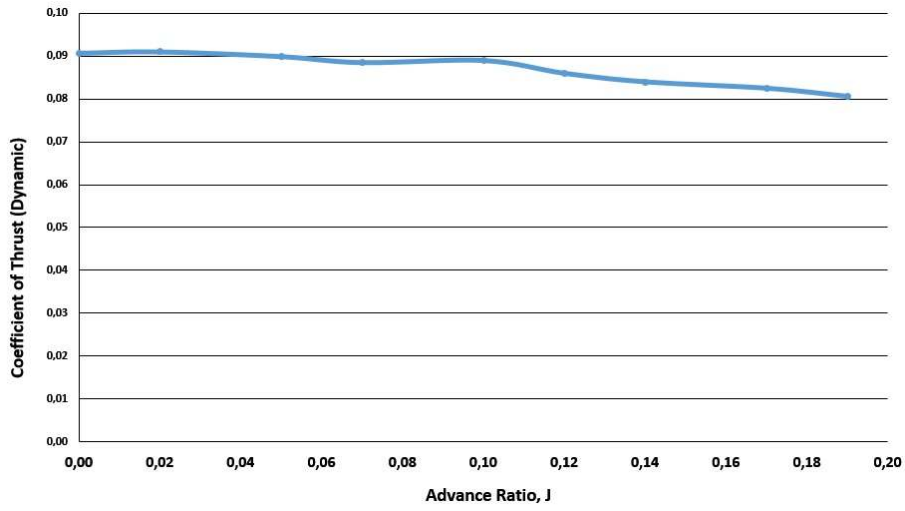


(b) Coefficient of Power versus Advance Ratio

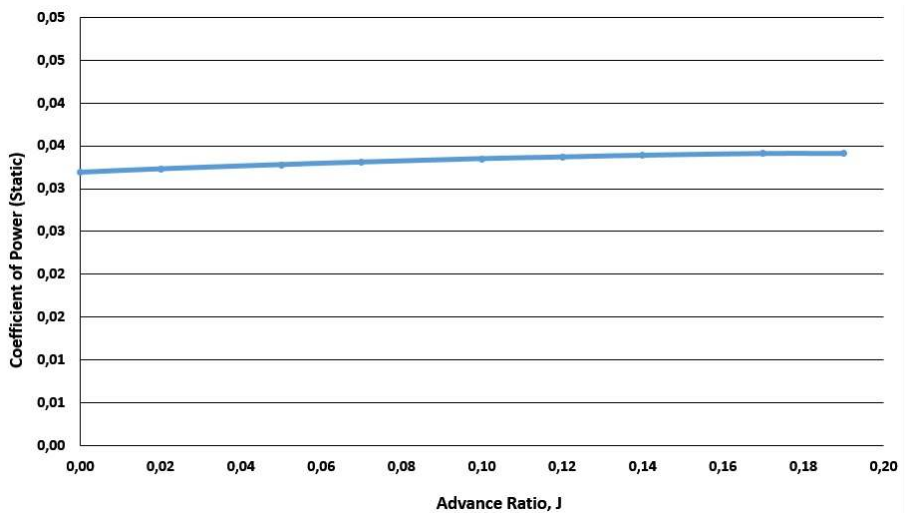


(c) Propulsive Efficiency versus Advance Ratio

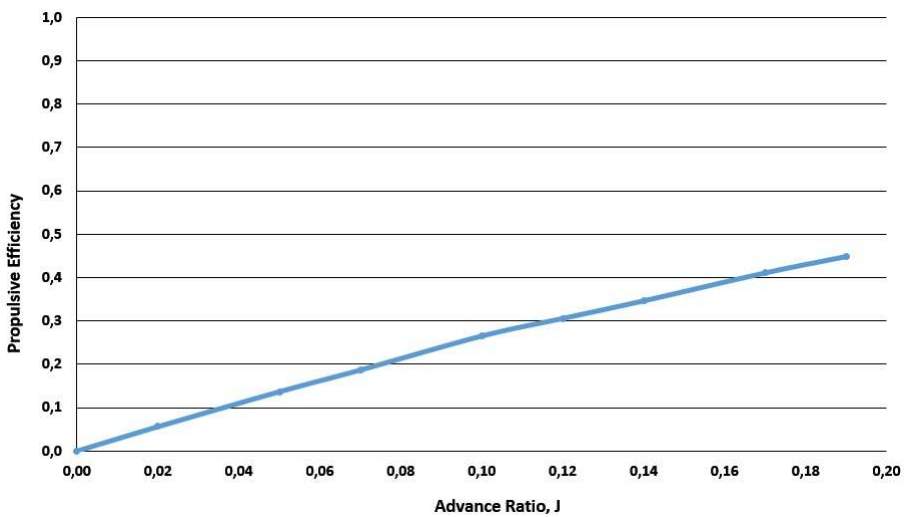
Figure 7.9: Motor at N=3000 rev/min for the APC 14x7E propeller



(a) Coefficient of Thrust versus Advance Ratio

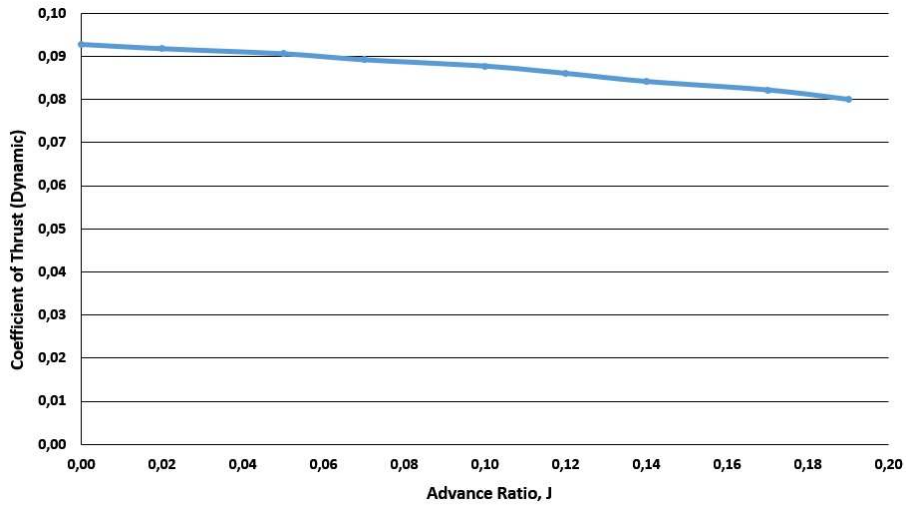


(b) Coefficient of Power versus Advance Ratio

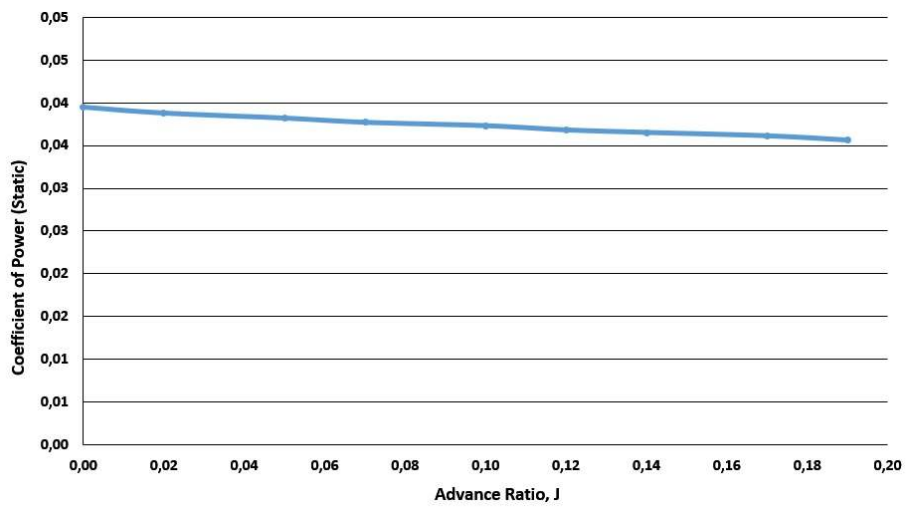


(c) Propulsive Efficiency versus Advance Ratio

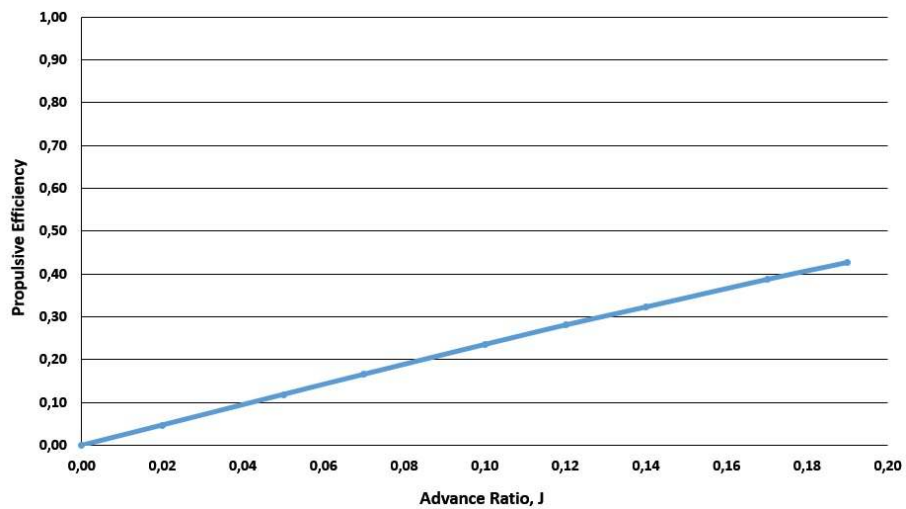
Figure 7.10: Motor at N=5000 rev/min for the APC 14x7E propeller



(a) Coefficient of Thrust versus Advance Ratio



(b) Coefficient of Power versus Advance Ratio



(c) Propulsive Efficiency versus Advance Ratio

Figure 7.11: Motor at N=7000 rev/min for the APC 14x7E propeller

# Chapter 8

## Conclusions

### 8.1 Achievements

The main goal of this thesis was the electro- mechanical project, construction and validation of a system that could allow the testing of an electric propulsion system to be used in UAVs. This system can be fitted in the LEEUAV Project. Of course, the propulsive system tested in the test rig can be applied to other UAV of bigger dimensions and higher electrical energy demand since the control is generic for any system and the type of test rig allows several different configurations of motor and propellers. The main outputs for this project were:

- The research made revealed that similar projects have lack of flexibility in terms of range of propellers and motors;
- Design, development and construction of a flexible structure that allows the test of several different ranges of propellers and brushless motors;
- Implementation of a graphical user interface based on the software LabView that allows the user of this test rig to have the reading and record of the output produced by the propulsive system;
- During the dynamic tests, the load produced by the wind generates a load that can seriously compromise the thrust produced. However, the higher the air stream velocity passing through the blade of the propeller, the higher the propulsive efficiency
- Also, during the dynamic tests it was possible to see that the lower the rotation is, higher is the propulsive efficiency. Mainly because of the less drag produced by the airflow passing through the propeller;

### 8.2 Future Work

This project still has several features that can be improved. A better graphical user interface system can be introduced where the user after performing the static and dynamic tests can see the output plots

corresponding to the propulsive system. Also a better data analysis can be introduced since the output data generated by the program contains a large size of information per each variable measured.

Also, since the amount of torque generated by this type of propulsive engine is high, a torque measuring system can be also introduced in the test rig.

Referring to the sensors used, it can be installed a more precise and stable sensor for measuring the air speed since it was the measure that gave more unprecise and unstable values comparing to the real values. Alternatively, different data filtering techniques can also be applied.

# Bibliography

- [1] A. C. Marta and P. Gamboa. Long endurance electric uav for civilian surveillance missions. *29th Congress of the International Council of Aeronautic Sciences, St. Petersburg*, September 2014.
- [2] Celebrating a century of flight. *NASA - National Aeronautics and Space Administration*, 2003. ISBN: 0-16-067541-3.
- [3] Robert Graves. *Greek Myths: Illustrated Edition*. Penguin Group, 1955.
- [4] David W Wragg. *Flight before flying*. Osprey, 1974.
- [5] Arthur E Popham. *The drawings of Leonardo Da Vinci*. Jonathan Cape, 1971.
- [6] Daniel Arasse. *Leonardo Da Vinci*. Konecky and Konecky, 2005.
- [7] Carvalho. *História dos Balões*. Relógio d'Água, 1991.
- [8] Charles Gillispie. *The Montgolfier Brothers and the Invention of Aviation*. Princeton University Press, 1992.
- [9] Gibbs-Smith Charles. *Sir George Cayley Father of Aerial Navigation*. Royal Society of London, 1962.
- [10] First powered flight. <http://airandspace.si.edu/exhibitions/wright-brothers/online/>, 2014.
- [11] NASA National Aeronautics and Space Administration. <http://www.nasa.gov/sites/default/files/images/206311main-wright-brothers-full.jpg>, 2012.
- [12] Konstantinos Dalamagkidis, Kimon P. Valavanis, and Dr. Les A. Piegl. *On Integrating Unmanned Aircraft Systems into the National Airspace System*. Springer Netherlands, 2012.
- [13] S.J.Zaloga. *Unmanned Aerial Vehicles: Robotic Air Warfare 1917–2007*. Osprey Publishing Ltd., 2008.
- [14] Newcome L. *Unmanned Aviation: A brief history of UAV's*. American Institute of Aeronautics and Astronautics, 2004.
- [15] Tekever. <http://www.tekever.com>. Lisbon, Portugal.
- [16] J. Borges de Sousa, G. Gonçalves, A. Costa, and J. Morgado. Mixed initiative control of unmanned air vehicle systems: the pitvant r and d uav program. 2012.

- [17] UAVision. <http://www.uavision.com>. Lisbon, Portugal.
- [18] Spin.Works. <http://www.spinworks.pt>. Lisbon, Portugal.
- [19] Jeremiah Gertler. U.s. unmanned aerial systems. *Federation of American Scientists website*, 2013.
- [20] Jason Gilbert. Tacocopter aims to deliver tacos using unmanned drone helicopters. *The Huffington Post*, 2012.
- [21] Kevin Robillard and Alex Byers. Amazon drones: Obstacles to the bezos dream. *Politico*, 2013.
- [22] E-commerce giant amazon seeks faa nod for testing drones. *Seattle Bulletin*, 2014.
- [23] S. K. Ojha. *Flight Performance of Aircraft*. Ed. Bombay, India: AIAA, 1st edition, 1995.
- [24] A. Emadi. *Handbook of automotive power electronics and motor drives*. United States of America: CRC Press, 2005.
- [25] W. H. Yeadon. *Handbook of small electric motors*. United States of America: McGraw-Hill, 2001.
- [26] Ward Brown. Brushless dc motor control made easy. 2002.
- [27] Concha Reid, Michelle Manzo, and Michael J. Logan. Performance characterization of a lithium-ion gel polymer battery power supply system for an unmanned aerial vehicle. *Power Systems Conference*, 2004.
- [28] APC Advance Precision Composites. <http://www.apcprop.com/>. Woodland, CA, USA.
- [29] AXI Model Motors. <http://www.hyperion-eu.com/>. Hvidovre, Denmark.
- [30] AXI Model Motors. <http://www.modelmotors.cz>. Pardubice, Czech Republic.
- [31] W. B. Garner. Model airplanes propellers. March 2009.
- [32] Turnigity Power Systems.
- [33] Ramada Aços e Indústrias SA. <http://www.ramada.pt/>. Ovar, Portugal.
- [34] UIUC Applied Aerodynamics Group. <http://m-selig.ae.illinois.edu/ads.html>. Illinois, USA.
- [35] XFOIL MIT. <http://web.mit.edu/drela/Public/web/xfoil/>. Massachusetts, USA.
- [36] Vishay Intertechnology Inc. <http://www.vishay.com/>. Selb, Germany.
- [37] PitLab innovative electronics. <http://www.pitlab.com/>. Warsaw, Poland.
- [38] Analog Devices. <http://www.analog.com/>. Massachusetts, USA.
- [39] National Instruments. <http://www.ni.com/>. Texas, USA.



# Appendix A

## LiPo cells duration

Propeller	Mechanical Power	Electrical Power	LiPo Cells	Voltage	Current	Time (min)
9x6E	0,50	0,63	3	11,1	56,3	5,33
10x6E	0,73	0,91	3	11,1	82,2	3,65
11x7E	1,03	1,29	4	14,8	86,9	3,45
12x6E	1,08	1,35	4	14,8	91,2	3,29
13x8E	1,20	1,50	4	14,8	101,3	2,96
14x85E	1,85	2,31	5	18,5	125,0	2,40
15x10E	2,26	2,83	5	18,5	152,7	1,96
16x10E	3,27	4,09	5	18,5	220,9	1,36
17x10E	3,92	4,90	6	22,2	220,7	1,36
18x10E	3,89	4,86	6	22,2	219,0	1,37
19x10E	3,74	4,68	8	29,6	157,9	1,90
20x10E	2,89	3,61	8	29,6	122,0	2,46
21x13E	4,02	5,03	8	29,6	169,7	1,77
22x10E	3,24	4,05	10	37	109,4	2,74
24x12E	3,35	4,19	10	37	113,1	2,65
25x125E	4,19	5,24	10	37	141,5	2,12
26x13E	4,99	6,24	10	37	168,5	1,78
27x13E	6,03	7,54	10	37	203,7	1,47

Table A.1: Values used to plot the LiPo cells usage

## Appendix B

# Technical Datasheets

The following datasheets are included in this appendix:

- Vishay S-Type Load Cell, Model STC
- Strain Gauge Amplifier BA660
- Reflective Optical Sensor with Transistor Output, CNY70
- Low Voltage Temperature Sensor TMP36GZ
- MPXV7002 Pressure Sensor
- Y-bearing flanged unit FYTB 17 TF
- Y-bearing plummer block unit SY 17 TF

## S-Type Load Cell

### FEATURES

- Capacities:  
Aluminum construction—1, 2, 5, 10, 20 kg;  
Alloy Steel construction— 25 to 5000 kg, 250 to 40k lbs
- Bi-direction (tension/compression)
- Rationalized output
- NTEP Class III 5000S, III L10000 approval from 250 lbs to 20k lbs
- **Optional**
  - Stainless steel available
  - FM approval available



### APPLICATIONS

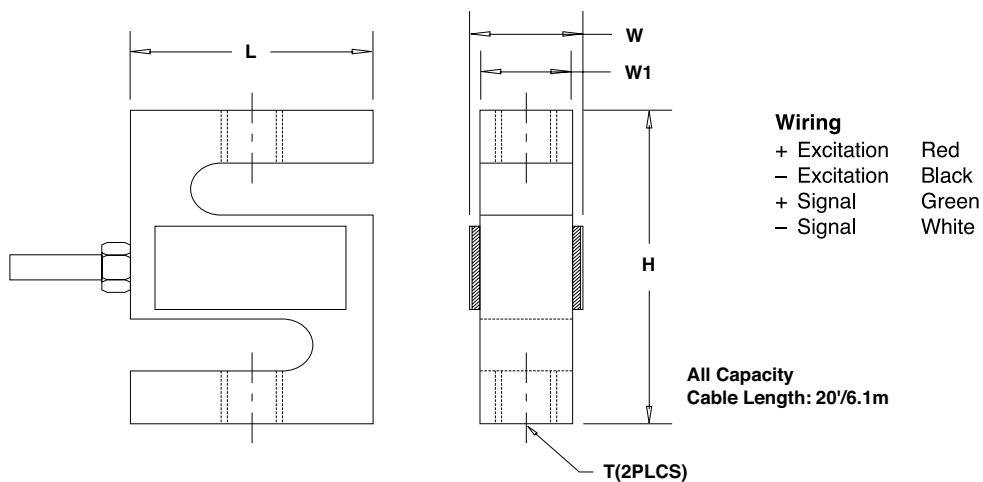
- Electro-mechanical conversion scales
- Silo/hopper/tank weighing
- Crane scales
- Fork-lift scales
- Dosing/filling
- Universal material tester
- Tensile/pulling force measurement

### DESCRIPTION

The S-type load cell, as the name indicates, can be easily identified by S-shaped body. They can be loaded either in tension or compression, and used for single or multiple-cell application if the output is rationalized.

STC is made of Aluminum, Alloy Steel or Stainless Steel, sealed to IP67 providing excellent protection against moisture and humidity.

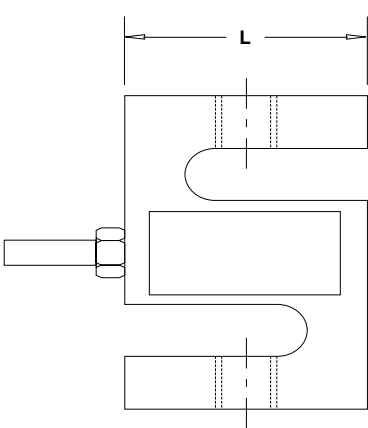
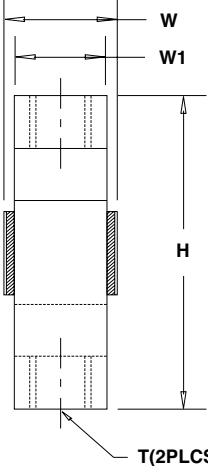
### OUTLINE DIMENSIONS—ALUMINUM in inches [millimeters]



CAPACITY		L	W	W <sub>1</sub>	H	T
1 / 2 / 5 / 10 / 20 kg	mm	50.8	16.6	16.6	63.5	M6 x 1.0
	(inch)	0.65	1.05	0.65	2.50	

Outline dimension for Alloy Steel supplied on next page

## S-Type Load Cell

OUTLINE DIMENSIONS—ALLOY STEEL in inches [millimeters]						
						<p><b>Wiring</b></p> <ul style="list-style-type: none"> <li>+ Excitation    Red</li> <li>- Excitation    Black</li> <li>+ Signal        Green</li> <li>- Signal        White</li> </ul>
<b>All Capacity Cable Length: 20'/6.1m</b>						
CAPACITY		L	W	W <sub>1</sub>	H	T
25 / 50 / 75 kg	mm	50.8	26.7	12.7	63.5	M6 x 1.0
	(inch)	2.00	1.05	0.50	2.50	
100 / 150 kg	mm	50.8	22.92	19.1	76.2	M10 x 1.5
	(inch)	2.00	0.9	0.75	3.00	
250 / 300 lbs	mm	50.8	26.7	12.7	76.2	3/8-24UNF
	(inch)	2.00	1.05	0.50	3.00	
250 kg 500 / 750 lbs	mm	50.8	30.4	19.1	76.2	M12 x 1.75
	(inch)	2.00	1.2	0.75	3.00	
500 / 750 kg	mm	50.8	25.4	19.1	76.2	M12 x 1.75
	(inch)	2.00	1.00	0.75	3.00	
1k / 1.5k lbs	mm	50.8	26.1	19.1	76.2	1/2-20UNF
	(inch)	2.00	1.03	0.75	3.00	
1000 / 1500 kg 2k / 2.5k / 3k lbs	mm	50.8	31.8	25.4	76.2	M12 x 1.75
	(inch)	2.00	1.25	1.00	3.00	
5k / 7.5k lbs	mm	76.2	31.8	25.4	107.9	3/4-16UNF
	(inch)	3.00	1.25	1.00	4.25	
2000 / 2500 / 5000 kg	mm	76.2	38.1	31.8	100.4	M20 x 1.5
	(inch)	3.00	1.50	1.25	3.95	
10k lbs	mm	88.9	31.8	25.4	120.7	3/4-16UNF
	(inch)	3.50	1.25	1.00	4.75	
15k lbs	mm	101.6	38.1	31.8	139.7	1-14UNS
	(inch)	4	1.50	1.25	5.50	
20k lbs	mm	127	55.7	50.8	177.8	1 1/4-12UNF
	(inch)	5	2.19	2	7.00	
40k lbs	mm	152.4	69.9	63.5	254.0	1 1/2-12UNF
	(inch)	6.00	2.75	2.50	10.00	

## S-Type Load Cell

SPECIFICATIONS			
PARAMETER	VALUE		UNIT
NTEP/OIML accuracy class	NTEP III & IIIL	Non-Approved	
Maximum no. of intervals (n)	III 5000 single* IIIL10000 single*	2000	
$Y = E_{max}/V_{min}$	10000	5000	Maximum available
Standard capacities ( $E_{max}$ ) (Aluminum)	1, 2, 5, 10, 20		kg
Standard capacities ( $E_{max}$ ) (Steel)	25, 50, 75, 100, 250, 500, 750, 1000, 1500, 2000, 2500, 5000		kg
	250, 300, 500, 750, 1k, 1.5k, 2k, 2.5k, 3k, 5k, 7.5k, 10k, 15k, 20k, 40k		lbs
Rated output—R.O. (Aluminum)	2.0		mV/V
Rated output—R.O. (Steel)	3.0		mV/V
Rated output tolerance	0.25		±% of rated output
Zero balance	1		±% of rated output
Non-linearity	0.020	0.020 (SS: 0.05)	±% of rated output
Hysteresis	0.020	0.020 (SS: 0.05)	±% of rated output
Non-repeatability	0.020		±% of rated output
Creep error (20 minutes)	0.030		±% of rated output
Zero return (20 minutes)	0.030		±% of rated output
Temperature effect on min. dead load output	0.0015	0.0026	±% of rated output/°C
Temperature effect on sensitivity	0.0010	0.0015	±% of applied load/°C
Compensated temperature range	-10 to +40		°C
Operating temperature range	-20 to +60		°C
Safe overload	150		% of R.C.
Ultimate overload	200 (Aluminum) / 300 (Steel)		% of R.C.
Excitation, recommended	10		VDC or VAC RMS
Excitation, maximum	15		VDC or VAC RMS
Input impedance	410±5 (Aluminum) / 385±5 (Steel)		Ω
Output impedance	350±3		Ω
Insulation resistance	>5000		MΩ
Construction	Aluminium or Nickel-plated alloy steel **		
Environmental protection	IP67		

\* Capacities 250–20k lbs

\*\* Stainless steel available

All specifications subject to change without notice.

FM Approval

Intrinsically Safe: Class I, II, III; Div. 1 Groups A-G

Non-Incendive: Class I; Div. 2 Groups A-D

## Disclaimer

ALL PRODUCTS, PRODUCT SPECIFICATIONS AND DATA ARE SUBJECT TO CHANGE WITHOUT NOTICE.

Vishay Precision Group, Inc., its affiliates, agents, and employees, and all persons acting on its or their behalf (collectively, "Vishay Precision Group"), disclaim any and all liability for any errors, inaccuracies or incompleteness contained herein or in any other disclosure relating to any product.

The product specifications do not expand or otherwise modify Vishay Precision Group's terms and conditions of purchase, including but not limited to, the warranty expressed therein.

Vishay Precision Group makes no warranty, representation or guarantee other than as set forth in the terms and conditions of purchase. **To the maximum extent permitted by applicable law, Vishay Precision Group disclaims (i) any and all liability arising out of the application or use of any product, (ii) any and all liability, including without limitation special, consequential or incidental damages, and (iii) any and all implied warranties, including warranties of fitness for particular purpose, non-infringement and merchantability.**

Information provided in datasheets and/or specifications may vary from actual results in different applications and performance may vary over time. Statements regarding the suitability of products for certain types of applications are based on Vishay Precision Group's knowledge of typical requirements that are often placed on Vishay Precision Group products. It is the customer's responsibility to validate that a particular product with the properties described in the product specification is suitable for use in a particular application.

No license, express, implied, or otherwise, to any intellectual property rights is granted by this document, or by any conduct of Vishay Precision Group.

The products shown herein are not designed for use in life-saving or life-sustaining applications unless otherwise expressly indicated. Customers using or selling Vishay Precision Group products not expressly indicated for use in such applications do so entirely at their own risk and agree to fully indemnify Vishay Precision Group for any damages arising or resulting from such use or sale. Please contact authorized Vishay Precision Group personnel to obtain written terms and conditions regarding products designed for such applications.

Product names and markings noted herein may be trademarks of their respective owners.

# Strain Gauge Amplifier BA 660 With Auto-Zero Function

## Features

- Auto-zero any input signal up to 100% of full scale
- Zero trigger via external switch or via logic signal from PLC etc.
- Bi-directional measurement. Output voltage 0 to  $\pm 5V$  or optional 0 to  $\pm 10V$
- Input for full bridge Strain gauge  $\pm 2$  mV/V or optional 1 mV/V or  $\pm 3,5$  mV/V
- Connect via screw terminal

## Applications

- Strain measurement on machine parts with strain gauges directly applied to it
- Use with all strain gauge sensors, i.e. force measurement, strain measurement
- Automatization with zero tracking
- Whenever zero adjustment should be quick and easy to do

## Description

The BA660 is a miniature amplifier, designed to provide a signal conditioning for full bridge strain gauge sensors. A internal voltage reference supplies the excitation voltage for a sensor. The zero adjustment is performed by digital controller with a wide adjustment range of  $\pm 100\%$  of full scale. This allows zero-cycle to run the via an external trigger signal from a switch or a PLC.



The zero reading gets stored in a flash memory. It provides direct connectivity to a range of analog input devices as required: PLC, Analog PC cards, displays and many others. The zero adjustment cycle takes only 90ms. The trigger voltage can be anywhere between 5 volts to 30 volts. It is feasible to connect the Z input with the power voltage via a switch in order to trigger a zero cycle.

## Connection

Screw terminal Pin	
1	$-U_D$ : Input -
2	$+U_D$ : Input +
3	$+U_S$ : Excitation +
4	$-U_S$ : Excitation - (GND)
5	GND : Ground
6	$+U_A$ : Analog out
7	$+U_B$ : Power supply +12 to +24VDC
8	Z: Zero control input

**Specifications:**

		Unit
<b>Accuracy class</b>	0,1	
<b>Input range</b> (Input signal needed for full scale output)	±2 optional ±1 and ±3,5mV	mV/V
<b>Bridge resistance</b>	87 to 5000Ω (87Ω is equivalent to 4 x 350Ω parallel)	Ohm
<b>Bridge excitation</b>	5	V
<b>Input impedance</b>	>20 / 300pF	MΩ
<b>Linearity</b>	<0,02	% F.S.
<b>Temperature coefficient of zero</b>	<0,2 typ. 0,05	% F.S./10K
<b>Temperature coefficient of span</b>	< 0,1 typ. 0,05	% of reading /10K
<b>Bandwidth (-3dB)</b>	<b>250</b> ; optional 20, 2500, 10 000 (Standard bandwidth is 250 Hz)	Hz
<b>Resolution</b>	>20000 divisions (at 250Hz filter)	
<b>Analog output</b>		
Full scale	±5	V
Usable range	±10*	V
Output resistance	47	Ω
<b>Zero adjustment</b>		
Tolerance	<5, typical <2,5	mV
Adjustment time	<90	ms
<b>Zero control input</b>		
auto zero triggers at falling edge. High level must be present for a minimum of 4ms	Low: <1,4 High: >5 (max. 28V)	V V
<b>Power supply</b>		
Operating range	12 to 24	VDC
Usable range	10,5 to 28	VDC
<b>Power consumption</b>	35 mA, plus current into the full bridge	mA
<b>Stored values</b>	Last zero (stored in Flash memory)	
<b>Operating temperature</b>	-10...+65	°C
<b>Storage temperature</b>	-40...+85	°C
<b>Dimensions (l x w x h)</b>	40.5 x 30 x 12	mm

**Ordering examples**

**BA 660** (=Standard unit. Input 2mV/V, Filter 250Hz, Output 0 to ±5)

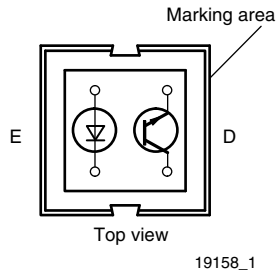
**BA 660-E1-F10kHz-A10** (=Input 1mV/V, Filter 10000Hz, Output 0 to ±10V)

**BA 660-E3,5** (=Input 3,5mV and Standard Filter 250Hz)

A version that is adjusting "Zero" to 2.5 volts or 5 volts can be supplied. This version is used together with some analog PC-card that cannot read negative input signals.



## Reflective Optical Sensor with Transistor Output



### FEATURES

- Package type: leaded
- Detector type: phototransistor
- Dimensions (L x W x H in mm): 7 x 7 x 6
- Peak operating distance: < 0.5 mm
- Operating range within > 20 % relative collector current: 0 mm to 5 mm
- Typical output current under test:  $I_C = 1$  mA
- Emitter wavelength: 950 nm
- Daylight blocking filter
- Lead (Pb)-free soldering released
- Material categorization: For definitions of compliance please see [www.vishay.com/doc?99912](http://www.vishay.com/doc?99912)


**RoHS**  
COMPLIANT

### DESCRIPTION

The CNY70 is a reflective sensor that includes an infrared emitter and phototransistor in a leaded package which blocks visible light.

### APPLICATIONS

- Optoelectronic scanning and switching devices i.e., index sensing, coded disk scanning etc. (optoelectronic encoder assemblies).

### PRODUCT SUMMARY

PART NUMBER	DISTANCE FOR MAXIMUM CTR <sub>rel</sub> (1) (mm)	DISTANCE RANGE FOR RELATIVE I <sub>out</sub> > 20 % (mm)	TYPICAL OUTPUT CURRENT UNDER TEST (2) (mA)	DAYLIGHT BLOCKING FILTER INTEGRATED
CNY70	0	0 to 5	1	Yes

#### Notes

- (1) CTR: current transference ratio,  $I_{out}/I_{in}$   
 (2) Conditions like in table basic characteristics/sensors

### ORDERING INFORMATION

ORDERING CODE	PACKAGING	VOLUME (1)	REMARKS
CNY70	Tube	MOQ: 4000 pcs, 80 pcs/tube	-

#### Note

- (1) MOQ: minimum order quantity

### ABSOLUTE MAXIMUM RATINGS (T<sub>amb</sub> = 25 °C, unless otherwise specified)

PARAMETER	TEST CONDITION	SYMBOL	VALUE	UNIT
<b>COUPLER</b>				
Total power dissipation	T <sub>amb</sub> ≤ 25 °C	P <sub>tot</sub>	200	mW
Ambient temperature range		T <sub>amb</sub>	- 40 to + 85	°C
Storage temperature range		T <sub>stg</sub>	- 40 to + 100	°C
Soldering temperature	Distance to case 2 mm, t ≤ 5 s	T <sub>sd</sub>	260	°C
<b>INPUT (EMITTER)</b>				
Reverse voltage		V <sub>R</sub>	5	V
Forward current		I <sub>F</sub>	50	mA
Forward surge current	t <sub>p</sub> ≤ 10 μs	I <sub>FSM</sub>	3	A
Power dissipation	T <sub>amb</sub> ≤ 25 °C	P <sub>V</sub>	100	mW
Junction temperature		T <sub>J</sub>	100	°C



ABSOLUTE MAXIMUM RATINGS ( $T_{amb} = 25\text{ }^{\circ}\text{C}$ , unless otherwise specified)				
PARAMETER	TEST CONDITION	SYMBOL	VALUE	UNIT
<b>OUTPUT (DETECTOR)</b>				
Collector emitter voltage		$V_{CEO}$	32	V
Emitter collector voltage		$V_{ECO}$	7	V
Collector current		$I_C$	50	mA
Power dissipation	$T_{amb} \leq 25\text{ }^{\circ}\text{C}$	$P_V$	100	mW
Junction temperature		$T_j$	100	$^{\circ}\text{C}$

**ABSOLUTE MAXIMUM RATINGS**

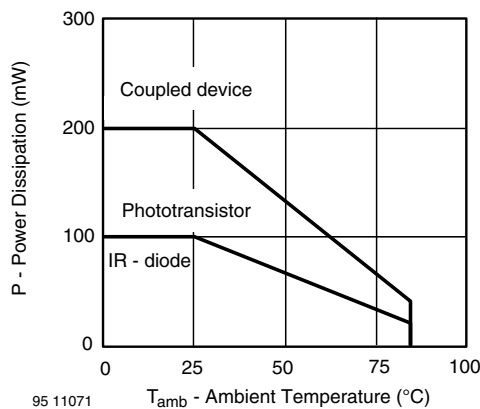


Fig. 1 - Power Dissipation vs. Ambient Temperature

BASIC CHARACTERISTICS ( $T_{amb} = 25\text{ }^{\circ}\text{C}$ , unless otherwise specified)						
PARAMETER	TEST CONDITION	SYMBOL	MIN.	TYP.	MAX.	UNIT
<b>COUPLER</b>						
Collector current	$V_{CE} = 5\text{ V}$ , $I_F = 20\text{ mA}$ , $d = 0.3\text{ mm}$ (figure 1)	$I_C^{(2)}$	0.3	1.0		mA
Cross talk current	$V_{CE} = 5\text{ V}$ , $I_F = 20\text{ mA}$ , (figure 2)	$I_{CX}^{(3)}$			600	nA
Collector emitter saturation voltage	$I_F = 20\text{ mA}$ , $I_C = 0.1\text{ mA}$ , $d = 0.3\text{ mm}$ (figure 1)	$V_{CEsat}^{(2)}$			0.3	V
<b>INPUT (EMITTER)</b>						
Forward voltage	$I_F = 50\text{ mA}$	$V_F$		1.25	1.6	V
Radiant intensity	$I_F = 50\text{ mA}$ , $t_p = 20\text{ ms}$	$I_e$			7.5	mW/sr
Peak wavelength	$I_F = 100\text{ mA}$	$\lambda_P$	940			nm
Virtual source diameter	Method: 63 % encircled energy	$d$		1.2		mm
<b>OUTPUT (DETECTOR)</b>						
Collector emitter voltage	$I_C = 1\text{ mA}$	$V_{CEO}$	32			V
Emitter collector voltage	$I_E = 100\text{ }\mu\text{A}$	$V_{ECO}$	5			V
Collector dark current	$V_{CE} = 20\text{ V}$ , $I_F = 0\text{ A}$ , $E = 0\text{ lx}$	$I_{CEO}$			200	nA

**Notes**

- (1) Measured with the "Kodak neutral test card", white side with 90 % diffuse reflectance
- (2) Measured without reflecting medium

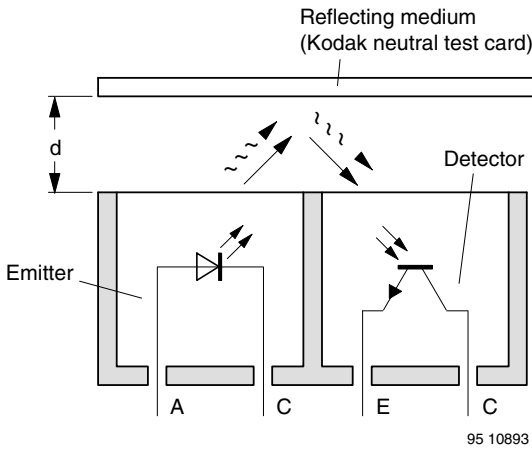


Fig. 2 - Test Condition

**BASIC CHARACTERISTICS** ( $T_{amb} = 25\text{ }^{\circ}\text{C}$ , unless otherwise specified)

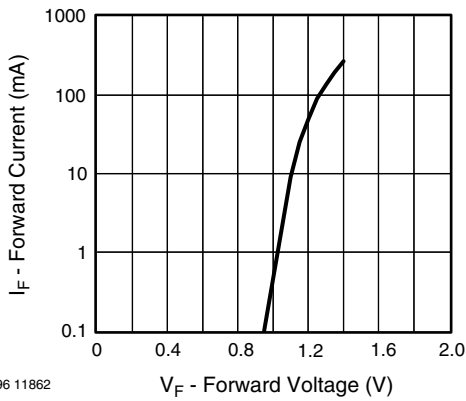


Fig. 3 - Forward Current vs. Forward Voltage

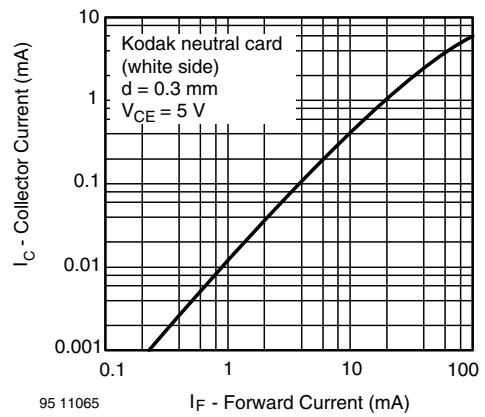


Fig. 5 - Collector Current vs. Forward Current

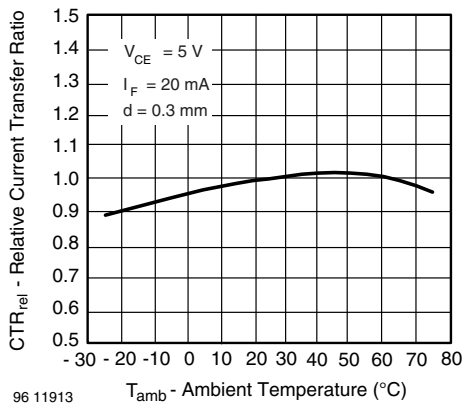


Fig. 4 - Relative Current Transfer Ratio vs. Ambient Temperature

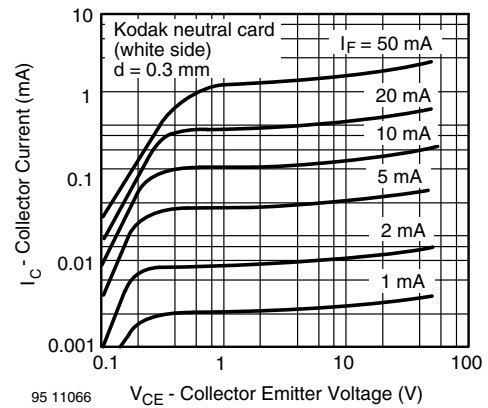


Fig. 6 - Collector Current vs. Collector Emitter Voltage

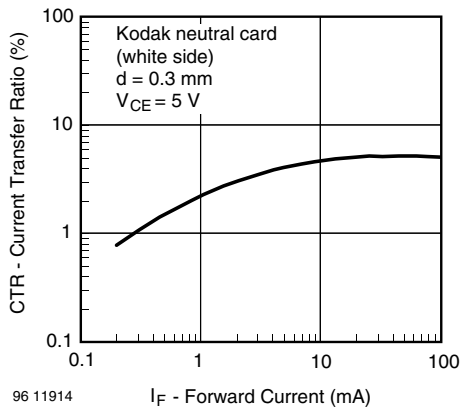


Fig. 7 - Current Transfer Ratio vs. Forward Current

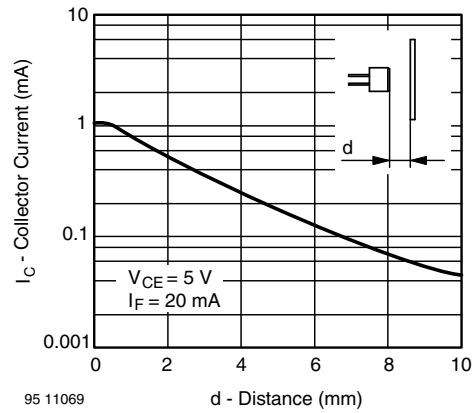


Fig. 9 - Collector Current vs. Distance

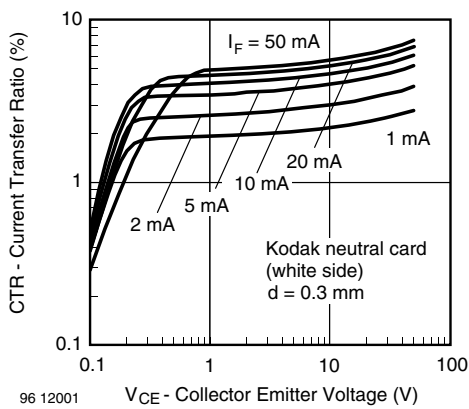


Fig. 8 - Current Transfer Ratio vs. Collector Emitter Voltage

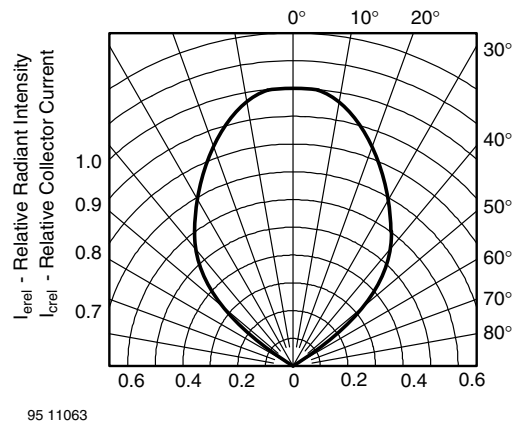


Fig. 10 - Relative Radiant Intensity/Collector Current vs. Angular Displacement

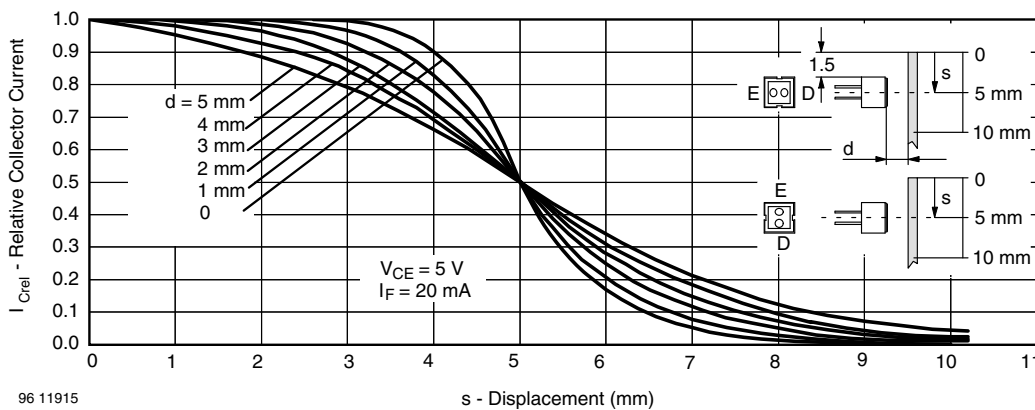


Fig. 11 - Relative Collector Current vs. Displacement

### FEATURES

- Low voltage operation (2.7 V to 5.5 V)
- Calibrated directly in °C
- 10 mV/°C scale factor (20 mV/°C on **TMP37**)
- ±2°C accuracy over temperature (typ)
- ±0.5°C linearity (typ)
- Stable with large capacitive loads
- Specified -40°C to +125°C, operation to +150°C
- Less than 50 µA quiescent current
- Shutdown current 0.5 µA max
- Low self-heating
- Qualified for automotive applications

### APPLICATIONS

- Environmental control systems
- Thermal protection
- Industrial process control
- Fire alarms
- Power system monitors
- CPU thermal management

### GENERAL DESCRIPTION

The **TMP35/TMP36/TMP37** are low voltage, precision centi-grade temperature sensors. They provide a voltage output that is linearly proportional to the Celsius (centigrade) temperature. The **TMP35/TMP36/TMP37** do not require any external calibration to provide typical accuracies of ±1°C at +25°C and ±2°C over the -40°C to +125°C temperature range.

The low output impedance of the **TMP35/TMP36/TMP37** and its linear output and precise calibration simplify interfacing to temperature control circuitry and ADCs. All three devices are intended for single-supply operation from 2.7 V to 5.5 V maximum. The supply current runs well below 50 µA, providing very low self-heating—less than 0.1°C in still air. In addition, a shutdown function is provided to cut the supply current to less than 0.5 µA.

The **TMP35** is functionally compatible with the LM35/LM45 and provides a 250 mV output at 25°C. The **TMP35** reads temperatures from 10°C to 125°C. The **TMP36** is specified from -40°C to +125°C, provides a 750 mV output at 25°C, and operates to 125°C from a single 2.7 V supply. The **TMP36** is functionally compatible with the LM50. Both the **TMP35** and **TMP36** have an output scale factor of 10 mV/°C.

The **TMP37** is intended for applications over the range of 5°C to 100°C and provides an output scale factor of 20 mV/°C. The **TMP37** provides a 500 mV output at 25°C. Operation extends to 150°C with reduced accuracy for all devices when operating from a 5 V supply.

The **TMP35/TMP36/TMP37** are available in low cost 3-lead TO-92, 8-lead SOIC\_N, and 5-lead SOT-23 surface-mount packages.

### FUNCTIONAL BLOCK DIAGRAM

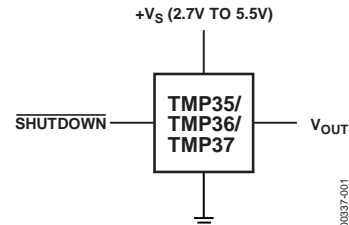


Figure 1.

00337-001

### PIN CONFIGURATIONS

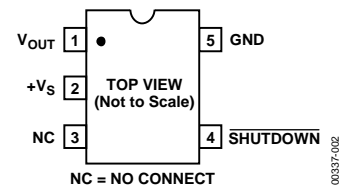


Figure 2. RJ-5 (SOT-23)

00337-002

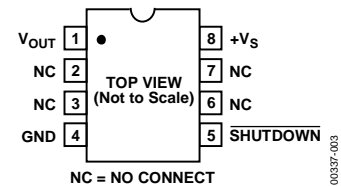
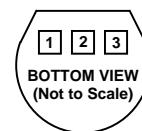


Figure 3. R-8 (SOIC\_N)

00337-003



PIN 1, +V\_S; PIN 2, V\_OUT; PIN 3, GND

Figure 4. T-3 (TO-92)

00337-004

Rev. G

[Document Feedback](#)

Information furnished by Analog Devices is believed to be accurate and reliable. However, no responsibility is assumed by Analog Devices for its use, nor for any infringements of patents or other rights of third parties that may result from its use. Specifications subject to change without notice. No license is granted by implication or otherwise under any patent or patent rights of Analog Devices. Trademarks and registered trademarks are the property of their respective owners.

One Technology Way, P.O. Box 9106, Norwood, MA 02062-9106, U.S.A.  
Tel: 781.329.4700 ©1996–2013 Analog Devices, Inc. All rights reserved.  
[Technical Support](#) [www.analog.com](http://www.analog.com)

**TABLE OF CONTENTS**

Features ..... 1

Applications..... 1

General Description ..... 1

Functional Block Diagram ..... 1

Pin Configurations ..... 1

Revision History ..... 2

Specifications..... 3

Absolute Maximum Ratings..... 4

    Thermal Resistance ..... 4

    ESD Caution..... 4

Typical Performance Characteristics ..... 5

Functional Description ..... 8

Applications Information ..... 9

    Shutdown Operation..... 9

    Mounting Considerations ..... 9

    Thermal Environment Effects ..... 9

Basic Temperature Sensor Connections..... 10

Fahrenheit Thermometers ..... 10

Average and Differential Temperature Measurement ..... 12

Microprocessor Interrupt Generator ..... 13

Thermocouple Signal Conditioning with Cold-Junction Compensation..... 14

Using TMP3x Sensors in Remote Locations ..... 15

Temperature to 4–20 mA Loop Transmitter ..... 15

Temperature-to-Frequency Converter ..... 16

Driving Long Cables or Heavy Capacitive Loads ..... 17

Commentary on Long-Term Stability ..... 17

Outline Dimensions ..... 18

Ordering Guide ..... 19

Automotive Products ..... 20

**REVISION HISTORY**

**11/13—Rev. F to Rev. G**

Change to Table 1, Long-Term Stability Parameter ..... 3

Change to Caption for Figure 38 ..... 18

Changes to Ordering Guide ..... 19

**11/10—Rev. E to Rev. F**

Changes to Features..... 1

Updated Outline Dimensions ..... 18

Changes to Ordering Guide ..... 19

Added Automotive Products Section ..... 20

**8/08—Rev. D to Rev. E**

Updated Outline Dimensions ..... 18

Changes to Ordering Guide ..... 19

**3/05—Rev. C to Rev. D**

Updated Format ..... Universal

Changes to Specifications ..... 3

Additions to Absolute Maximum Ratings..... 4

Updated Outline Dimensions ..... 18

Changes to Ordering Guide ..... 19

**10/02—Rev. B to Rev. C**

Changes to Specifications.....3

Deleted Text from Commentary on Long-Term Stability Section..... 13

Updated Outline Dimensions..... 14

**9/01—Rev. A to Rev. B**

Edits to Specifications .....2

Addition of New Figure 1 .....2

Deletion of Wafer Test Limits Section .....3

**6/97—Rev. 0 to Rev. A**

**3/96—Revision 0: Initial Version**

## SPECIFICATIONS

$V_S = 2.7\text{ V to }5.5\text{ V}$ ,  $-40^\circ\text{C} \leq T_A \leq +125^\circ\text{C}$ , unless otherwise noted.

Table 1.

Parameter <sup>1</sup>	Symbol	Test Conditions/Comments	Min	Typ	Max	Unit
<b>ACCURACY</b>						
TMP35/TMP36/TMP37 (F Grade)		$T_A = 25^\circ\text{C}$		$\pm 1$	$\pm 2$	$^\circ\text{C}$
TMP35/TMP36/TMP37 (G Grade)		$T_A = 25^\circ\text{C}$		$\pm 1$	$\pm 3$	$^\circ\text{C}$
TMP35/TMP36/TMP37 (F Grade)		Over rated temperature		$\pm 2$	$\pm 3$	$^\circ\text{C}$
TMP35/TMP36/TMP37 (G Grade)		Over rated temperature		$\pm 2$	$\pm 4$	$^\circ\text{C}$
Scale Factor, TMP35		$10^\circ\text{C} \leq T_A \leq 125^\circ\text{C}$		10		$\text{mV}/^\circ\text{C}$
Scale Factor, TMP36		$-40^\circ\text{C} \leq T_A \leq +125^\circ\text{C}$		10		$\text{mV}/^\circ\text{C}$
Scale Factor, TMP37		$5^\circ\text{C} \leq T_A \leq 85^\circ\text{C}$		20		$\text{mV}/^\circ\text{C}$
		$5^\circ\text{C} \leq T_A \leq 100^\circ\text{C}$		20		$\text{mV}/^\circ\text{C}$
Load Regulation		$3.0\text{ V} \leq V_S \leq 5.5\text{ V}$ $0\ \mu\text{A} \leq I_L \leq 50\ \mu\text{A}$ $-40^\circ\text{C} \leq T_A \leq +105^\circ\text{C}$		6	20	$\text{m}^\circ\text{C}/\mu\text{A}$
Power Supply Rejection Ratio	PSRR	$-105^\circ\text{C} \leq T_A \leq +125^\circ\text{C}$ $T_A = 25^\circ\text{C}$ $3.0\text{ V} \leq V_S \leq 5.5\text{ V}$		25 30 50	60 100	$\text{m}^\circ\text{C}/\mu\text{A}$ $\text{m}^\circ\text{C}/\text{V}$ $\text{m}^\circ\text{C}/\text{V}$
Linearity				0.5		$^\circ\text{C}$
Long-Term Stability		$T_A = 150^\circ\text{C}$ for 1000 hours		0.4		$^\circ\text{C}$
<b>SHUTDOWN</b>						
Logic High Input Voltage	$V_{IH}$	$V_S = 2.7\text{ V}$	1.8			V
Logic Low Input Voltage	$V_{IL}$	$V_S = 5.5\text{ V}$			400	mV
<b>OUTPUT</b>						
TMP35 Output Voltage		$T_A = 25^\circ\text{C}$		250		mV
TMP36 Output Voltage		$T_A = 25^\circ\text{C}$		750		mV
TMP37 Output Voltage		$T_A = 25^\circ\text{C}$		500		mV
Output Voltage Range			100		2000	mV
Output Load Current	$I_L$		0		50	$\mu\text{A}$
Short-Circuit Current	$I_{SC}$	Note 2			250	$\mu\text{A}$
Capacitive Load Driving	$C_L$	No oscillations <sup>2</sup>	1000	10000		pF
Device Turn-On Time		Output within $\pm 1^\circ\text{C}$ , $100\ \text{k}\Omega    100\ \text{pF}$ load <sup>2</sup>		0.5	1	ms
<b>POWER SUPPLY</b>						
Supply Range	$V_S$		2.7		5.5	V
Supply Current	$I_{SY}$ (ON)	Unloaded			50	$\mu\text{A}$
Supply Current (Shutdown)	$I_{SY}$ (OFF)	Unloaded		0.01	0.5	$\mu\text{A}$

<sup>1</sup> Does not consider errors caused by self-heating.

<sup>2</sup> Guaranteed but not tested.

## ABSOLUTE MAXIMUM RATINGS

Table 2.

Parameter <sup>1,2</sup>	Rating
Supply Voltage	7 V
Shutdown Pin	$GND \leq \overline{SHUTDOWN} \leq +V_S$
Output Pin	$GND \leq V_{OUT} \leq +V_S$
Operating Temperature Range	-55°C to +150°C
Die Junction Temperature	175°C
Storage Temperature Range	-65°C to +160°C
IR Reflow Soldering	
Peak Temperature	220°C (0°C/5°C)
Time at Peak Temperature Range	10 sec to 20 sec
Ramp-Up Rate	3°C/sec
Ramp-Down Rate	-6°C/sec
Time 25°C to Peak Temperature	6 min
IR Reflow Soldering—Pb-Free Package	
Peak Temperature	260°C (0°C)
Time at Peak Temperature Range	20 sec to 40 sec
Ramp-Up Rate	3°C/sec
Ramp-Down Rate	-6°C/sec
Time 25°C to Peak Temperature	8 min

<sup>1</sup> Digital inputs are protected; however, permanent damage can occur on unprotected units from high energy electrostatic fields. Keep units in conductive foam or packaging at all times until ready to use. Use proper antistatic handling procedures.

<sup>2</sup> Remove power before inserting or removing units from their sockets.

Stresses above those listed under Absolute Maximum Ratings may cause permanent damage to the device. This is a stress rating only; functional operation of the device at these or any other conditions above those indicated in the operational section of this specification is not implied. Exposure to absolute maximum rating conditions for extended periods may affect device reliability.

### THERMAL RESISTANCE

$\theta_{JA}$  is specified for the worst-case conditions, that is, a device in socket.

Table 3. Thermal Resistance

Package Type	$\theta_{JA}$	$\theta_{JC}$	Unit
TO-92 (T-3-1)	162	120	°C/W
SOIC_N (R-8)	158	43	°C/W
SOT-23 (RJ-5)	300	180	°C/W

### ESD CAUTION



**ESD (electrostatic discharge) sensitive device.** Charged devices and circuit boards can discharge without detection. Although this product features patented or proprietary protection circuitry, damage may occur on devices subjected to high energy ESD. Therefore, proper ESD precautions should be taken to avoid performance degradation or loss of functionality.



TYPICAL PERFORMANCE CHARACTERISTICS

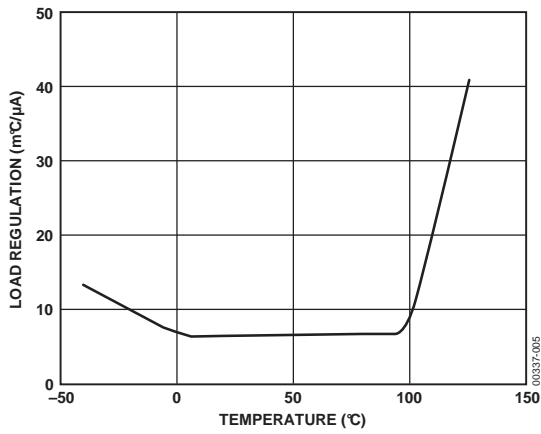


Figure 5. Load Regulation vs. Temperature (m°C/µA)

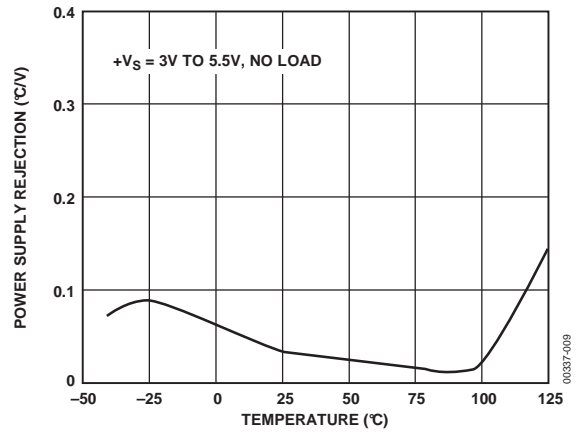


Figure 8. Power Supply Rejection vs. Temperature

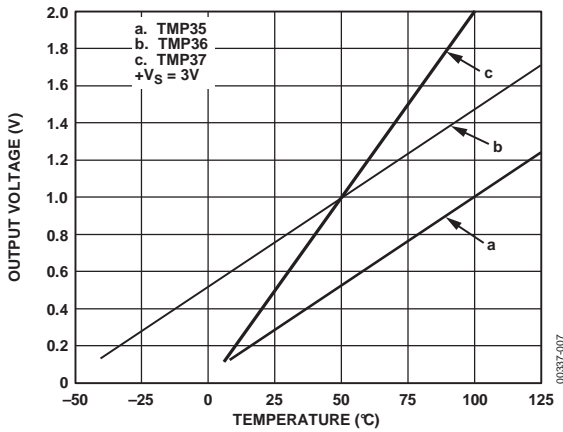


Figure 6. Output Voltage vs. Temperature

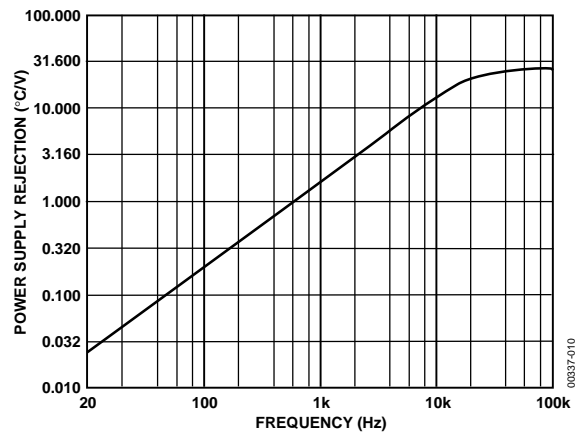


Figure 9. Power Supply Rejection vs. Frequency

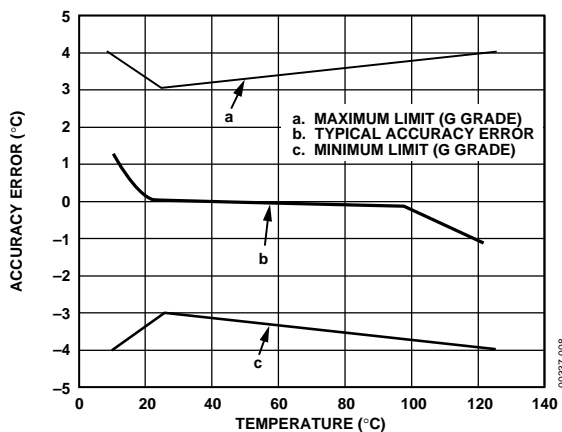


Figure 7. Accuracy Error vs. Temperature

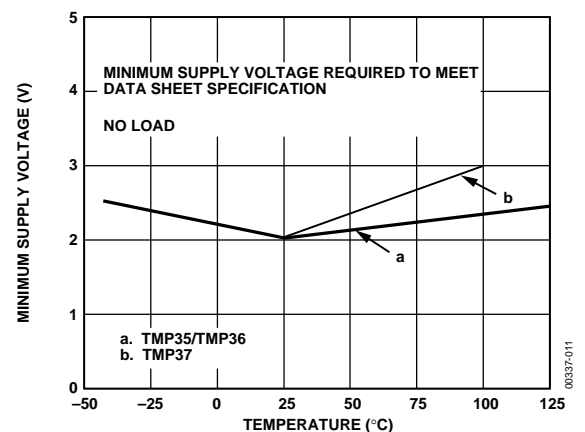


Figure 10. Minimum Supply Voltage vs. Temperature

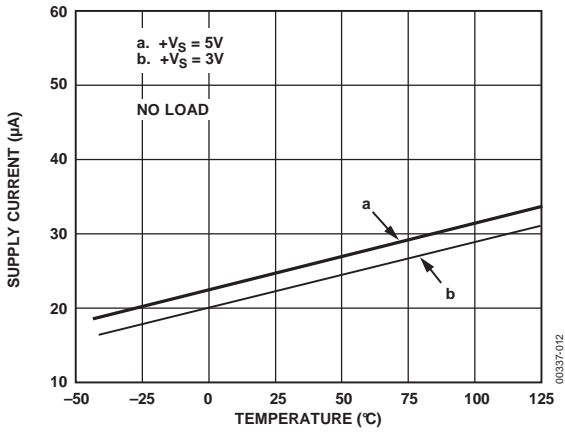


Figure 11. Supply Current vs. Temperature

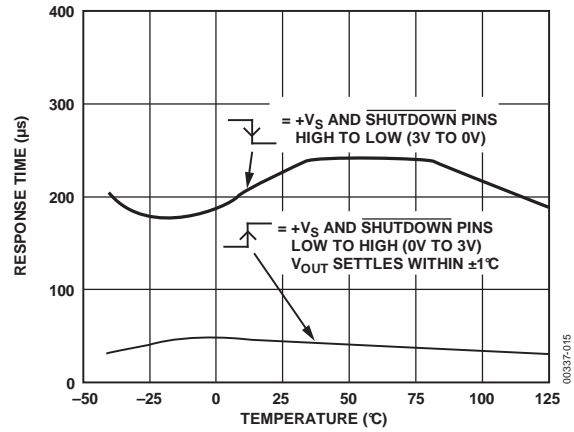


Figure 14.  $V_{OUT}$  Response Time for  $+V_S$  Power-Up/Power-Down vs. Temperature

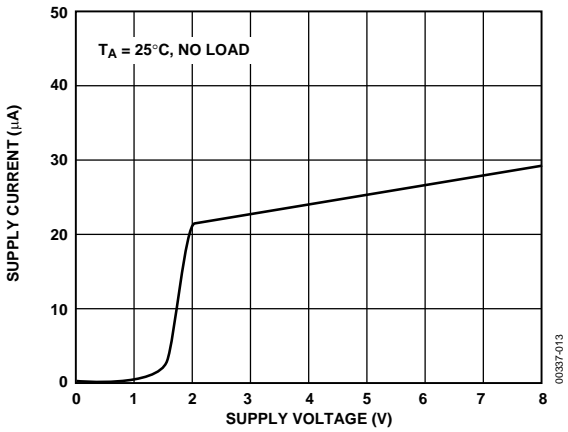


Figure 12. Supply Current vs. Supply Voltage

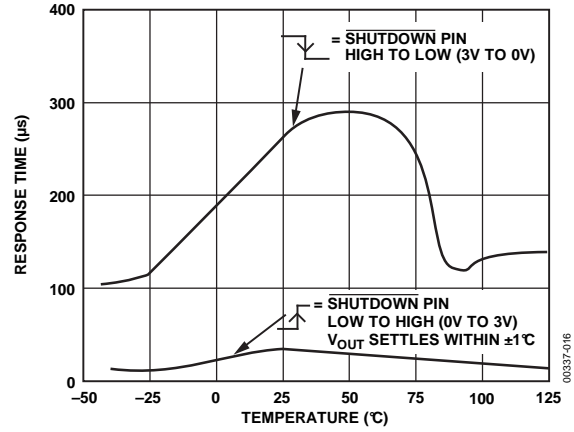


Figure 15.  $V_{OUT}$  Response Time for  $\overline{SHUTDOWN}$  Pin vs. Temperature

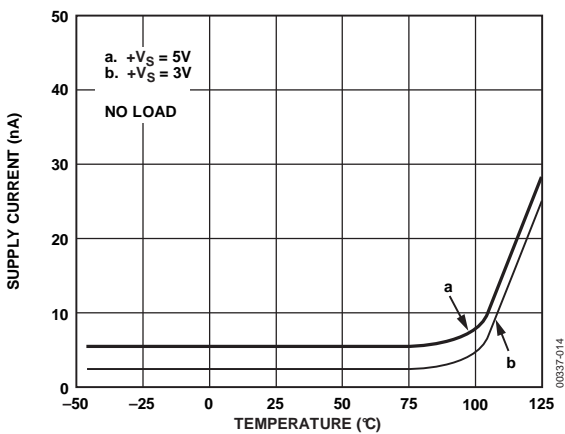


Figure 13. Supply Current vs. Temperature (Shutdown = 0 V)

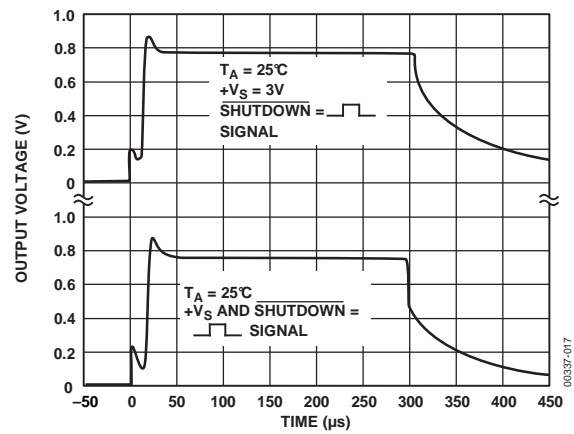


Figure 16.  $V_{OUT}$  Response Time to  $\overline{SHUTDOWN}$  Pin and  $+V_S$  Pin vs. Time

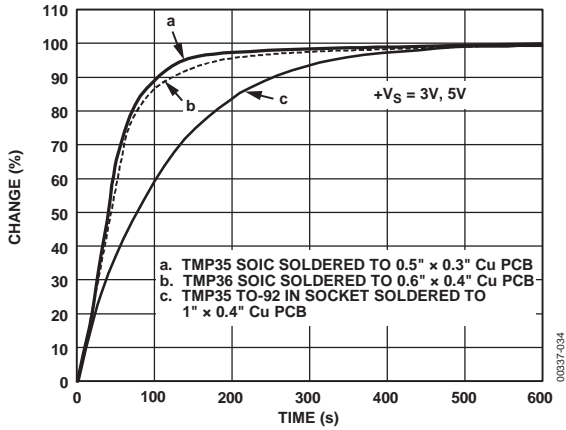


Figure 17. Thermal Response Time in Still Air

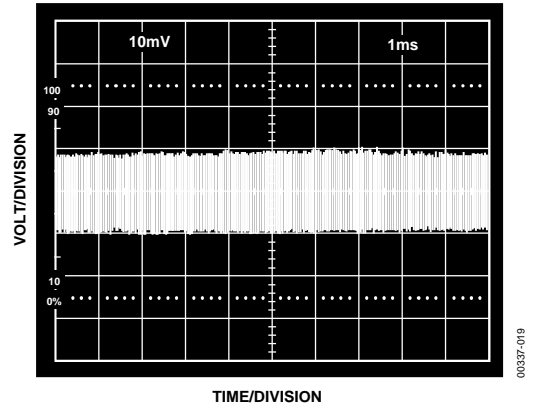


Figure 20. Temperature Sensor Wideband Output Noise Voltage; Gain = 100, BW = 157 kHz

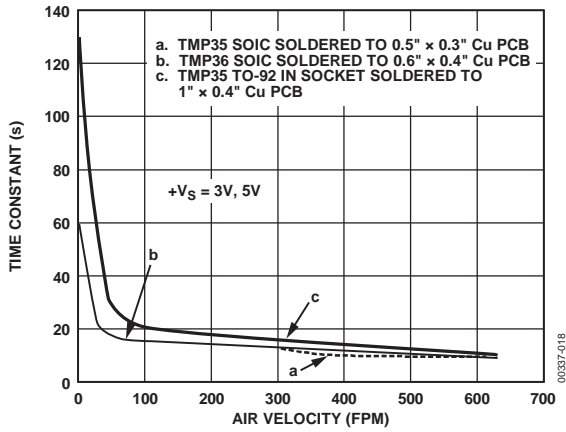


Figure 18. Thermal Response Time Constant in Forced Air

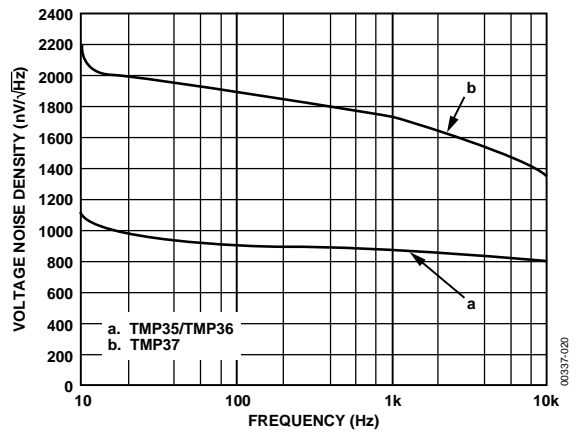


Figure 21. Voltage Noise Spectral Density vs. Frequency

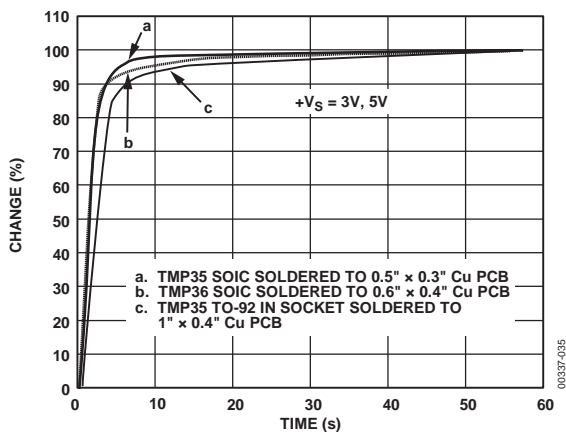


Figure 19. Thermal Response Time in Stirred Oil Bath

# MPXV7002 Integrated Silicon Pressure Sensor On-Chip Signal Conditioned, Temperature Compensated and Calibrated

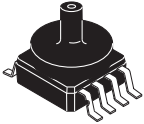
The MPXV7002 series piezoresistive transducers are state-of-the-art monolithic silicon pressure sensors designed for a wide range of applications, but particularly those employing a microcontroller or microprocessor with A/D inputs. This transducer combines advanced micromachining techniques, thin-film metallization, and bipolar processing to provide an accurate, high level analog output signal that is proportional to the applied pressure.

## Features

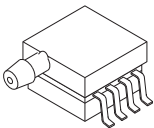
- 2.5% Typical Error over +10°C to +60°C with Auto Zero
- 6.25% Maximum Error over +10°C to +60°C without Auto Zero
- Ideally Suited for Microprocessor or Microcontroller-Based Systems
- Thermoplastic (PPS) Surface Mount Package
- Temperature Compensated over +10° to +60°C
- Patented Silicon Shear Stress Strain Gauge
- Available in Differential and Gauge Configurations

## MPXV7002

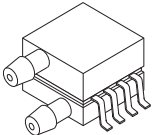
-2 to +2 kPa (-0.3 to +0.3 psi)  
0.5 to 4.5 V Output



**MPXV7002GC6U/C6T1**  
CASE 482A

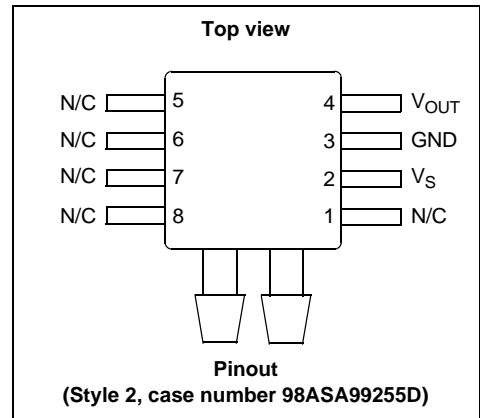


**MPXV7002GP**  
CASE 1369



**MPXV7002DP**  
CASE 1351

**Small Outline Package**



ORDERING INFORMATION									
Device Name	Package Options	Case No.	# of Ports			Pressure Type			Device Marking
			None	Single	Dual	Gauge	Differential	Absolute	
<b>Small Outline Package (MPXV7002 Series)</b>									
MPXV7002GC6U	Rails	482A		•		•			MPXV7002G
MPXV7002GC6T1	Tape & Reel	482A		•		•			MPXV7002G
MPXV7002GP	Trays	1369		•		•			MPXV7002G
MPXV7002DP	Trays	1351			•		•		MPXV7002DP

# 1 Operating Characteristics

**Table 1. Operating Characteristics** ( $V_S = 5.0$  Vdc,  $T_A = 25^\circ\text{C}$  unless otherwise noted. Decoupling circuit shown in [Figure 3](#) required to meet specification.)

Characteristic	Symbol	Min	Typ	Max	Unit
Pressure Range <sup>(1)</sup>	$P_{OP}$	-2.0	—	2.0	kPa
Supply Voltage <sup>(2)</sup>	$V_S$	4.75	5.0	5.25	Vdc
Supply Current	$I_o$	—	—	10	mAdc
Pressure Offset <sup>(3)</sup> @ $V_S = 5.0$ Volts	$V_{off}$	2.25	2.5	2.75	Vdc
Full Scale Output <sup>(4)</sup> @ $V_S = 5.0$ Volts	$V_{FSO}$	4.25	4.5	4.75	Vdc
Full Scale Span <sup>(5)</sup> @ $V_S = 5.0$ Volts	$V_{FSS}$	3.5	4.0	4.5 V	Vdc
Accuracy <sup>(6)</sup>	—	—	$\pm 2.5^{(7)}$	$\pm 6.25$	% $V_{FSS}$
Sensitivity	V/P	—	1.0	—	V/kPa
Response Time <sup>(8)</sup>	$t_R$	—	1.0	—	ms
Output Source Current at Full Scale Output	$I_{O+}$	—	0.1	—	mAdc
Warm-Up Time <sup>(9)</sup>	—	—	20	—	ms

1. 1.0 kPa (kiloPascal) equals 0.145 psi.

2. Device is ratiometric within this specified excitation range.

3. Offset ( $V_{off}$ ) is defined as the output voltage at the minimum rated pressure.

4. Full Scale Output ( $V_{FSO}$ ) is defined as the output voltage at the maximum or full rated pressure.

5. Full Scale Span ( $V_{FSS}$ ) is defined as the algebraic difference between the output voltage at full rated pressure and the output voltage at the minimum rated pressure.

6. Accuracy (error budget) consists of the following:

Linearity: Output deviation from a straight line relationship with pressure over the specified pressure range.

Temperature Hysteresis: Output deviation at any temperature within the operating temperature range, after the temperature is cycled to and from the minimum or maximum operating temperature points, with zero differential pressure applied.

Pressure Hysteresis: Output deviation at any pressure within the specified range, when this pressure is cycled to and from the minimum or maximum rated pressure, at  $25^\circ\text{C}$ .

TcSpan: Output deviation over the temperature range of  $10^\circ$  to  $60^\circ\text{C}$ , relative to  $25^\circ\text{C}$ .

TcOffset: Output deviation with minimum rated pressure applied, over the temperature range of  $10^\circ$  to  $60^\circ\text{C}$ , relative to  $25^\circ\text{C}$ .

Variation from Nominal: The variation from nominal values, for Offset or Full Scale Span, as a percent of  $V_{FSS}$ , at  $25^\circ\text{C}$ .

7. Auto Zero at Factory Installation: Due to the sensitivity of the MPXV7002 Series, external mechanical stresses and mounting position can affect the zero pressure output reading. Auto zero is defined as storing the zero pressure output reading and subtracting this from the device's output during normal operations. Reference AN1636 for specific information. The specified accuracy assumes a maximum temperature change of  $\pm 5^\circ\text{C}$  between auto zero and measurement.

8. Response Time is defined as the time for the incremental change in the output to go from 10% to 90% of its final value when subjected to a specified step change in pressure.

9. Warm-up Time is defined as the time required for the product to meet the specified output voltage after the Pressure has been stabilized.

## 2 Maximum Ratings

Table 2. Maximum Ratings<sup>(1)</sup>

Rating	Symbol	Value	Unit
Maximum Pressure ( $P_1 > P_2$ )	$P_{max}$	75	kPa
Storage Temperature	$T_{stg}$	-30 to +100	°C
Operating Temperature	$T_A$	10 to 60	°C

1. Exposure beyond the specified limits may cause permanent damage or degradation to the device.

Figure 1 shows a block diagram of the internal circuitry integrated on a pressure sensor chip.

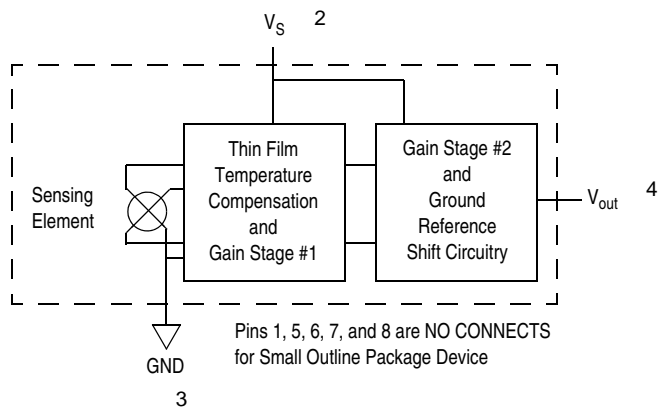


Figure 1. Integrated Pressure Sensor Schematic

### 3 On-Chip Temperature Compensation, Calibration and Signal Conditioning

The performance over temperature is achieved by integrating the shear-stress strain gauge, temperature compensation, calibration and signal conditioning circuitry onto a single monolithic chip.

Figure 2 illustrates the Differential or Gauge configuration in the basic chip carrier (Case 482). A gel die coat isolates the die surface and wire bonds from the environment, while allowing the pressure signal to be transmitted to the sensor diaphragm.

The MPXV7002 series pressure sensor operating characteristics, and internal reliability and qualification tests are based on use of dry air as the pressure media. Media, other than dry air, may have adverse effects on sensor performance and long-term reliability. Contact the factory for information regarding media compatibility in your application.

Figure 3 shows the recommended decoupling circuit for interfacing the integrated sensor to the A/D input of a microprocessor or microcontroller. Proper decoupling of the power supply is recommended.

Figure 4 shows the sensor output signal relative to pressure input. Typical, minimum, and maximum output curves are shown for operation over a temperature range of 10° to 60°C using the decoupling circuit shown in Figure 3. The output will saturate outside of the specified pressure range.

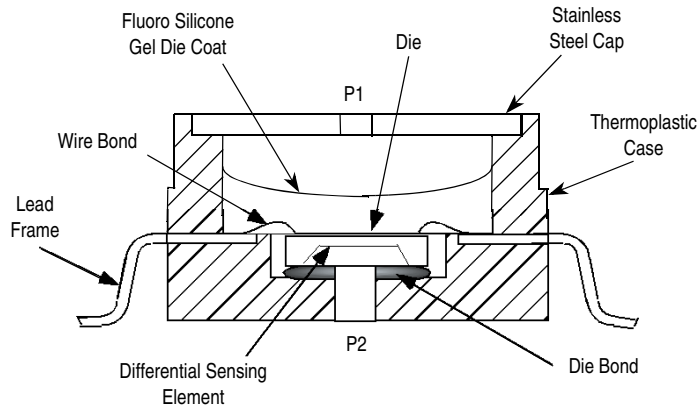


Figure 2. Cross-Sectional Diagram SOP (not to scale)

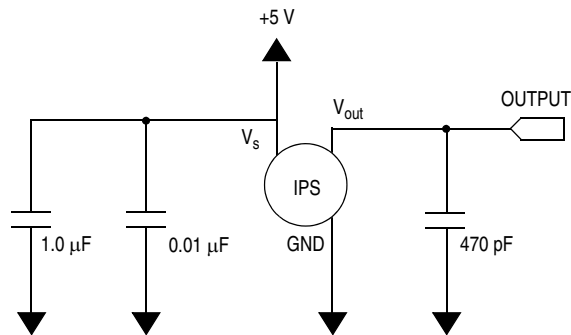


Figure 3. Recommended Power Supply Decoupling and Output Filtering (For additional output filtering, please refer to Application Note AN1646.)

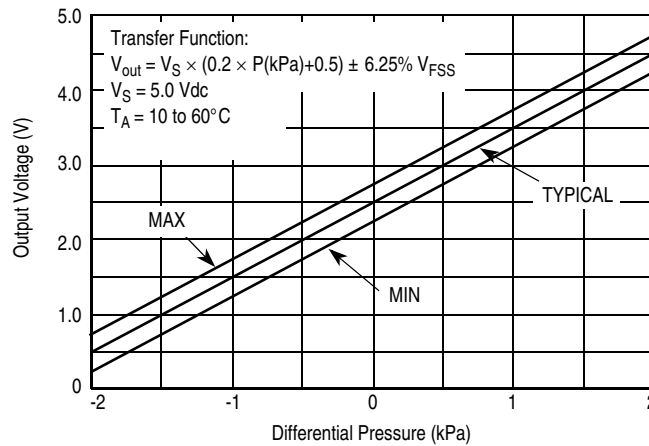


Figure 4. Output versus Pressure Differential

#### 4 Pressure (P1)/Vacuum (P2) Side Identification Table

Freescale designates the two sides of the pressure sensor as the Pressure (P1) side and the Vacuum (P2) side. The Pressure (P1) side is the side containing a gel die coat which protects the die from harsh media.

The Pressure (P1) side may be identified by using the following table:

Part Number	Case Type	Pressure (P1) Side Identifier
MPXV7002GC6U/GC6T1	482A-01	Side with Port Attached
MPXV7002GP	1369-01	Side with Port Attached
MPXV7002DP	1351-01	Side with Part Marking

#### 5 Minimum Recommended Footprint for Surface Mounted Applications

Surface mount board layout is a critical portion of the total design. The footprint for the surface mount packages must be the correct size to ensure proper solder connection interface between the board and the package. With the correct footprint, the packages will self align when subjected to a solder reflow process. It is always recommended to design boards with a solder mask layer to avoid bridging and shorting between solder pads.

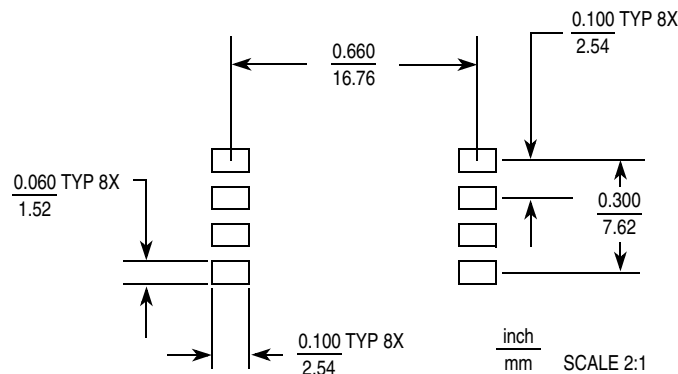
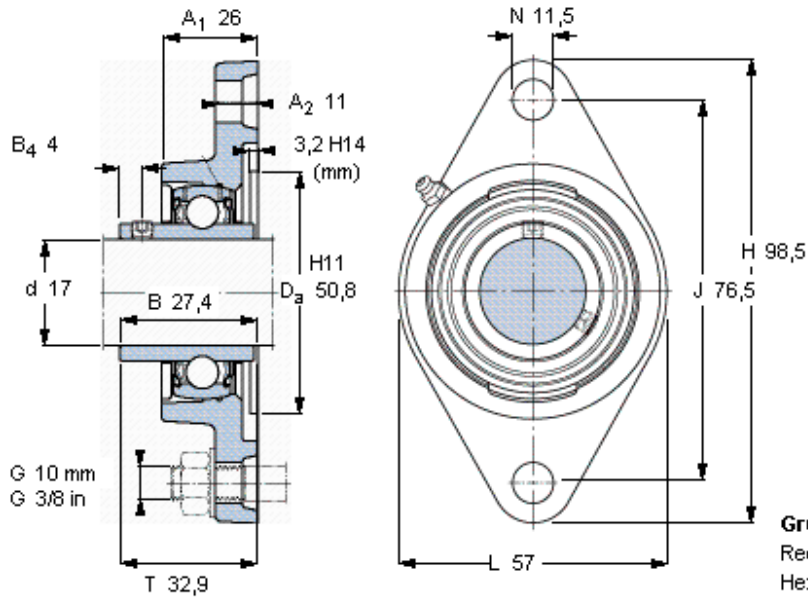


Figure 5. Small Outline Package Footprint



Y-bearing flanged units, cast housing, oval flange, grub screw locking

Principal dimensions					Basic load ratings		Designations		
d	A1	J	L	T	dynamic C	static C0	Bearing unit	Housing	Bearing
mm					kN		-		
<b>17</b>	26	76,5	57	32,9	9,56	4,75	FYTB 17 TF	FYTB 503 M	YAR 203-2F



**Grub screw**

Recommended tightening torque [Nm]

Hexagonal key size [mm]

**End cover**

M6x0.75

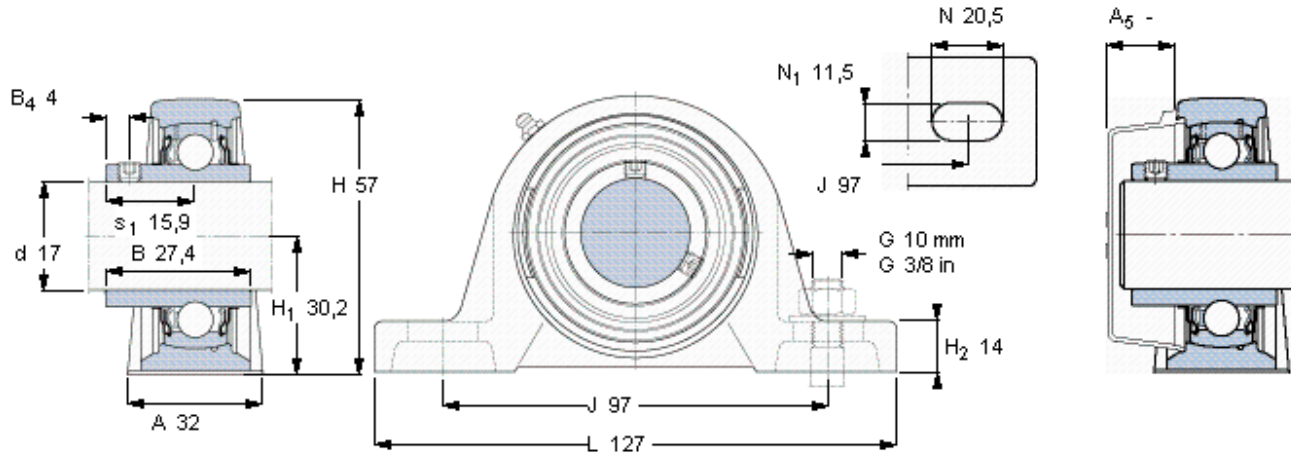
4

3

-

Y-bearing plummer block units, cast housing, grub screw locking

Principal dimensions					Basic load ratings		Designations		
d	A	H	H <sub>1</sub>	L	dynamic C	static C <sub>0</sub>	Bearing unit	Housing	Bearing
mm					kN		-		
17	32	57	30,2	127	9,56	4,75	SY 17 TF	SY 503 M	YAR 203-2F



<b>Grub screw</b>	M6x0.75
Recommended tightening torque [Nm]	4
Hexagonal key size [mm]	3
<b>End cover</b>	-